EN BUSCA DE POBLACIONES MÚLTIPLES EN EL CÚMULO GLOBULAR RUPRECHT 106 Y UN MÉTODO COMPLEMENTARIO PARA ENCONTRARLAS.
(Searching for multiple populations in the Globular Cluster Ruprecht 106 and a complementary method to uncover them.)

Tesis presentada a la Facultad de Ciencias Físicas y Matemáticas para optar al grado de Doctor en Física

Por: Heinz Ernesto Frelijj Rubilar
Profesor Guía: Sandro Villanova

Agosto 2021
Concepción - Chile

1 Acknowledgements

A mi familia, a mi profesor guia y a mis compañeros por las enseñanzas y apoyo durante estos 4 años.

TOPCAT (Taylor 2005) was used to make most of the plots and histograms in this work.

2 Abstract

Part 1: More than a decade has passed since the definition of Globular Cluster (GC) changed, and now we know that they host Multiple Populations (MPs). But at least one GC does not share that behaviour - Ruprecht 106. We analyzed thirteen member red giant branch stars using spectra in the wavelength range 6120-6405 Å obtained through the GIRAFFE Spectrograph, mounted at UT2 telescope at Paranal. We also observed the whole cluster using C, V, R and I photometry obtained through the Swope telescope at Las Campanas. Atmospheric parameters were determined from the photometry to determine Fe and Na abundances. A photometric analysis searching for MPs was also carried out. Both analyses confirm that Ruprecht 106 is indeed one on the few GCs to host Simple Stellar Population, in agreement with previous studies. Finally, a dynamical study concerning its orbits was carried out to analyze the possible extra galactic origin of the Cluster. The orbital integration indicates that this GC belongs to the inner halo, while an Energy plane shows that it cannot be accurately associated with any known extragalactic progenitor.

Part 2: Multiple Populations(MP) in Globular Clusters can be detected both spectroscopically and with appropriate photometric filters. Filters specifically sensitive to light element abundances are particularly effective. One such filter is the classic C(Carbon) filter, one of the original set of Washington System filters. It has proved to be efficient in detecting multiple populations, in combination with the T_1 filter in the form of the $C - T_1$ color. In this research we test the ability of a three Washington filter combination, $(C - T_1) - (T_1 - T_2)$. We compare the ability of this color combination with that of the traditional $C - T_1$ color on two globular clusters, NGC 7099 and NGC 1851, types I and II Globular clusters, respectively. Our improved photometry and membership selection, now using Gaia proper motions, finds that the second generation stars are more centrally concentrated than first generation stars, as expected and contrary to our previous findings for NGC 7099. We find that multiple populations are more easily detected in the new $(C - T_1) - (T_1 - T_2)$ color, although $C - T_1$ conserves the best width/error ratio. We also search for differences of both colors while splitting the red-RGB and the blue-RGB in NGC 1851, but no significant improvement was found.

Contents

List of Figures

List of Tables

3 Introduction

3.1 Basic Concepts

3.1.1 Star Clusters

Star Clusters are groups of stars gravitationally bound. Their composition, age and number of stars will vary depending of their type. In our galaxy there are two types of Star Clusters: Open Clusters and Globular Clusters.

Star clusters are formed in Giant Molecular Clouds composed principally of H_2. Once the first stars begin to form, the remaining Hydrogen gas near them is illuminated and ionized (ionized Hydrogen is called HII). This indicates that only a small fraction (24 ± 9 % - Chandar et al. 2018) of the gas is used to form stars, and all the remnant gas that is heated is rapidly blown away from the protocluster. After this stage most of the stars remain together due to their collective gravity, but there are some that escape due to the exchange of energy of the stars inside the protocluster. The remaining stars become gravitationally bound, forming an "Open Cluster".

Subsequent survival depends mostly on the cluster mass. If sufficiently massive, the cluster can survive for roughly a Hubble time. Our Galaxy produced a very large number of very massive clusters early in its infancy which still survive today, which are called "Globular Clusters".
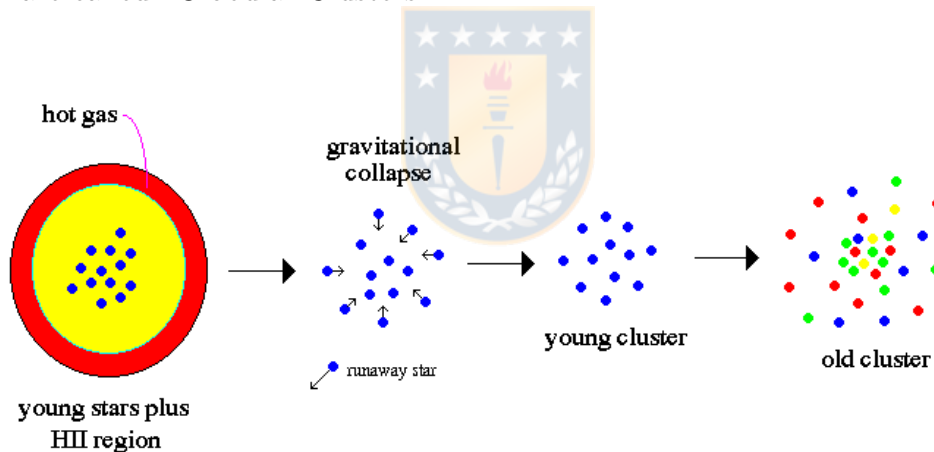
Figure 1: Stages of formation for star clusters. Source: Own elaboration

Open Clusters

An Open Cluster is a group of stars orbiting in the disk of the galaxy, normally from a few hundred up to a few thousand stars, that share the same Giant Molecular Cloud as a place of birth. Since this cloud is believed to be homogeneous and star formation proceeds rapidly, all of the stars formed have roughly the same age and the same initial chemical composition(see "Stellar Populations"). The name "Open" is due to their loose appearance, because the stars inside them are relatively loosely bound to each other and there are relatively small number of stars compared to the more massive globular clusters ($10 - 10^4$ solar masses versus $10^4 - 10^6$ solar masses), giving an open cluster an irregular form. They are found in Spiral and Irregular galaxies, in which active star formation is occurring. Open Clusters are considered as young objects compared to globulars. Most are less than a few hundred million

years old, and it is common to find gas from molecular clouds surrounding them, meaning that stars may still form nearby. Their relatively young age is graphically demonstrated by the presence of blue, massive stars, that have the shortest lifetimes, indicating a recent formation episode. Open clusters are important objects in the study of stellar evolution, because the stars are all of very similar age and chemical composition (see section "Stellar populations"), and the effects of mass and other more subtle variables on the properties of stars are much more easily studied than they are for isolated stars.

In addition, Open Clusters tend to be dispersed before most of their stars reach the end of their lives, because their small gravitational binding energy allows to the cluster to become disrupted by close encounters with other clusters and clouds of gas, especially dense molecular clouds, as they orbit in the dense Galactic disk. They also lose members through internal close encounters. However, given sufficient mass and depending on their Galactic orbit, some open clusters can survive for a very long time, with a few as old as 8 Gyr.

Figure 2: The Pleiades, one of the best known Open Clusters. Source: www.bibliotecapleyades.net

Globular Clusters

Globular Clusters are very old groups of stars orbiting mainly in the Halo of the Galaxy, but we can found them also in the thick disk and the bulge. The halo clusters orbit in generally random directions, with no net rotation. They are tightly gravitationally bounded, giving to the cluster a spherical or "globular" shape. They are composed of hundreds of thousands or millions of old, low mass, low metal content stars, with higher density towards the center of the cluster.

One of the most notable characteristics of Globular Cluster are their ages, because they are among the oldest objects in the universe, with the oldest being approximately 13 billion years old. This makes them extremely useful to study the age of the Universe as well as the formation of structure in it like galaxies. There

are no molecular clouds inside Globular clusters, hence there is no current star formation. This fact, alongside their age explains the reason of why there are no young blue stars, which are the brightest ones in the optical wavelength, and the most massive. Because of this, high mass stars evolve more rapidly than low-mass stars because they develop the necessary central pressures and temperatures for hydrogen fusion sooner and at much higher values than their lower mass cousins, and therefore burn their larger supply of fuel much more rapidly.(Kaufmann, W.J., Universe, 3rd Edition). The brightest stars in globular clusters (in the optical) are instead red giants.

There is a strong debate about the formation scenarios of Globular Clusters. One of the most accepted formation theories is the one described in the beginning of "Stars Clusters" section, but some studies, like Ideta & Makino (2004) present evidence of the formation of ω Centauri by Tidal Stripping of a Dwarf Galaxy. However, it is now recognized that ω Cen is a very unusual object (the most massive GC in the Galaxy) and its formation and evolution is not typical.

Globular Clusters were for a very long time considered as Simple Stellar Populations (see "Stellar populations"), but different kinds of studies during the last 2 decades showed the opposite, originating the term "Multiple Populations" explained later in this work.

Figure 3: ω Centauri, the most massive globular cluster in the Galaxy. Source: http://earthsky.org

3.1.2 Observational Techniques

Studies like the search for Multiple populations requires observational evidence, and for that we need to use appropriate observational techniques and understand how they work in order to properly interpret the data and arrive at robust results. There are two types of techniques: Spectroscopy and Photometry.

Spectroscopy

Spectroscopy is a common method to study the Universe. This method consist in passing light through a slit and a prism to see its spectrum, i.e. the flux as a function of wavelength. An instrument called a spectrograph realizes this action. There are three types of spectra, continuous, absorption and emission.

A continuous spectrum is simply the light in all wavelengths, like a rainbow, having no apparent breaks or gaps throughout its wavelength range.

An emission spectrum consists in discrete bright lines(called emission lines) which appear when heating a gas and passing the resultant radiation through the spectrograph.

An absorption spectrum consists in a continuous spectrum with dark lines (called absorption lines) seen while passing continuous radiation through a colder, low density gas and then a spectrograph. Both the emission and absorption lines are produced by the presence of different elements at different physical conditions (temperature, gravity, etc.)(Eric Chaisson, Steve Mcmillan,(2004) Astronomy Today, Unit 4)
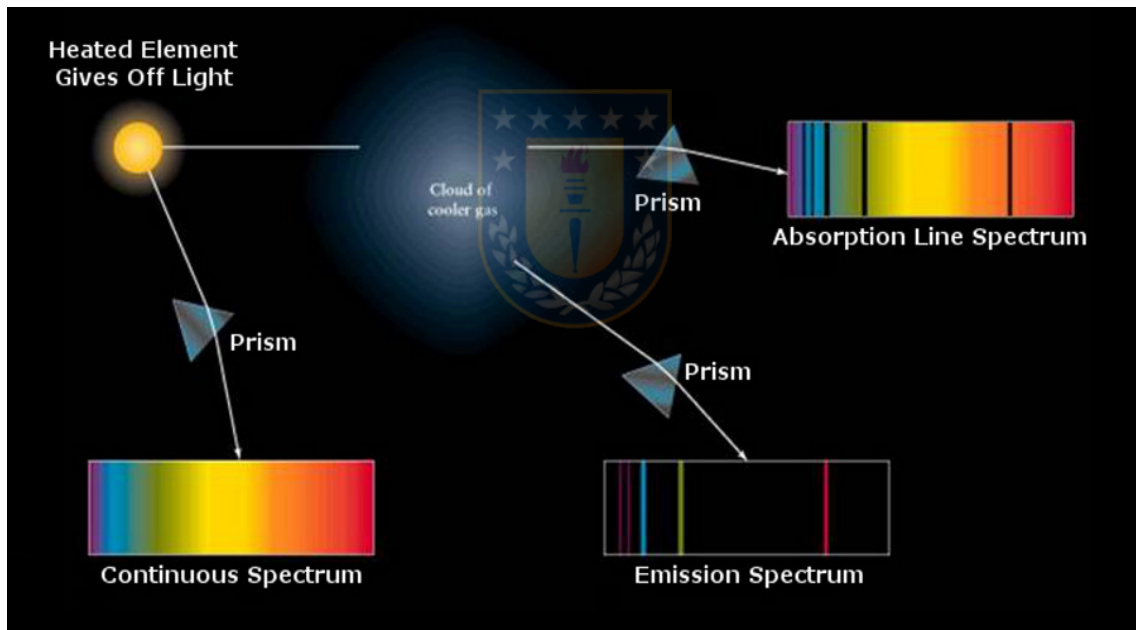
Figure 4: Different types of spectra and how they are produced. Source: http://www-revista.iaa.es

Photometry

Photometry is the science of measuring the flux within a limited wavelength range that we receive from celestial objects. The wavelength range is generally isolated using a filter and then imaging through this filter. The flux in a star is the sum of the star's contribution over all pixels illuminated by it, after subtracting the contribution from the sky background.

A simple kind of photometry consist in using a circular measuring aperture and a concentric sky annulus in which to determine the average sky background, this

is called Aperture Photometry, figure 5 illustrates this. But this method present problems with varying background due to the difficulty of measuring the true sky level(i.e. crowded fields).(W. Romanishin. An introduction to astronomical Photometry using CCDs). A more serious problem, especially in the very crowded central regions of a globular cluster, is that of image crowding, whereby two distinct stars are not well resolved in the image, thus causing the light of each to affect the measurement of the flux from the other.
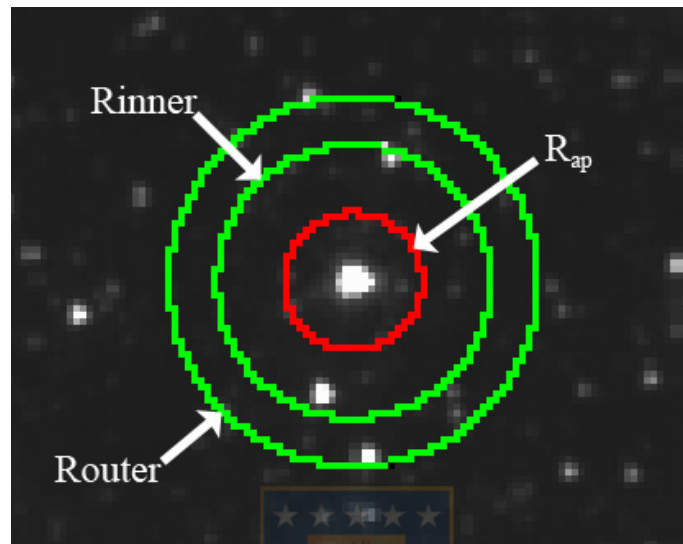
Figure 5: Aperture photometry parameters: standard aperture (red) and local background annulus (green). Source: WISE data processing page.

One useful technique to circumvent this problem is to determine a Point Spread Function (PSF) based in isolated stars of the frame. A PSF is the shape of the CCD image of a point source of light. In astronomy, the dominant determinant of the PSF is smearing caused by the passage of starlight through the Earth's turbulent atmosphere. This smearing is called seeing.
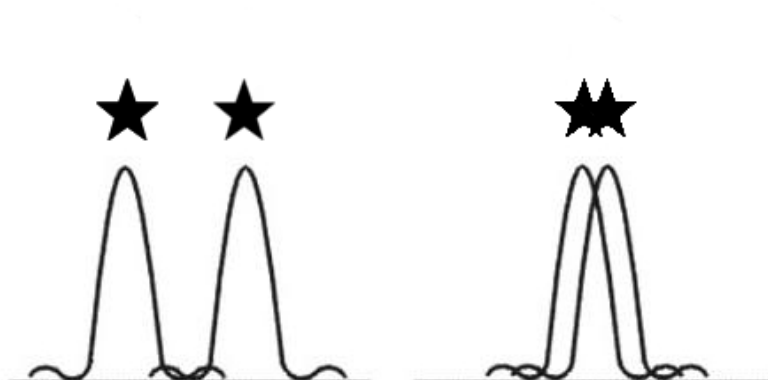
Figure 6: A graphic explanation of how determining a good Point Spread Function is necessary to properly characterize the light profile of stars in crowded fields. Source: Own elaboration

With a well determined PSF, the stars can be measured one by one, starting with the brightest, but then digitally subtracting(by properly shifting and scaling

the image PSF) each star from the image as it is measured. This leaves fewer star to mess up the sky and cause contamination for the fainter stars. This technique is known as PSF Photometry.(W. Romanishin. An introduction to astronomical Photometry using CCDs)

Photometry measurements are combined with the use of colored filters in order to limit the wavelength they measure. Different filters, sensitive to different wavelength regions, yield different information for each star. A commonly used technique is to calculate the difference between the flux in two or more filters to make a color and plot it versus the flux in a filter. This graph is called Color-Magnitude Diagram (CMD).

CMDs of clusters contain a vast amount of information concerning the stars, stellar evolution and the cluster itself; e.g. its distance, age, reddening, composition, etc.
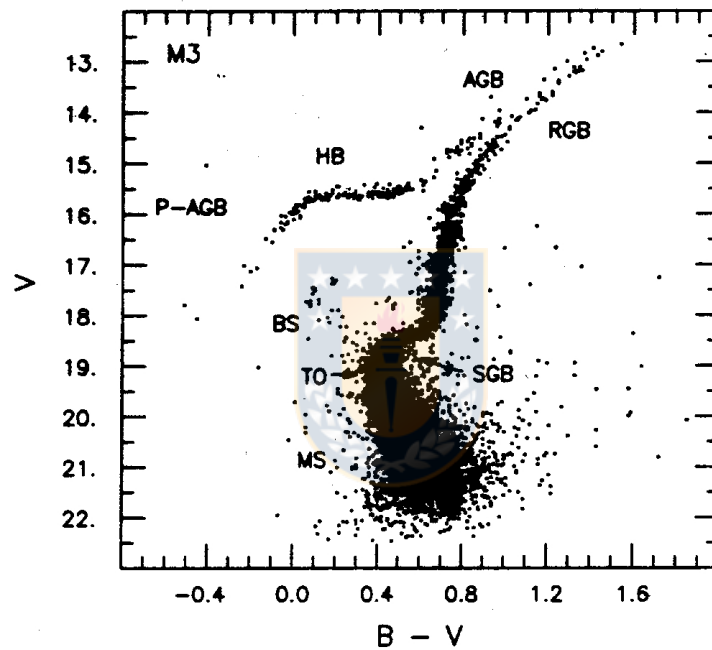
Figure 7: Color-Magnitude Diagram with all its parts. Source: Annual Review of Astronomy And Astrophysics, Vol 26, 1988.

The CMD is divided in the following parts:

Main Sequence(MS): Part of the CMD where the star stays almost all of its life, where stars fuse H into He in their centers.

Turn off Point(TO): Part of the CMD where a star leaves the main sequence after the exhaustion of all its core H.

Subgiant Branch(2GB): Part of the CMD where the star is increasing its size to become later a giant, developing a H-burning shell.

Red Giant Branch(RGB): Part of the CMD where a star stays before helium ignition. At this stage the star is red due to its expanded size which cools the outer layers and is luminous despite its coolness due to its large surface area. The energy source is still H shell burning.

Horizontal Branch(HB): Part of the CMD where stars are powered by helium fusion in the core. It has higher temperature and lesser luminosity than an upper RGB star.

Asymptotic Giant Branch(AGB): Part of the CMD where the star inhabits after core He exhaustion. An AGB star can have both H and He burning shells, causing various instabilities, leading to the ejection of its outer layers to leave a core of carbon and oxygen, leaving a white dwarf. (Astronomy Today/Chaisson & Mcmillan-5th edition)

3.1.3   Stellar Populations

A Stellar Population refers to a group of stars that resemble each other in spatial distribution, chemical composition, kinematics and/or age.

Simple Stellar Populations consists of stars born at the same time and having the same initial element composition. For example, Open Clusters are Simple Stellar Populations, since they are composed of stars with the same age and initial abundance, as confirmed by a number of observational studies. As said in a past section, Globular Clusters were also long considered as Simple Stellar Populations. But over recent years, new investigations have refuted this, finding evidence of different chemical abundances inside Globular Clusters for the majority, if not (almost) all, of them. Thus, a new definition was required: Multiple Populations, indicating that there are not only a single population of stars like open clusters, but two or more populations of stars that do not share the same age and/or initial composition. Thus, the recognition of MPs in globular clusters has revolutionized the understanding of them, making them at the same time both more complicated as well as more interesting.

3.2   Multiple Populations

3.2.1   Formation scenarios for MPs

There are various formation scenarios that try to explain MPs in GCs: The Basic and refined Asymptotic Giant Branch Model (D'Ercole et al. (2008), D'Ercole, D'Antona & Vesperini (2016)), the Fast Rotating Massive Stars model (Decressin et al. (2007) and Decressin, Charbonnel & Meynet (2007)), an Extended cluster formation event model(Prantzos & Charbonnel(2006), Elmegreen (2017)), a model that adopts very massive stars ($> 10^3 \ M_{Sun}$) as the origin of the processed material (Gieles et al. 2018), and even a model that do not invoke multiple epochs of star-formation (Bastian et al. 2013), among others (see Carretta et al. (2010), Hénault-Brunet et al. (2015), Renzini et al. (2015), and so on), but there is no consensus about the true scenario because the majority are in conflict with one or more observational constraints or can't explain some processes. Valcarce & Catelan(2011) make an overview of some scenarios, and present a "toy model" dividing GCs by their initial mass to explain each formation process. The formation process has the same beginning for all cases:

1) A GC begins with the gravitational collapse of a cloud where first generation (1G) stars are formed following a homogeneous distribution throughout the GC. They are initially embedded inside the interstellar medium (ISM) gas that was not used up to form stars. These are indeed a simple stellar population.

2) The gas is distributed over a larger volume than required to trigger a new local fragmentation process to form a new generation of stars, decreasing the local gas

pressure for the same potential well. This causes that the remaining gas starts to fall again into the center of the cluster. Massive stars begin to eject at high velocities their envelopes, which then collide with the falling gas, decreasing the speed of the expanding massive star ejecta and the infalling gas.

From here, the process is differentiated according to the GC initial mass.

Low-mass Progenitor Structures

2b) Low-mass Progenitor Structures (PS) are unable to retain the 1G massive star ejecta because of their shallower potential well, and the consequent low velocity of the infalling primordial gas. For the same reason, the PS core does not contain enough material to transform all the kinetic energy of massive star ejecta into thermal energy. The formation of a viable star-forming cloud in the core is thus inhibited.

3) 1G core-collapse SNe explosions begin, which completely clean the PS of the remaining primordial gas.

4) In this case, Second Generation (2G) stars are formed only with (diluted) gas ejected by super-AGB and/or AGB stars, with the chemical composition of the ejecta depending in detail on the stellar mass.

5) This is potentially a continuous process, with renewed cleansing of the intra-cluster gas taking place after each new star formation event.

Figure 8: Low-mass PS scenario according to Valcarce and Catelan(2011). Stages are detailed in text. Source: Valcarce and Catelan(2011)

Intermediate-mass Progenitor Structures

2b) Since intermediate-mass PSs have deeper gravitational potential wells than low-mass PSs, the infalling gas reaches a higher speed, and a fraction of the massive star ejecta is retained before their progenitors explode. However, in the outer parts of the PS the massive star ejecta are trying to escape, as the pristine gas is infalling. Additionally, in the PS core, where the primordial gas has been accumulating, the

gas ejected by massive stars is slowed down, and the kinetic energy transformed into thermal energy, which delays further star formation.

3) When 1G core-collapse SNe explode, their ejecta compress the center cloud, thus triggering star formation in the 2G. These 2G stars have been highly enriched in helium by the massive star ejecta, but at the same time are not heavily enriched in metals. Assuming that SN explosions are nearly symmetrical and that their precursors are not too close to the center, only a small fraction of the SN ejecta, which is metal-enriched, will be mixed with the core cloud. This event also completely removes the outer mixed gas from the cluster, since the gravitational potential well is not deep enough and the mass of the outer infalling gas is insufficient to retain the SNe ejecta. Thus, 2G stars will accordingly not be metal-enriched.

4) The ejecta of massive 2G stars are not retained in the case of an intermediate-mass PS, because the infalling gas is only produced by intermediate-mass 1G stars. If any such gas is initially retained, it will eventually be expelled by 2G corecollapse SNe or 1G type Ia SNe explosions, or will form but very few stars.

5) After this second cleansing of the cluster, a new cloud begins to form in the cluster center, using the intermediate mass stellar ejecta (mass lost at low velocity) from 1G and 2G stars. The chemical composition of this new cloud falls between both generations, as a consequence of the slope of the IMF (which favors low-mass stars) and the mass ratio of both generations. Here, the first stars of the third generation (TG) will be created.

6) These star formation and cluster ISM cleansing stages continue, with each successive stellar population becoming chemically more similar to 1G stars, while at the same time less numerous.

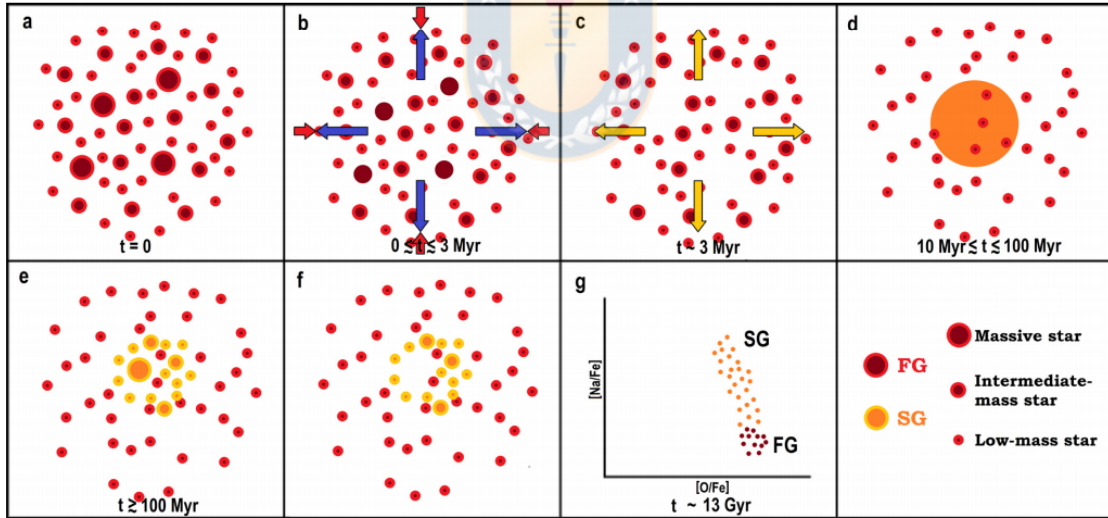Figure 9: Intermediate-mass scenario according to Valcarce and Catelan(2011). Stages are detailed in text. Source: Valcarce and Catelan(2011)

Massive Progenitor Structures

2b) As in Intermediate mass scenario, in the PS core a cloud has been formed that is highly enriched in helium. Its material comes from massive star ejecta and a fraction of the remaining gas that was not used to form 1G stars. However, in the

outer part of the PS the massive star ejecta is trying to escape, while the pristine gas is infalling to the PS center with a velocity (and a total mass) that is higher than in the case of intermediate mass PSs.

3) The first core-collapse SNe explosions compress the core gas, triggering the 2G star formation episode. As in Intermediate mass scenario, these 2G stars are highly enriched in helium. However, in contrast to what happens in the Intermediate mass case, the deeper potential well does allow the gas in the outer part of the cloud to be retained. Most of the SN ejecta tries to escape the cluster, merging with the infalling gas in the process. This event efficiently mixes both gas components, and delays the moment of arrival of this mixed gas to the core.

4) After a while, the highly metal-enriched material is mixed with the gas that was not used to form 2G stars, creating a new cloud in the core of the cluster.

5) This cloud is also fed by 2G massive stars and by both massive and intermediate-mass 1G stars – and these provide the chemical ingredients that will characterize the cluster's third generation (TG) of stars.

6) With three stellar generations in the cluster, the process of star formation continues, but each time with material processed mainly by less massive stars. As a result, the newborn stars belonging to the fourth generation (4G) will have a chemical composition that is a mixture of products from the three preceding generations. In this scenario, 2G and TG stars are created using only a relatively small fraction of the total mass that was used to form 1G stars. In other words, subsequent stellar generations will be increasingly affected by the evolution of lower-mass stars, whose ejecta will not be chemically very different from that of the original PS gas.
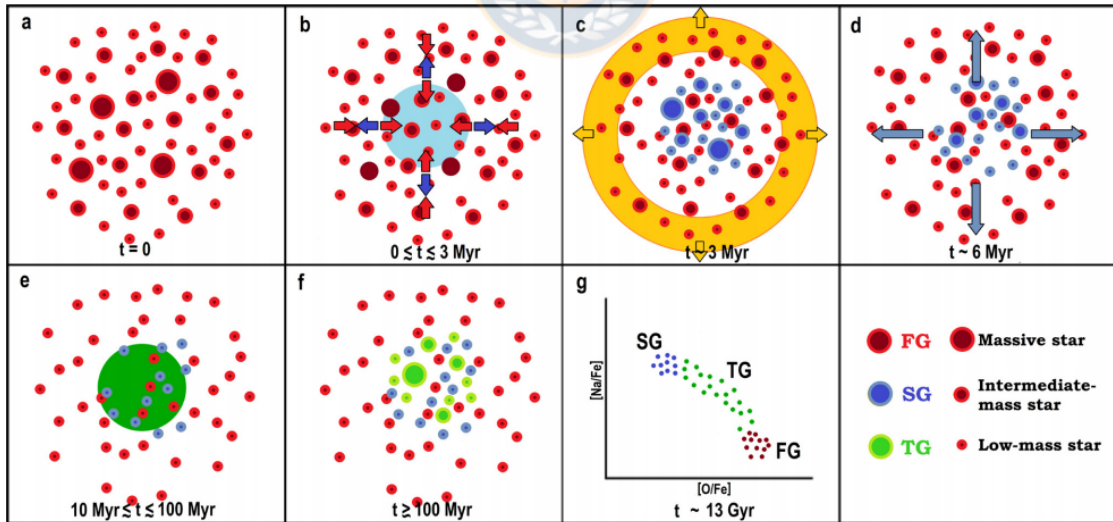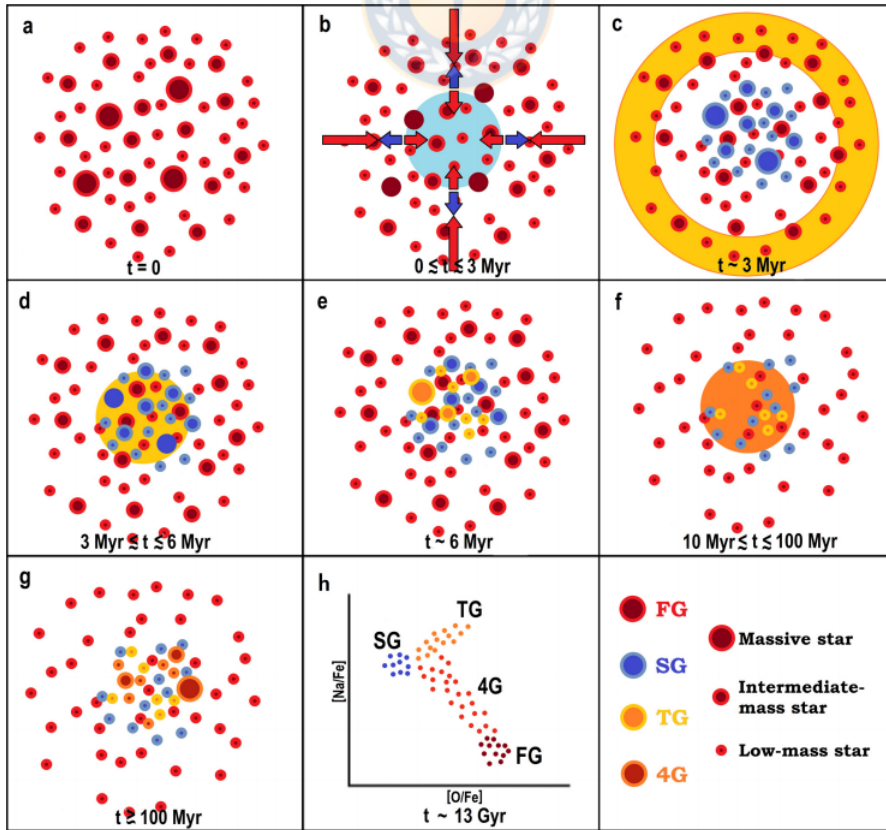

Figure 10: High-mass scenario according to Valcarce and Catelan(2011). Stages are detailed in text. Source: Valcarce and Catelan(2011)

3.2.2 Mass budget problem

Caretta et al.(2009) found that generally 2G stars make up roughly 2/3 of the current cluster population. In order to explain the large fraction of 2G stars seen now and the small amount of polluted material that can be delivered by the 1G requires that the original cluster was some 10 or more times more massive than it is today, i.e. that each cluster has lost 90% or more of its initial mass. This is termed the "Mass Budget Problem". So far, no strong evidence either observational or theoretical exists for such an extreme mass loss.

Some models try to "alleviate" the mass budget problem. D'Ercole et al. (2010) postulate a different Initial Mass Function between 1G and 2G stars, with that of 2Gs being truncated at a mass close to or below ~ 8 M$\odot$, thus reducing the mass budget and avoiding supernova pollution from one 2G star to another. However, this theory remains unproved(Renzini et al. (2015)).

Marcolini et al. (2009) also investigated formation models where the abundances of forming stars move from 2G to 1G, as star formation within the cluster proceeds.

Actually all models require huge amounts of He enrichment which are simply not observed. "None of the proposed scenarios can explain the multiple population phenomenon, hence alternative theories are needed".(Bastian et al (2015)). However, such models serve as a useful attempt at trying to understand the nature of MPs.

Figure 11: Comparison between MP scenarios and observations. "As can be seen, no model does particularly well when compared to observations." Source: Bastian & Lardo (2018)

In the rest of this thesis, we will refer to 1G and 2G stars in the above context but recognize that we are still a long way from a successful theory. For that reason a lot of observational evidence, like Frelijj et al.(2017) and the two studies in this thesis, is needed to develop a theory capable of explain the multiple population phenomenon.

3.2.3 Abundance differences in Globular Clusters

A key feature of MPs in CGs are the light elements abundance variations between 1G and 2G stars. Osborn(1971) found a variation in CN among RGB stars. This was the first detection of abundance variations, long before the discovery of MPs.

A decade after, Norris et al. (1984) found an anticorrelation between CN and CH on the RGB. Further studies, like Smith & Norris (1984) and Martell & Smith (2009) among others, proved these two abundance variations to be a feature of GC only, since they did not find inhomogeneities in Open Clusters.

These were found not to be the only abundance differences: Cohen(1978) was the first one to find a difference in abundance of Na in GCs. Several years later, Cottrell & Da Costa(1981) found a correlation between CN and Na and Al. Sneden et al. (1992) found an anticorrelation between CN and O, and a correlation between CN and Na. Following the (admittedly flawed) formation scenarios seen in the past section, the differences of chemical abundances of 1G and 2G stars can be explained as follow:

1) 1G have normal levels of He, C, N, O, Na, Al and Mg, similar to field stars.

2) While the CNO cycle tends to convert their C and O into N, their Na is enriched by the $^{22}Ne(p,\gamma)^{23}Na$ reaction.(Lee (2010)), He is enriched via the CNO cycle, and in the most massive stars Al is enriched by the MgAl cycle.

3) 1G intermediate-mass stars become AGB stars.

4) The primordial pollution via stellar winds of these 1G intermediate-mass AGB stars provides these element abundances to the proto-stellar clouds of the 2G of stars.This should then lead to a 2G with enhanced He, N, Na and Al and depleted C, O and Mg compared to the 1G.

Comparing the spectra of a 1G versus a 2G star the abundance differences can be seen. The following image (figure 12) shows representative spectra of first and second generation red giants with the same atmospheric parameters and only differing in the content of the light elements C, N, O and Na, in amounts typical of 1G and 2G stars.
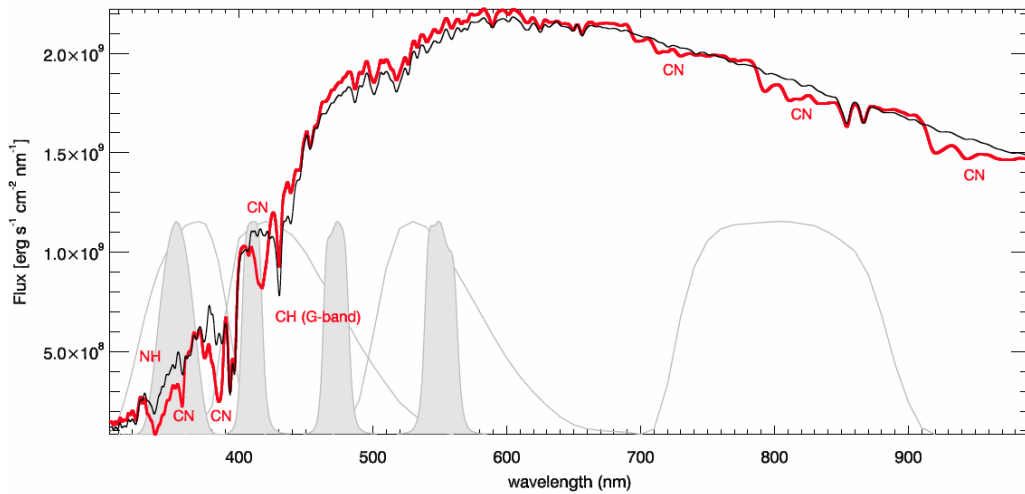
Figure 12: Comparison between the synthetic spectra of a First(black spectrum) and Second generation star(red spectrum) from the Red Giant Branch illustrating the variation of C, N, O and Na. Various photometric filter responses are also shown. Source: Sbordone et al (2011).

The spectra are substantially different in the molecular bands formed by these elements, particularly in the UV-blue portion of the optical. A filter covering any or all of these bands should therefore be sensitive to these varying band strengths, thus revealing MPs photometrically.

3.2.4 Evidence of Multiple Populations in Globular Clusters

A common method to find MPs with spectroscopy is to identify abundance correlation or anticorrelations between first and second generation stars. The most famous is the Na-O anticorrelation.

Carretta et al. (2009) realized a Na-O anticorrelation study using spectra from FLAMES/GIRAFFE of more than 2000 RGB stars in 19 GCs - see Figure 13. Their detections are indicated as open circles. Although they could not measure O abundances in all stars, they placed upper limits to O abundances, represented as arrows. Star-to-star error bars are indicated in each panel at the bottom-left. This evidence show that all these clusters present an Na-O anticorrelation. However, the slope and shape of the anticorrelation varies for each cluster. This was the first convincing evidence that MPs were not just an isolated phenomenon occurring in a few special cases but instead a general, possibly universal, phenomenon found in a wide variety of GCs.
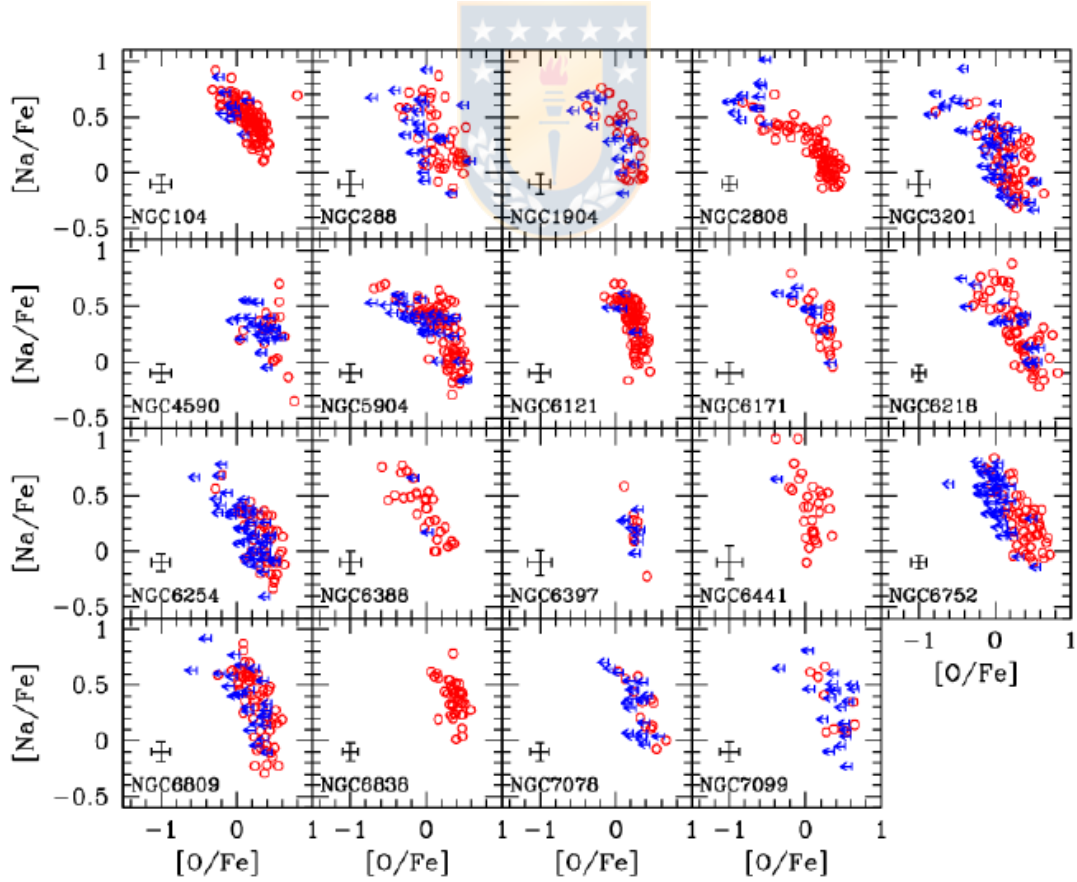
Figure 13: Na-O Anticorrelations of 19 GCs observed from Carretta et al (2009). Upper limits in O abundances are shown as arrows, detections are indicated as open circles. Source: Carretta et al (2009)

As said before, and looking at figure 12, some filters facilitate the photometric study of MPs. Sometimes these are demonstrated by distinct multiple sequences, as seen below (figure 14) in the case of ω Cen, and sometimes MPs are distinguished photometrically by spread in color in a given filter combination that is significantly wider than the observational errors, indicating an intrinsic variation in abundances within the cluster.(Figure 15)
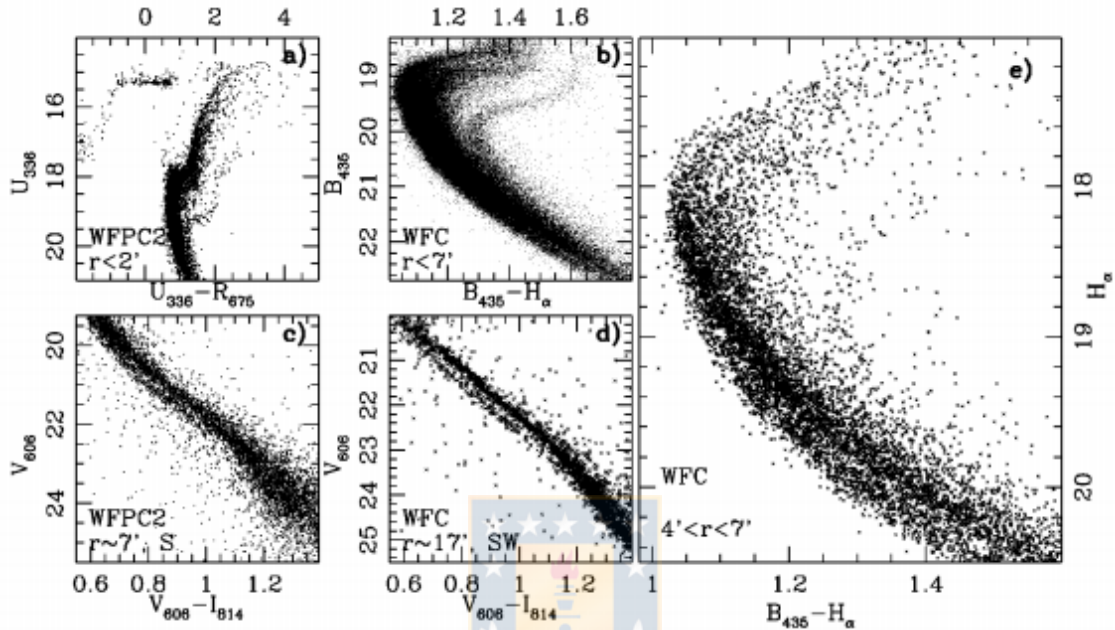
Figure 14: Color-Magnitude Diagrams of Omega Cen showing Multiple sequences, indicating the presence of MP. Source: Bedin et al. (2004).
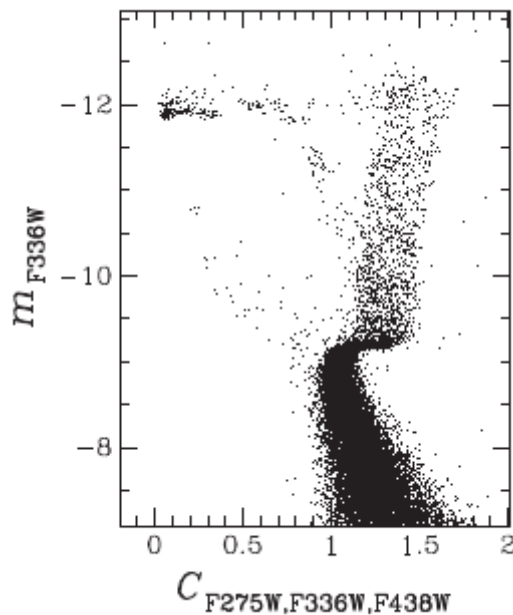
Figure 15: CMD of NGC 5986 using the "Magic trio" of filter from Piotto et al. (2015). The CMD doesn't show distinct sequences but a significantly wide RGB. Source: Piotto et al. (2015)

Piotto et al. (2015) realized a study of 57 GCs using the "Magic trio", as part of the HST GC Treasury Survey. This "magic trio" consists in a combination of three filters F275W, F336W and F438W with which Milone et al. (2013) defined a pseudo-color $C_{F275W,F336W,F438W} = (m_{F275W} - m_{F336W}) - (m_{F336W} - m_{F438W})$ that proved to be quite efficient in the separation of multiple sequences. The reason why F275W, F336W and F438W work so well is given by Milone et al. (2012): The F275W passband includes an OH molecular band, F336W an NH band, and F438W CN and CH bands, as illustrated in Figure 16.

The reason why F275W, F336W, and F438W work so well is because the F275W passband includes an OH molecular band, F336W an NH band, and F438W CN and CH bands. The 1G stars, which are oxygen- and carbon-rich and nitrogen-poor, are relatively faint in F275W and F438W, but bright in F336W. Conversely, 2G stars, whose material has been CNO-cycle processed, are oxygen- and carbon-poor but nitrogen-rich. As a consequence, they are relatively bright in F275W and F438W but faint in F336W.
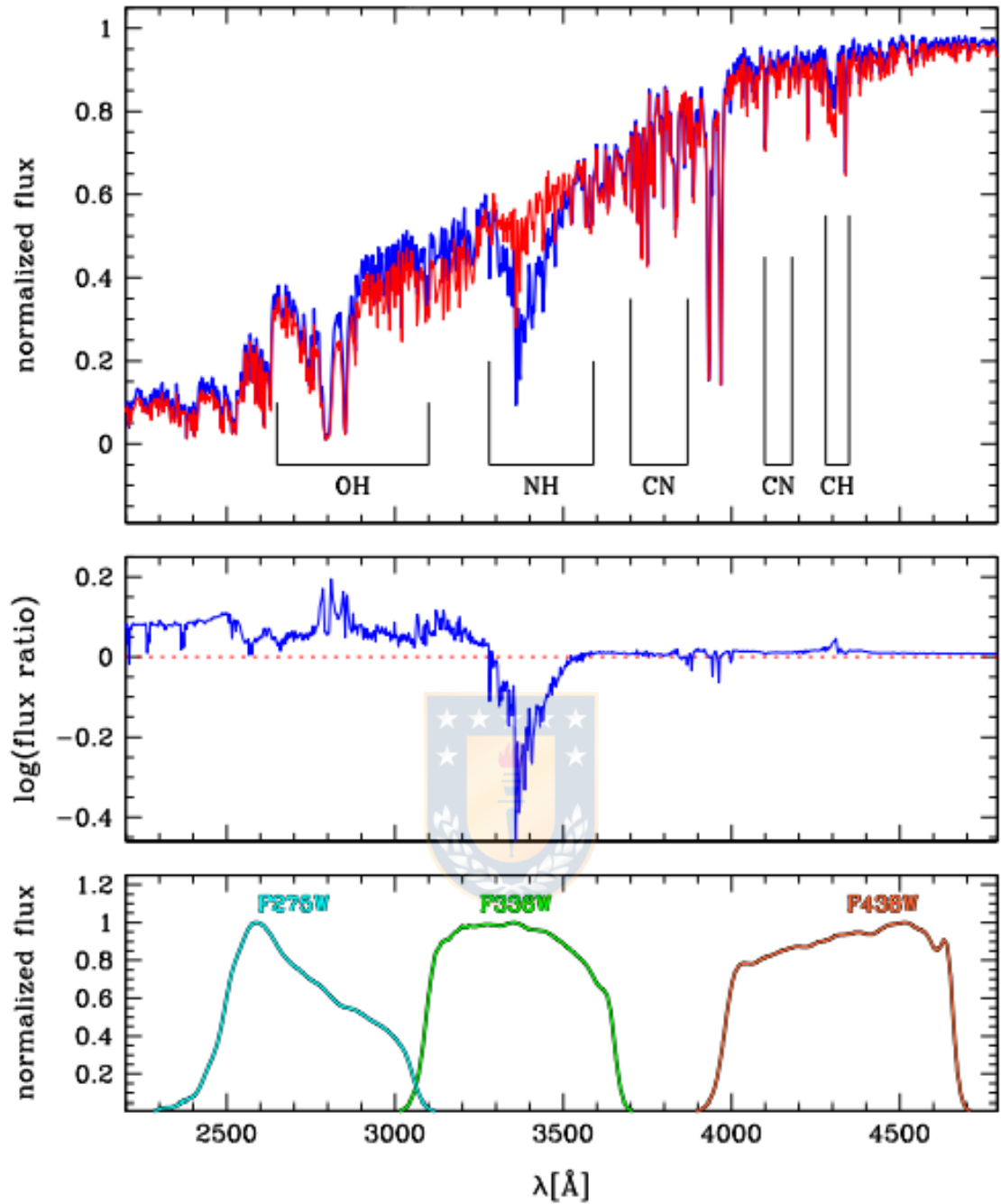
Figure 16: Upper panel: Simulated spectra of 1G star(N-poor) RGBa in NGC 6752(red) and a second generation(N-rich) RGBc star (Milone et al. 2010). Middle panel: flux ratio of the two spectra reproduced in the upper panel. Lower panel: bandpasses of WFC3/UVIS with F275W, F336W, and F438W. Source: Piotto et al. (2015)

Two years later Milone et al. (2017) would take the data from Piotto el al. (2015) to create Chromosome maps: "A pseudo-two-colour diagram built with a suitable combination of stellar magnitudes in the F275W, F336W, F438W, and F814W filters". These chromosome maps would reveal that there are two types of GCs: Type I, defined as those GCs whose stars separate in two distinct groups

that we identify with the 1G and 2G, and Type II GCs where the 1G and/or the 2G sequences appear to be split, hence displaying more complex chromosome maps. Also, this type of cluster presents a double Sub Giant Branch in the CMD. Figure 17 shows Chromosome maps of both Type I and II GC. As can be seen, the position in Figure 17b of the 1G and 2G stars determined in Figure 17a, clearly shows them to indeed be 1G and 2G stars, thus corroborating their distinct positions in Figure 17a.
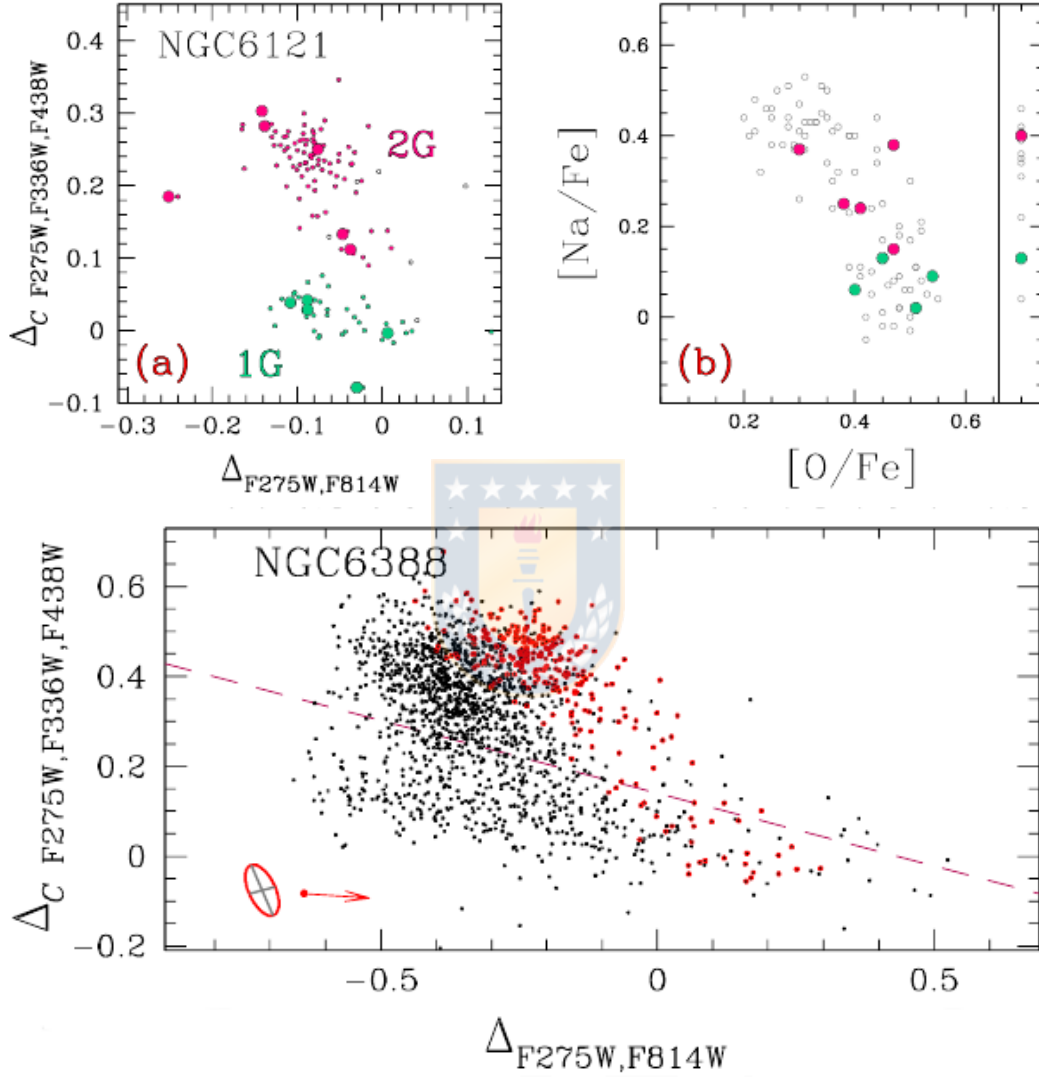
Figure 17: Top: Panel (a) shows a chromosome map of RGB 1G(aqua) and 2G(magenta) stars in the type I cluster NGC 6121. Large aqua and magenta dots indicate 1G and 2G stars studied spectroscopically by Marino et al. (2008), and whose [Na/Fe] versus [O/Fe] anticorrelation is shown in panel (b) using the same symbols. Bottom: Chromosome map for RGB stars of NGC 6388. The magenta dashed line is used to separate 1G from 2G stars. Red points indicate red-RGB stars, revealing a more complex chromosome map than type I GCs, leading to its classification as a Type II cluster. Source: Milone et al. (2017)

3.2.5 The Washington Filter System

The Washington System developed by Canterna (1976) and Geisler (1996) is another useful method to uncover MPs, it consist in four filters (C, M, T_1, T_2) initially developed to obtain accurate temperatures, metal abundances and a CN index for G and K giants.
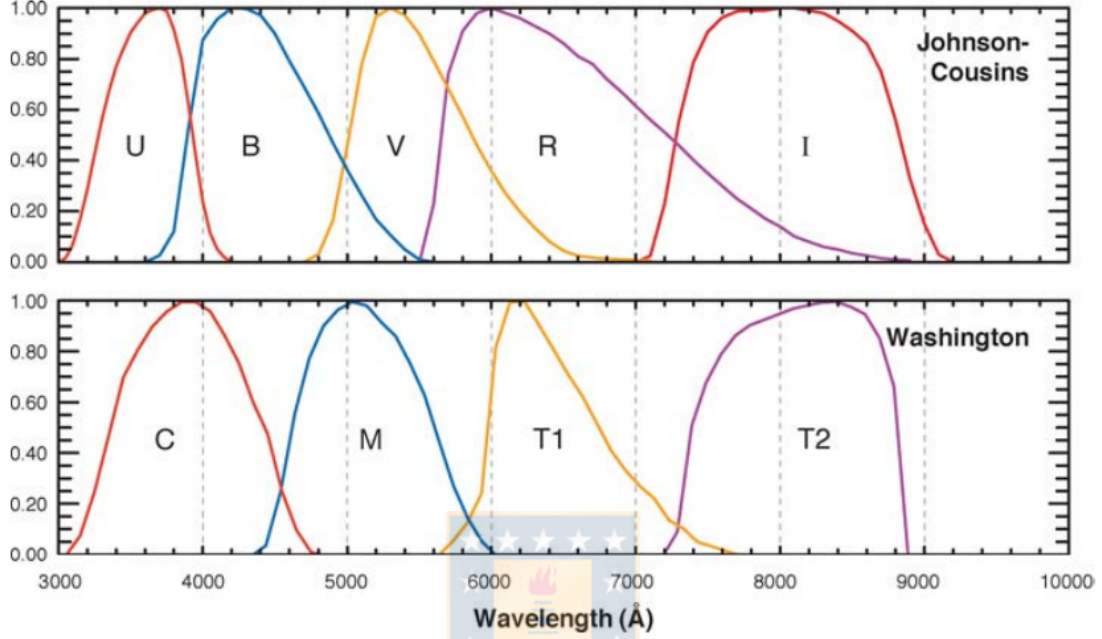
Figure 18: Comparison of the spectral response between the classic Johnson-Cousins Filter system and the Washington Filter system. Source: Bessel (2005)

The most important filter for this study is the C filter which indeed was designed to detect Multiple Populations, although at the time they were not designated as such. The C filter was added to the system to provide a measurement of CN/CH enhancements or depletions independent of the metallicity index measured by the M filter, just at the time when CN/CH variations within clusters were being discovered. The ability of ground-based C photometry to detect Multiple Populations in Globular Clusters was first explored in Cummings et al. (2014). They found that the filter was indeed very useful in this regard, given both the UV sensitivity as well as the high efficiency of this broad band (FWHM >1000 Å), high throughput filter.

The Washington C filter is very broad and covers the wide range from about 3300 - 4500 Å, where the largest flux differences exist between first and second generation stars due to the strong molecular bands of NH, CN and CH, making it very efficient for this task.

This filter is similar to the classical Johnson filter U, but much wider and with a higher peak transmission. It is also centered further to the red, making it less sensitive to atmospheric extinction and interstellar reddening. It is even more efficient with respect to the intermediate-band Sloan u and Stromgren u filters (Table 1). Tests at the telescope have shown that the C filter detects 3-5 times as many photons as the U filter for a typical red giant.
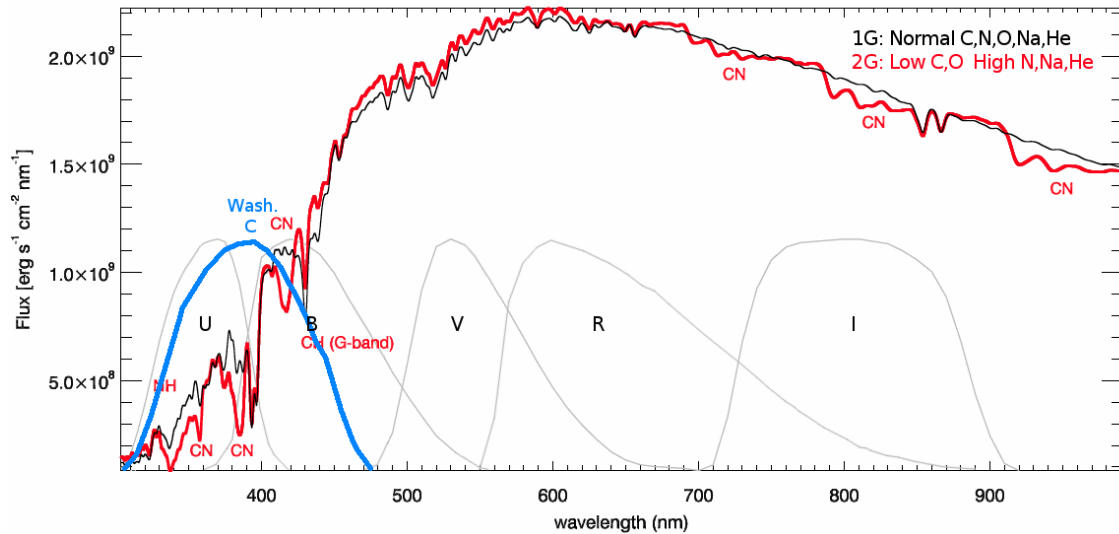
Figure 19: Modification of Figure 12 with the filter C added. The Washington C filter covers the entire region of the largest difference between 1G and 2G stars, in the ground-accessible UV due to the various molecular bands. Source: Cummings et al. (2014)

Filter	Central λ	FWHM (λ)	Peak Transmission	Source
Johnson U	3570	650	72.47%	1
Washington C	3850	1075	83%	1
SDSS u	3600	400	65.49%	1
Stromgren u	3537	278	38%	2

Table 1: Comparison of UV filters with the Washington filter C. Source: Cummings et al.(2014).

Cummings et al. (2014) investigated the utility of the Washington C filter to find Multiple Populations in NGC 1851, getting very good results using a telescope of only 1 meter aperture, in particular the Swope Telescope at Las Campanas Observatory.

They found a spread in the RGB, with a main locus and a relatively small number of stars dispersed to the red. They also studied the MS, finding evidence of a similar color distribution there as well. In addition, their analysis of radial distributions found a significant difference between the blue and red MSs(p-value=0.0), with the latter being more centrally concentrated. All these studies were consistent with previous studies in NGC 1851, like Zoccali et al. (2009).

Thus, this system provides a good ground-based alternative to the heavily oversubscribed Hubble Space Telescope and is more efficient than other ground-based filters.
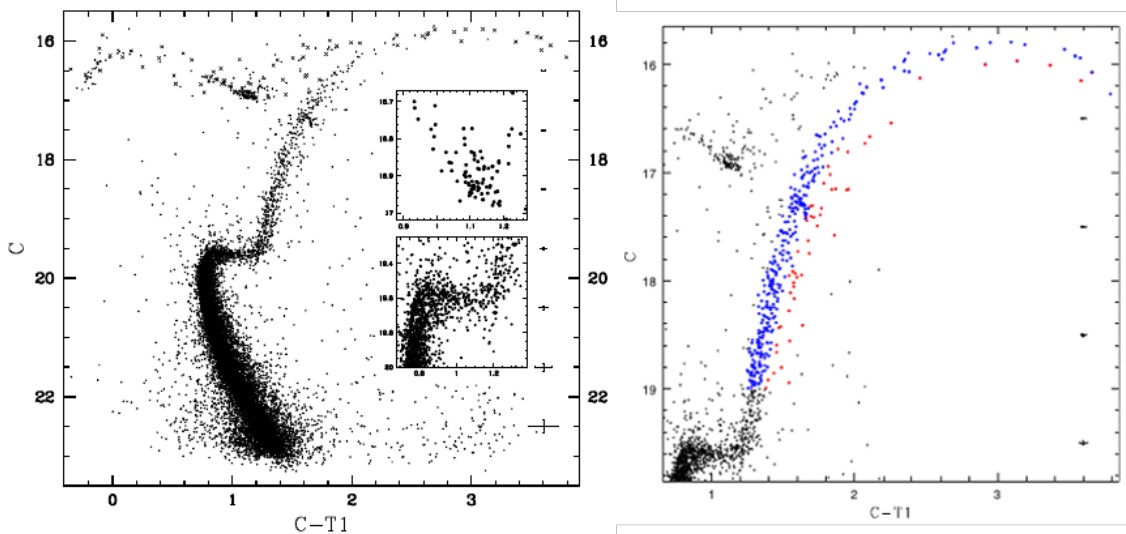
Figure 20: At left: CMD of NGC 1851 using $C-T_1$ vs C, the HB and RGB have been zoomed. Right: a zoom to the RGB clarifying the redder and bluer populations. Source: Cummings et al. (2014)

3.3 Ruprecht 106

With such evidence as discussed above, it is very tempting to say that all GCs have MPs, but several GCs seem to host only Simple Stellar Population(SSP)(i.e E3 (Salinas & Strader 2015) and Terzan 7 (Tautvaivien et al. 2004)), although actually some of them do not have enough evidence to confirm this hypothesis. Particularly, Villanova et al. (2013) showed convincing evidence suggesting that Ruprecht 106 is a genuine old, massive GC with only a single population, thus opening new questions about the nature of GCs and MPs. (Figure 21)

According to Harris (1996)(2010 edition) Rup106 is a GC with coordinates α(J2000): $12^h 38^m 40.2^s$ and δ(J2000): -51°09'01", located at 21.2 kpc from the Sun and 18.5 kpc from the Galactic centre. It has a metallicity [Fe/H] = -1.68, an Heliocentric Radial Velocity RV = -44 $\pm$ 3 km s^{-1} and a Foreground Reddening E(B-V) = 0.2.

As mentioned, Villanova et al. (2013)(hereafter V13) realized a spectroscopic study in Rup106 showing that all 9 stars studied showed no Na or O variation, and of course therefore no sign of the Na-O anticorrelation which is the trademark of MPs, concluding that Rup106 is to date the best case for a GC that lacks MPs. This has been well supported by an independent photometric study by Dotter et al. (2018). V13 also show that Rup106 has an extragalactic origin since its very low Na and α-element abundances only match those of the Magellanic Clouds and of the Sagittarius Galaxy. Both studies together present strong evidence of Rup106 hosting only SSP, but the 9 targets from V13 are not enough to assure that the cluster has no chemical spread at all. The first part of this work tries to provide, along with V13, enough spectroscopic and photometric evidence to demonstrate that Rup106 is indeed a SSP cluster or at most possesses only a single star from a different population, which could open again the controversy about this cluster.

20
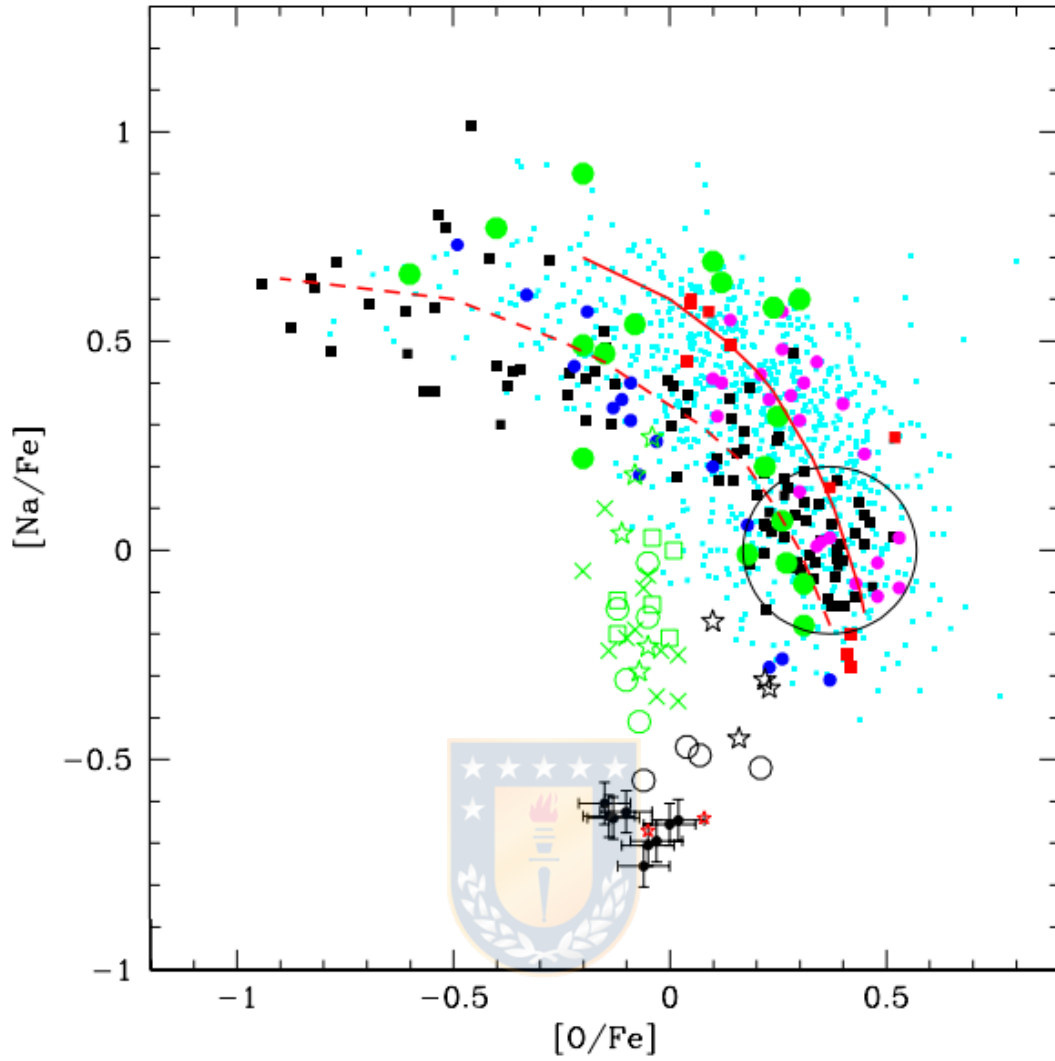
Figure 21: [Na/Fe] vs. [O/Fe] in GCs as well as intermediate-age Large Magellanic Cloud clusters (green open symbols). Filled black circles and open red stars are samples from Ruprecht 106 by Villanova et al. (2013) and Brown et al. (1997) respectively, while all the other figures are samples from other clusters. The Rup 106 stars all lie within the measurement errors of the same abundance for both O and Na. Source: Villanova et al. (2013)

3.4   NGC 7099 (M 30)
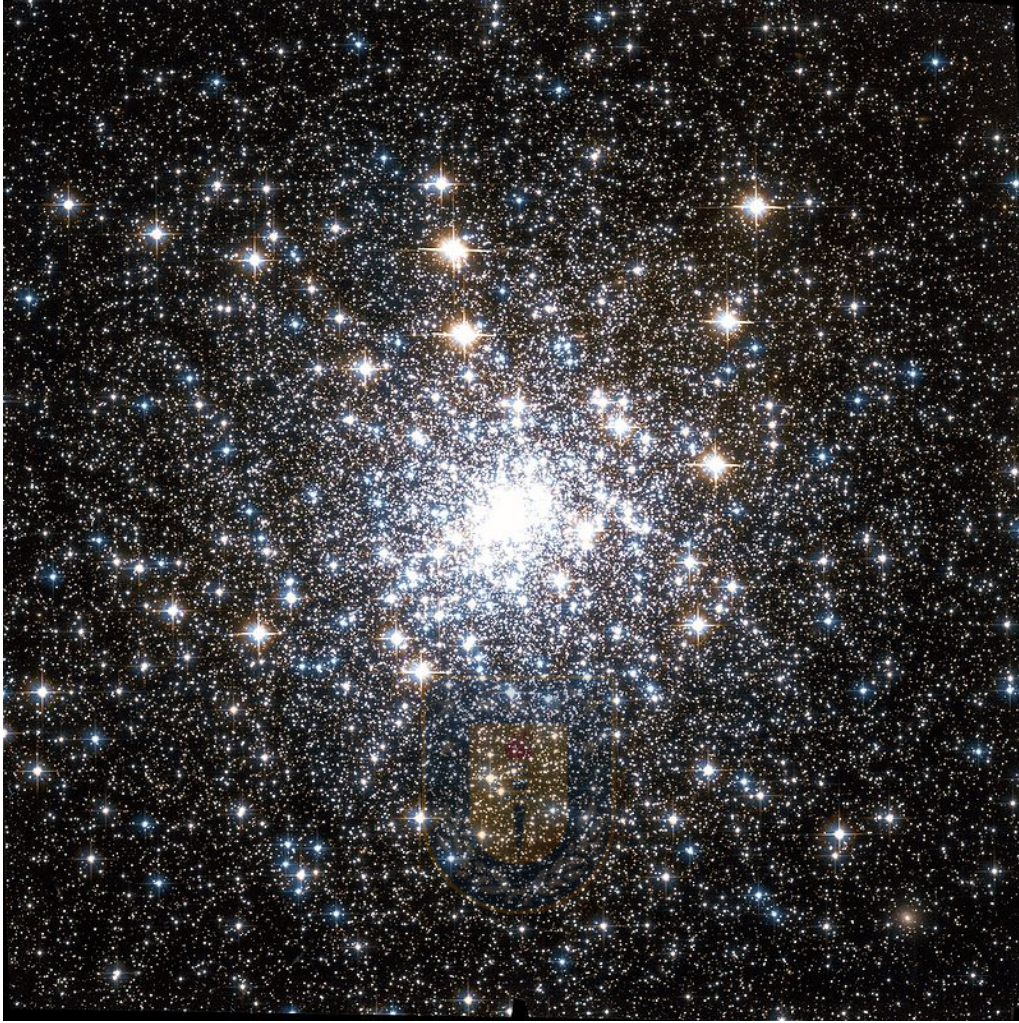
Figure 22: NGC 7099 (M30). Source: http://freestarcharts.com

This very metal poor cluster([Fe/H]= -2.27) is situated in the galactic halo at 8.1 Kpc from our Sun, with coordinates(epoch J2000):

$$RA : 21^h \, 40^m \, 22.12^s$$

$$Dec : -23 \, 10' \, 47.5''$$

Its integrated V magnitude is 7.19 and it has a foreground reddening of only 0.03.(Harris 1996 (2010 edition)) This last information was the reason of why we chose this cluster, because it means that differential reddening corrections are not needed. Also, at the time we took the observations, little other work had been done photometrically on MPs in this cluster, which is also among the most metal-poor in the Galaxy.

It has an estimated age of 12,9 Gyrs(Forbes & Bridges(2010)) and a mass of 1.6×10^6 Solar Masses (Vande Putte & Cropper (2009)); making it a massive cluster and thus one that should fall within Valcarce and Catelan case 2 or possibly 3.

Previous work in this GC concerning MPs was made by Carretta et al. (2009) using 29 RGB stars who found spectroscopically a Na-O anticorrelation, showing the presence of MPs.(Figure 21)
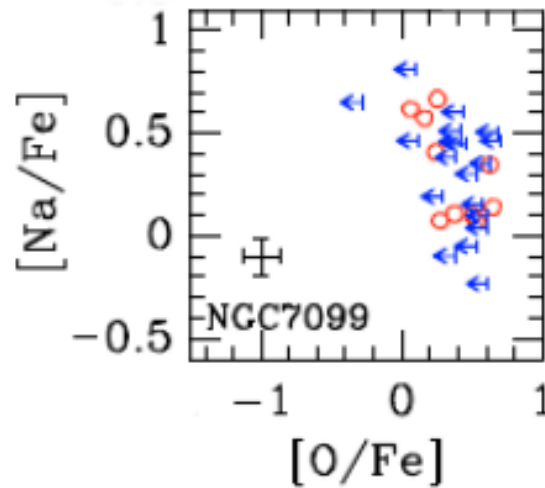
Figure 23: Plot from Carretta et al. (2009) The sample of 29 stars shows a Na-O anticorrelation. Source: Carretta et al. (2009)

We saw before, that photometrically Piotto et al. (2015) analyzed 57 GCs using the magic trio of filters (F275W, F336W and F438W) using data from the HST. These studies included NGC 7099. Although their CMD didn't show the typical split of the sequence, it does show a very broad Red Giant Branch.
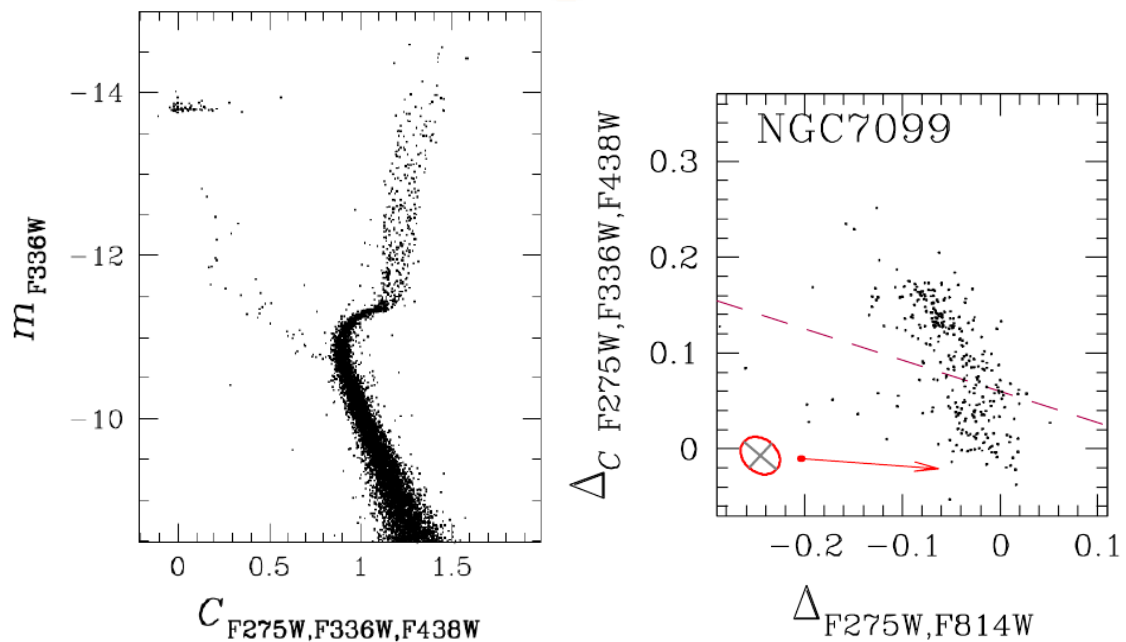
Figure 24: Left: Color-Magnitude Diagram from Piotto et al. (2015). The RGB is very wide, indicating the presence of MPs. Based on data obtained by the Hubble Space Telescope. Right: Chromosome map of NGC 7099, the magenta dashed line separates the 1G from the 2G. Sources: Piotto et al. (2015), Milone et al.(2017)

Milone et al.(2017) used the information from Piotto et al.(2015) to create a chromosome map of all the GC studied, included NGC 7099, this chromosome map can distinguish the 1G from the 2G more easily than the CMD.

Frelijj et al. (2017) found a real spread along the RGB in all the CMDs that included the C filter, with $C-T_1$ showing most clearly both populations, $C-T_2$ still differentiated them substantively, but T_1-T_2 showed no significant intrinsic spread. We also found that the bluer population, expected to be FG stars, is only about 20% of the total population of the cluster. But the most intriguing finding was respect to the radial distribution of the MPs. Where we found a more concentrated bluer population instead of the redder. This fact contradicts most of the actual formation scenarios for MPs.
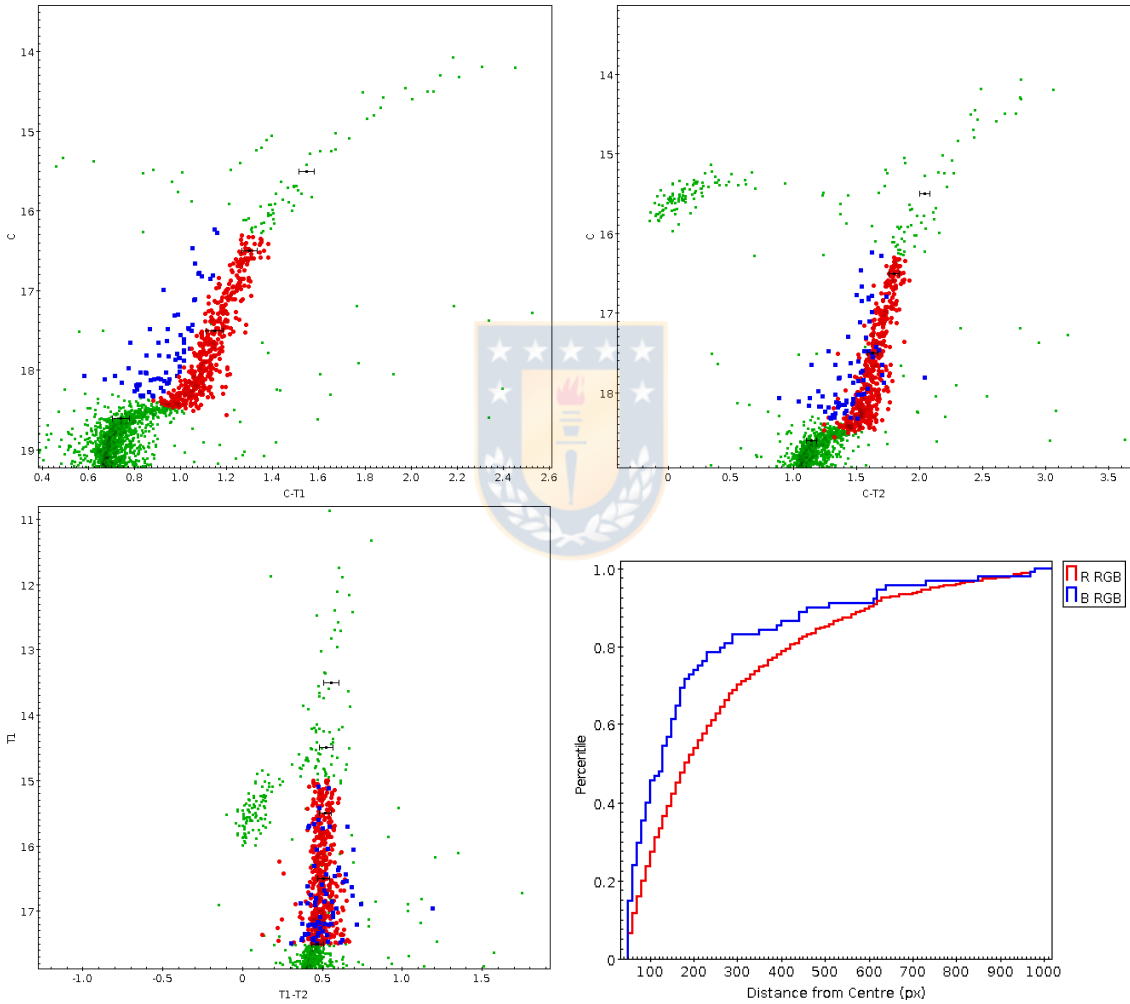
Figure 25: Results from Frelijj et al.(2017) The two diagrams on the top and the bottom-left show both 1G(blue) and 2G(red) in different colors. the bottom right panel shows the radial distribution of the populations showing, opposed to the expected, a more concentrated 1G. Source: Frelijj et al.(2017)

The second part of this work tries to improve the detection of these populations, and verify(or deny) the findings done in Frelijj et al.(2017), and test the efficacy of a different combination of Washington filters for detecting MPs.

3.5 NGC 1851

As explained earlier, NGC1851 has been widely studied. Hesser et al. (1982) found that three out of eight bright red giant branch (RGB) stars have extremely strong CN bands, enhanced SrII and BaII lines, and lie systematically on the red side of the RGB. Almost 20 years later, Saviane et al. (1998) confirmed the bimodal nature of the HB of NGC 1851.

The boom of studies of NGC1851 began 10 years later, when Milone et al.(2008) and Cassisi et al.(2008) studied a recently found double SGB which, in addition with the 2 studies mentioned earlier, apparently implied 2 different subpopulations with either an age difference of about 1 Gyr, or different (C+N+O) abundances. While Yong et al.(2009) supported the latter theory finding a C+N+O spread of 0.6 dex (with similar results in Yong, Grundahl & Norris(2014)), Villanova et al.(2010) did not find any spread in C+N+O in the red RGB, but did find a spread in their content of Ba.

On the other hand, Milone et al.(2009) did not find significant differences in the radial distributions of both SGBs.

It is worth mentioning that Yang et al.(2008), Villanova et al.(2010), Carreta et al.(2010) and Carretta et al.(2011) found an Na-O anticorrelation in the RGB of NGC 1851.

Han et al.(2009) found that the RGB and SGB of NGC1851 are clearly split into two in the U - I color, being the faint-SGB and the Red-RGB connected. Lardo et al.(2012) obtained a similar split using a combination of Strömgren colours ((u+v)−(b+y)) and later, Cummings et al.(2014) found a similar split, in considerable less observing time, using the Washington Color $C - T_1$. Piotto et al.(2015) improved the reality of the sequences using the magic trio.

Bekki & Yong (2012) showed that a merger scenario for NGC 1851 is dynamically plausible, and Campbell et al.(2012) found a complex quadrimodal distribution of CN molecular line strengths of RGB and asymptotic giant branch (AGB) stars, which could be the result of the superposition of two 'normal' bimodal populations.

Finally, Milone et al.(2017) took the CMD of NGC1851 from Piotto et al.(2015) to create a chomosome map, with which they found that the redder RGB and fainter SGB of NGC1851 are characteristics of type II GCs, and classified it as such.

One of the goals of the second part of this work is to see how much our new method improves the separation of the red-RGB stars.
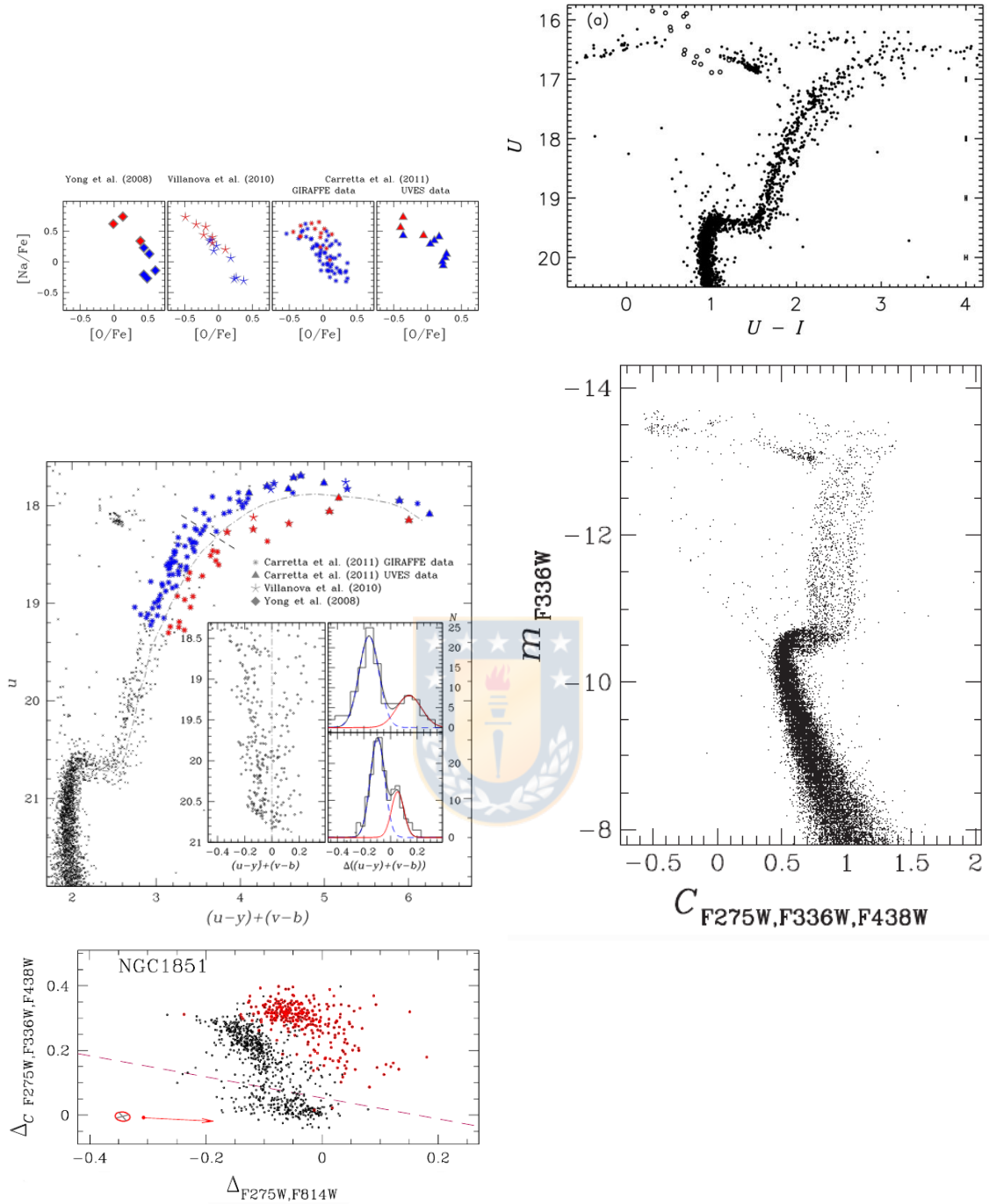
Figure 26: Results of NGC1851 from previous studies. Top left: Na-O Anticorrelation in the RGB according to different studies. Top Right: Double SGB/RGB found by Han et al.(2009) in the U-I vs U).Middle left: CMD from Lardo et al.(2012) showing the double SGB/RGB in NGC 1851. Middle right: CMD from Piotto et al.(2015) using the Magic Trio. Bottom : Chromosome map from Milone et al.(2017): The magenta dashed line separates 1G from 2G stars. Red points indicate red-RGB stars. Source: Lardo et al.(2012), Han et al.(2009), Piotto et al.(2015), Milone et al.(2017)

4 Part 1: Searching for Multiple Populations in the Globular Cluster Ruprecht 106

4.1 Introduction

The classical paradigm of Galactic globular clusters (GCs) being simple stellar populations has been changed dramatically by observational evidence. The presence of chemical inhomogeneities in their light elements, like a spread in Na or O extensively studied by Carretta et al.(2009), led some authors to create different theories to try to explain this behaviour (D'ercole et al.(2008), Renzini et al.(2015), Bastian et al.(2013)), but to date no scenario satisfies all the observations. As mentioned, the abundance analysis (obtained through spectroscopy) like the Na-O, Mg-Al and C-N anticorrelation is one of the strongest weapons to determine whether a GC possesses MPs since different populations present different chemical abundances.

Photometry is a different approach to search for MPs when spectroscopic chemical abundances are not available. We can use it to analyze large groups of stars simultaneously. UV filters in particular have proved to be sensitive to differences in chemical abundances of light elements. Bedin et al.(2004) used HST observations to prove that using the right combination of filters it is possible to distinguish between multiple main sequences and/or sub-giant and/or giant branches in almost all GCs. The most popular works involving this technique was Piotto et al.(2015) who used an improved combination of the UV/blue WFC3/UVIS filters F275W, F336W and F438W, the so called 'magic trio', to analyze 57 GCs. All of them presented split RGBs and often MS sequences or, at least, a great broadening in some parts of the sequences. Other filters like the C filter from the Washington Filter system (Canterna 1976) have proved to be very sensitive in discriminating the presence of MPs from the ground (Cummings et al. 2014, Frelijj et al. 2017). But like most cases, there is at least one exception to every rule. A bunch of GCs seems to host a Simple Stellar Population(SSP)(i.e E3 (Salinas & Strader 2015), Terzan 7 (Tautvaivien et al.2004), Ruprecht 106 (Villanova et al. 2013), etc), although actually some of them do not have enough evidence to confirm this hypothesis. In this paper we are going to focus in one of these: Ruprecht 106 (hereafter Rup106).

According to Harris (1996, 2010 edition) Rup106 is a GC with α(J2000): $12^h38^m40.2^s$ and δ(J2000): -51º09'01", located at 21.2 kpc from the Sun and 18.5 kpc from the Galactic centre. It has a metallicity [Fe/H] = -1.68, an Heliocentric Radial Velocity RV = -44 $\pm$ 3 km s^{-1} and a Foreground Reddening E(B-V) = 0.2.

As mentioned, Villanova et al.(2013, hereafter V13) realized a spectroscopic study in Rup106 showing that all the 9 stars studied showed no Na-O anticorrelation, concluding that Rup106 is one of the few GCs that lacks to exhibit the phenomenon of MPs, which have been well supported by an independent photometric study by Dotter et al.(2018). V13 also show that Rup106 has an extragalactic origin since its very low Na and α-element abundances only match those of the Magellanic Clouds and of the Sagittarius Galaxy. Both studies together present strong evidence of Rup106 hosting only a SSP, but the 9 targets from V13 are not enough to assure that the cluster has no chemical spread at all. This paper tries to provide, along with V13, enough spectroscopic and photometric evidence to demonstrate that Rup106 is indeed a SSP cluster or that possesses perhaps only a single star from a different population, what could open again the controversy about this cluster.

This section is organized in this way: In subsection 4.2, we discuss our observations and data reduction from Photometry and Spectroscopy. In subsection 4.3 we detail the steps done to get Heliocentric Velocities and Proper Motions to filter our photometric catalogue from non members. We also describe the process we used to get the atmospheric parameters that are necessary to calculate abundances. Subsection 4.4 describes the abundance determination. Subsection 4.5 presents the photometric analysis we applied to determine whether Rup106 have MPs or not. Subsection 4.6 contains a study of its orbit, discussing the possible extragalactic origin of Rup106.

4.2 Data

4.2.1 Photometric Observations

The sample used for this work is composed of 21 images taken at the 1-m Swope telescope, Las Campanas Observatory, Chile. All of these images are from the same observing run in march 2014. The Swope telescope works with one CCD (E2V CCD231-84) which contains 4 amplifiers together forming a square of 4096x4112 pixels with a scale of 0.435 "/pix and a field of view of 29.7x29.8 arc minutes. The filters used for this work are the Washington C filter (Canterna 1976), the I_{KC} filter, and the Harris V and R filters. From the 21 images, 2 images were taken using the I filter, 5 using R, 6 images using V and 8 C.

Table 2 gives details of the exposures:

	N° (exposure time)
C	1(30s), 1(300s), 6(1200s)
V	2(10s), 1(100s), 3(400s)
R	1(10s), 1(100s), 3(400s)
I	1(10s), 1(100s)

Table 2: Time exposures and number of images per filter. Source: Own elaboration.

The FWHM of the images ranges between 1.37"-2.15" and the airmasses vary between 1.079-1.160. None of the 3 nights were considered photometric, hence standard fields could not be observed.

The data processing and reduction was performed according to Frelijj et al. (2017). We used IRAF [1] to process all the 4 quadrants of each image separately, more specifically its tasks ccdproc, zerocombine and flatcombine. After that a script was used to combine the four quadrants into one single image. The photometry was performed using DAOPHOT (Stetson 1987) since this program is designed to treat crowded fields. We obtained the PSF using the ~150 brightest non saturated and isolated stars in each frame. With a good PSF in hand we proceeded to run ALLSTAR on each image separately. Once finished, we aligned all the catalogues with DAOMATCH and DAOMASTER. The file with the transformation coordinates was used along with the images, the catalogs and psf files to finally run ALLFRAME (Stetson 1994). ALLFRAME made PSF-photometry simultaneously in all the frames to realize the best photometry. Finally, with each image catalogue that ALLFRAME returned, we apply aperture corrections realizing aperture photometry to the PSF-Stars and comparing it with the PSF-photometry.

We calibrated our data using the Catalog used in Dotter et al. (2011) available in the ACS GC Treasury database, where they took the filters F606W and F814W and converted them to ground-based filters V and I (hereafter V_{ground} and I_{ground}) using the relation from Sirianni et al. (2005). After matching them with our catalogue we selected a sample (Figure 27: Grey stars and slope for V and green for I) to derive the transformation equations in the form of:

$$V = (v - i) * m_1 + b_1 + v$$

---

[1] IRAF is distributed by the National Optical Astronomy Observatory, which is operated by the Association of Universities for Research in Astronomy (AURA) under a cooperative agreement with the National Science Foundation.

$$I = (v - i) * m_2 + b_2 + i$$

Where V and I are our calibrated magnitudes, m are the slopes, b are the y-intercepts of the line and v and i our instrumental magnitudes.
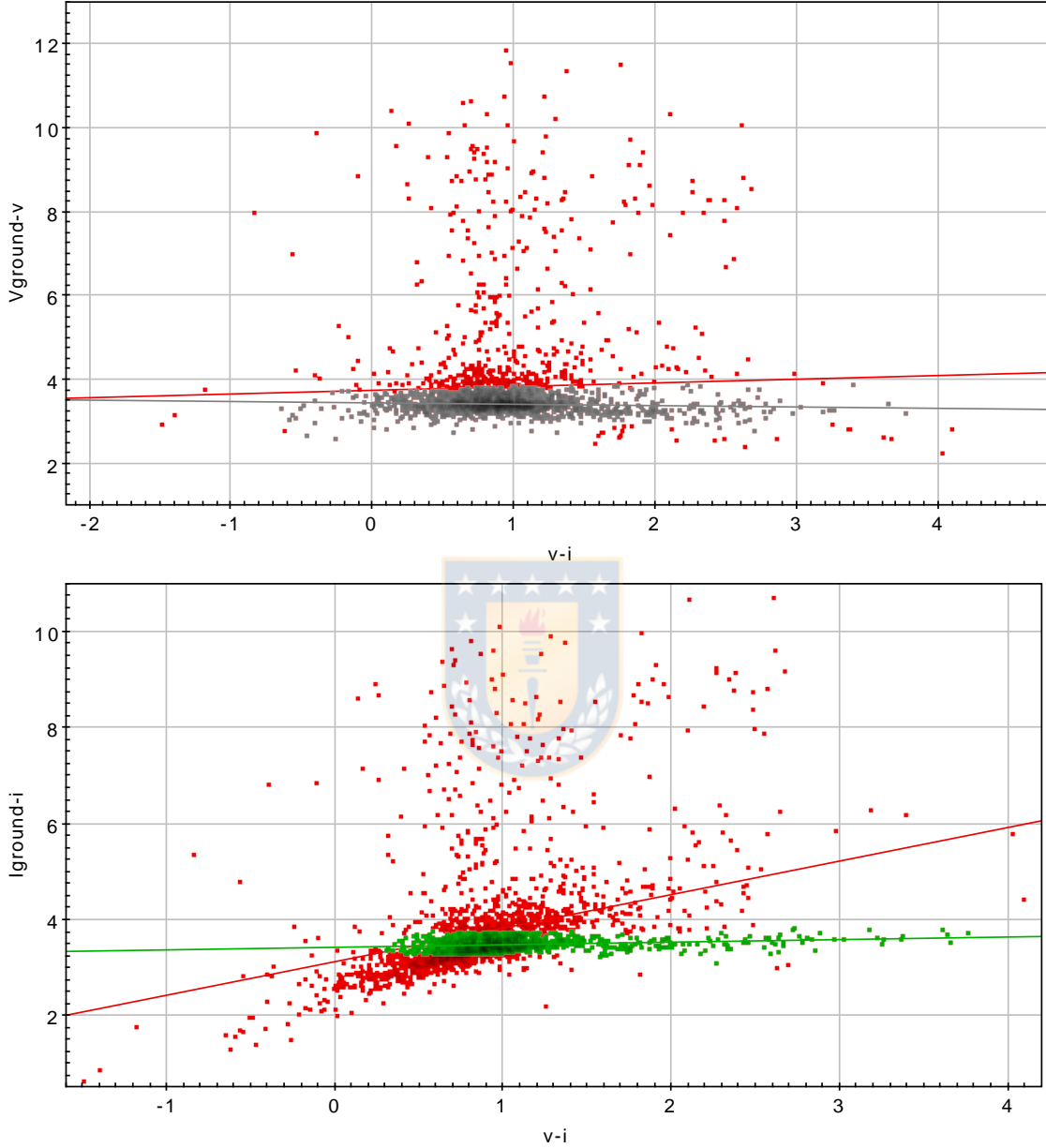
Figure 27: Calibration of the Instrumental Magnitudes, the sample and slope selected are the grey stars for V and green for I. Source: Own elaboration.

To verify the accuracy of the calibration we calculated the difference V_{ground}-V and I_{ground}-I. For the I filter we found a residual shift of 0.04 mag., so we subtracted it to all the calibrated I magnitudes (Figure 28).

Figure 29 shows a comparison between the V_{ground}-I_{ground} vs V_{ground} CMD from the Dotter et al. (2011) catalogue (blue dots) and our calibrated catalogue (red dots). Both HB and RGB are aligned, proving that the calibration is fine. We could not find a way to calibrate C and R filters, but for the purpose of this work this was not necessary.
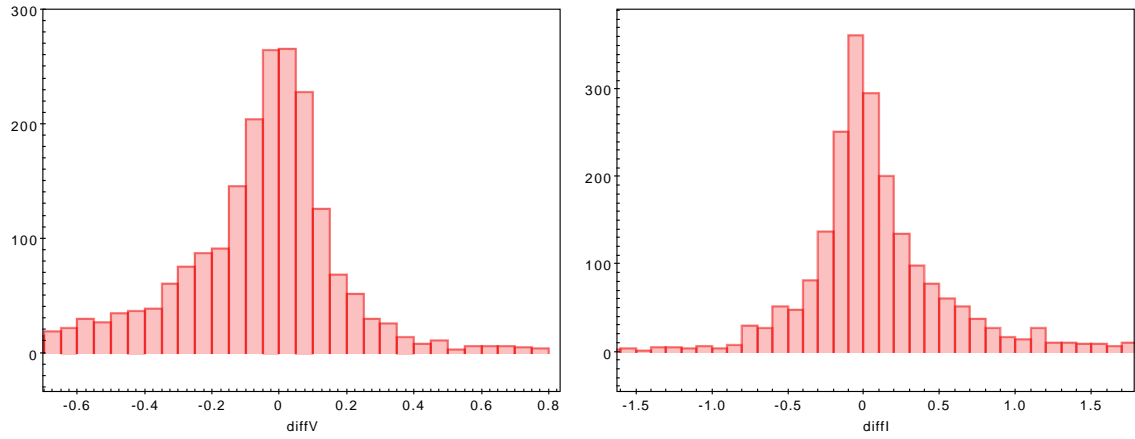
Figure 28: Difference in V_{ground}-V and I_{ground}-I. The I filter had a residual shift of 0.04 mag that was added to our magnitudes to match with those of I_{ground}. Source: Own elaboration.
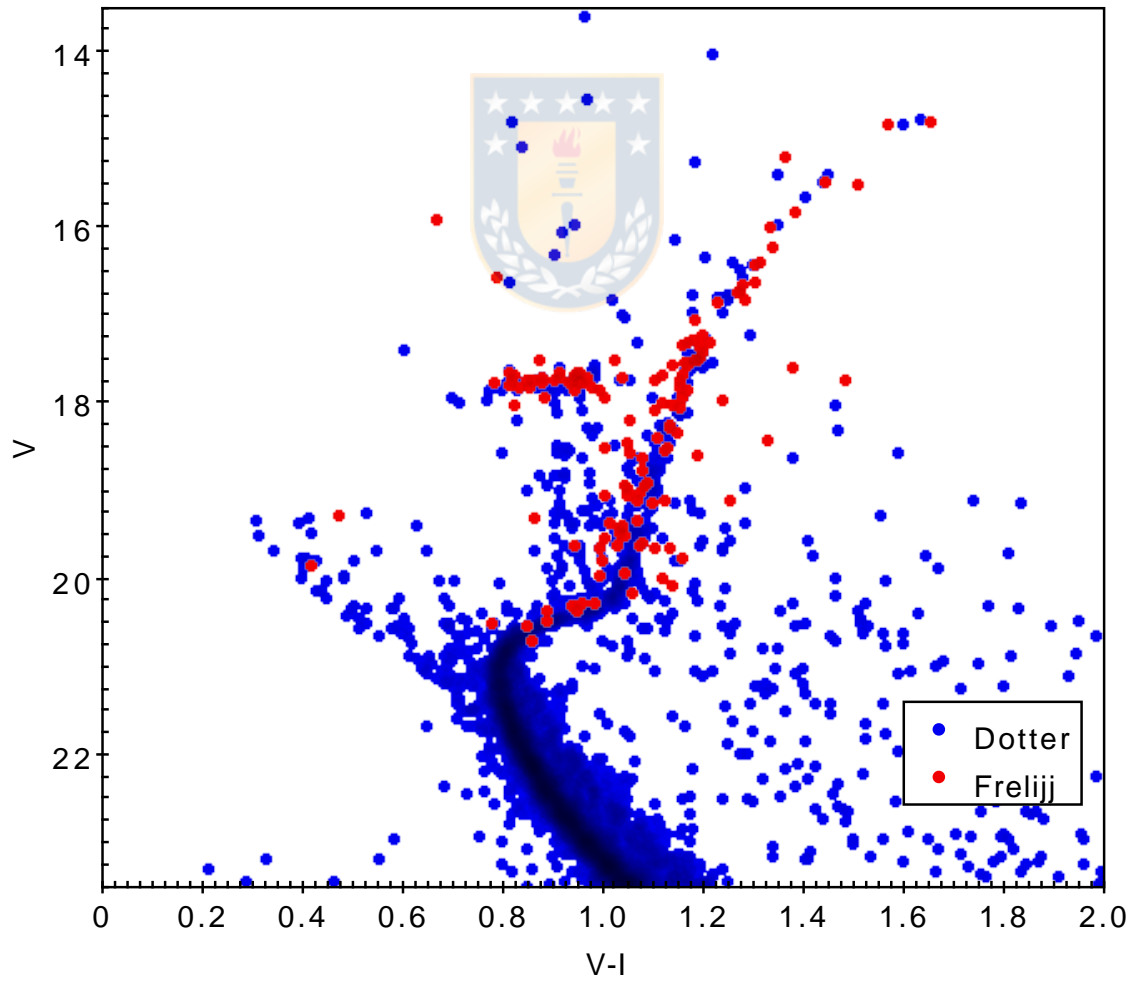
Figure 29: Plot overlapping a CMD using V_{ground}-I_{ground} vs V_{ground} from Dotter et al. (2011) and CMD with our calibrated V-I vs V. Source: Own elaboration.

Bonatto et al. (2013) shows that this cluster has a mean differential reddening of $\langle\delta\text{E(B-V)}\rangle = 0.026 \pm 0.010$ with a maximum differential reddening of $\delta\text{E(B-V)}_{\text{max}} = 0.051$, indicating that differential reddening corrections are small and we have chose not to make any.

Finally, the x/y coordinates of the standardized catalog were transformed to RA/Dec(J2000) using the xy2sky task from WCSTOOLS and a World Coordinate System created using 10 well separated stars from the reference frame with the IRAF tasks ccmap and ccsetwcs.

4.2.2 Spectroscopic Observations

Our spectroscopic data consist in observations from 2017 as part of the programme ID 098.D-0227(A) obtained using the medium-high resolution FLAMES-GIRAFFE Spectrograph installed in the UT2 (Kueyen) telescope in Paranal. The resolving power is R∼26400. Our targets were selected in the magnitude range V = 15.5 to V = 18.5 and they belong to the RGB (Figure 30). We observed 28 stars in the Wavelength range 6120-6405 Å. The exposure time was 2640 seconds per spectrum, and each star was observed 4 times, getting a total of 112 spectra.

The spectroscopic data were reduced using the GIRAFFE pipeline, with only a normalization, sky subtraction and a transformation from nm to Å remaining to do. These steps were done using IRAF tasks, specifically continuum, sarith and hedit. The 4 spectra of each star were combined using the task scombine to improve the S/N ratio.
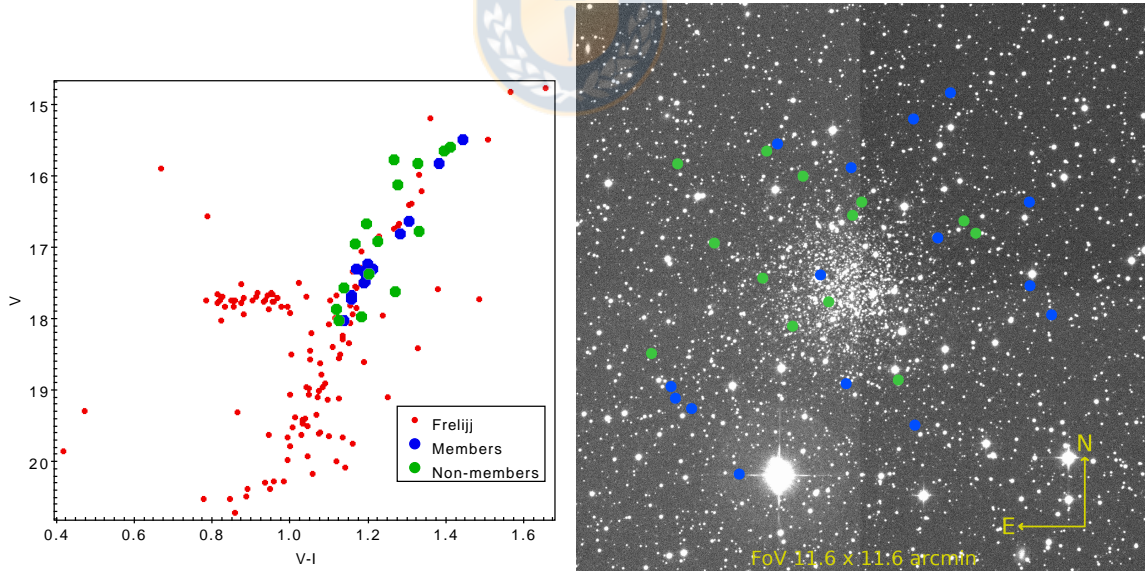
Figure 30: Top: Cluster Targets have been highlighted in the CMD. Members are shown as Blue dots while non-members are shown as Green dots. Bottom: Spatial distribution of the same targets in the cluster. Source: Own elaboration.

We measured observed radial Velocities using the IRAF fxcor package, with the help of a synthetic spectrum as a template calculated using typical RGB star parameters, i.e. $T_{\text{eff}} = 4500$ K, $\log(g) = 1.50$, $v_t = 1.50$ km s^{-1}, and the metallicity of the cluster ([Fe/H] = -1.50). These relative velocities were used to apply Doppler corrections through the IRAF task dopcor.

4.3 Data Analysis

4.3.1 Heliocentric Radial Velocities, Proper motions and membership

We obtained heliocentric radial velocities (RV) using the IRAF task rvcorrect. According to Figure 31, we consider possible cluster members those targets with RV between -45 and -35 km s^{-1}. This reduced our targets to 15. The mean heliocentric velocity of this sample is -38.99 $\pm$ 1.6 km s^{-1} with a standard deviation of 1.7 km s^{-1}. These values are in good agreement with V13 as it is shown in Figure 31.
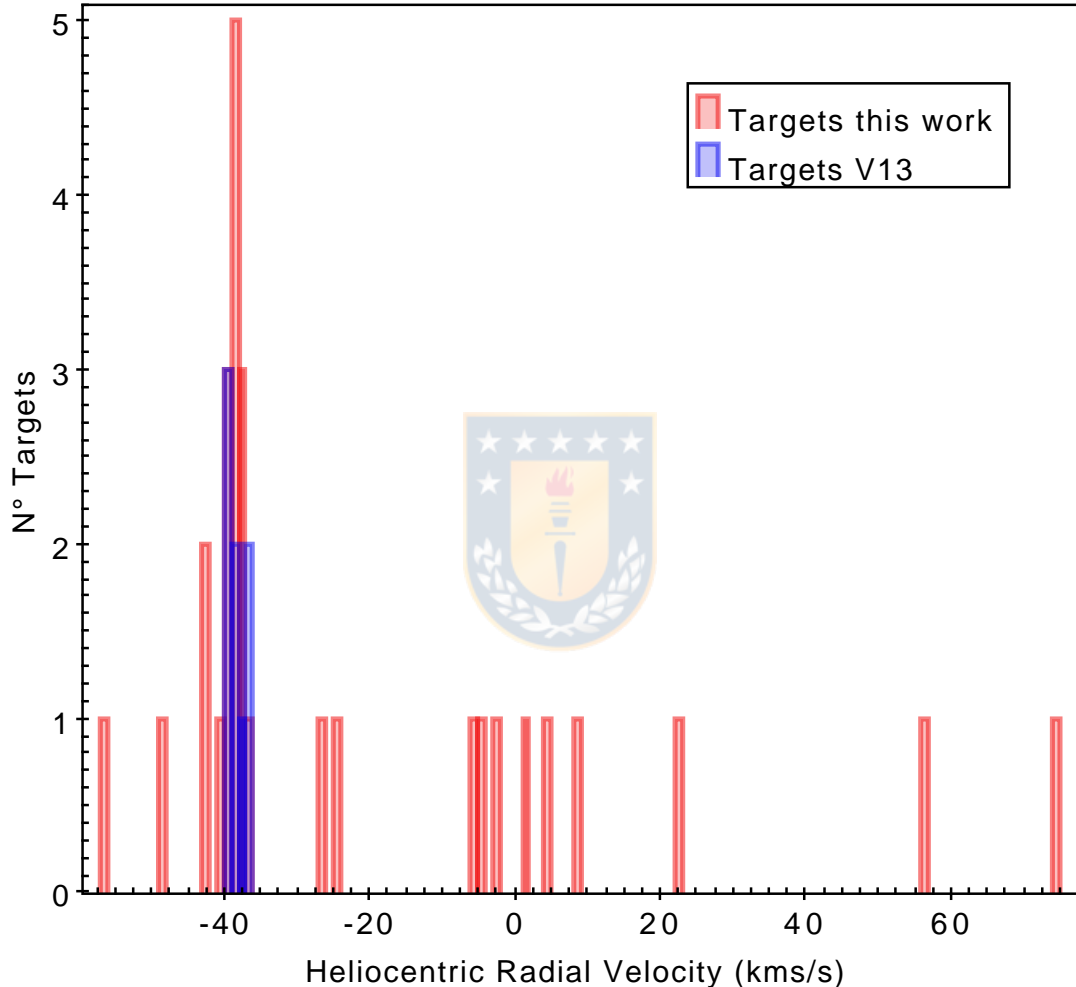
Figure 31: Heliocentric Velocities of the targets of this study are represented in red, targets from V13 have been overlapped in blue. All targets between -45 km s^{-1} and -35 km s^{-1} are considered members of the cluster. Source: Own elaboration.

Thanks to the Proper Motions (PM) provided by the *Gaia* mission DR2(Gaia collaboration et al. 2016,2018), we could remove further non-member stars as shown in Figure 32. We discarded 2 more of our targets that had RV similar to the mean radial velocity of the cluster but very different PM. The average PM of our final targets are : pmRA = -1.21 $\pm$ 0.13 mas yr^{-1} and pmDEC = 0.43 $\pm$ 0.08 mas yr^{-1} [2]. Table 3 (next section, columns 1-8) lists the details of the final members.

---

[2]In agreement with *Gaia* EDR3 (Gaia collaboration et al. 2020).
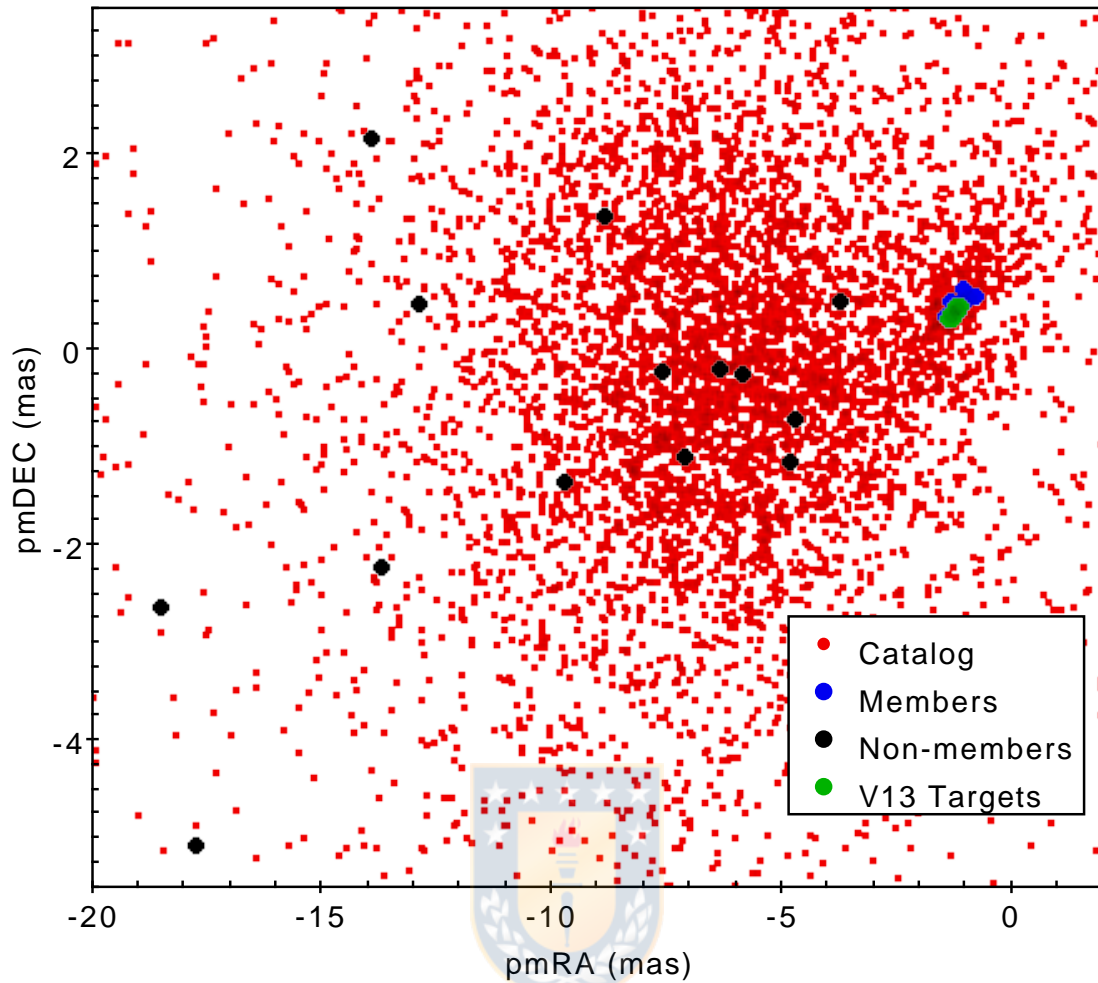
Figure 32: Proper motions for each star of the catalog. Blue dots represent the 13 targets members of the Cluster, black dots represent discarded non-members targets, and green dots represent the targets from V13. Source: Own elaboration.

4.3.2 Atmospheric parameters

Figure 33 shows the V-I vs V CMD with the identified members from this work and V13. All the stars with photometric errors greater than 0.1 were removed.

A reddening correction E(B-V) = 0.20 (Harris 1996, 2010 edition) was applied to the V-I color using the extinction relation E(B-V) = 1.24E(V-I) in order to obtain effective temperatures. Then T_{eff} were determined averaging the values obtained from the expressions given in Ramirez & Melendez (2005) and Alonso et al. (1999). Since Alonso et al. (1999) works with Johnson colors, a relation

$$(V - I)_J = -0.005 + 1.273 \cdot (V - I)_C$$

from Fernie (1983) was applied to our V-I color. Then T_{eff} were plotted against V and a polynomial was adjusted to the RGB, making possible to obtain T_{eff} using the V magnitudes instead of V-I, reducing the uncertainties. These values obtained through the polynomial fit are our definitive T_{eff}. Figure 34 shows a comparison between the T_{eff} obtained through the formulae and the polynomial. T_{eff} from V13 are shown for comparison.
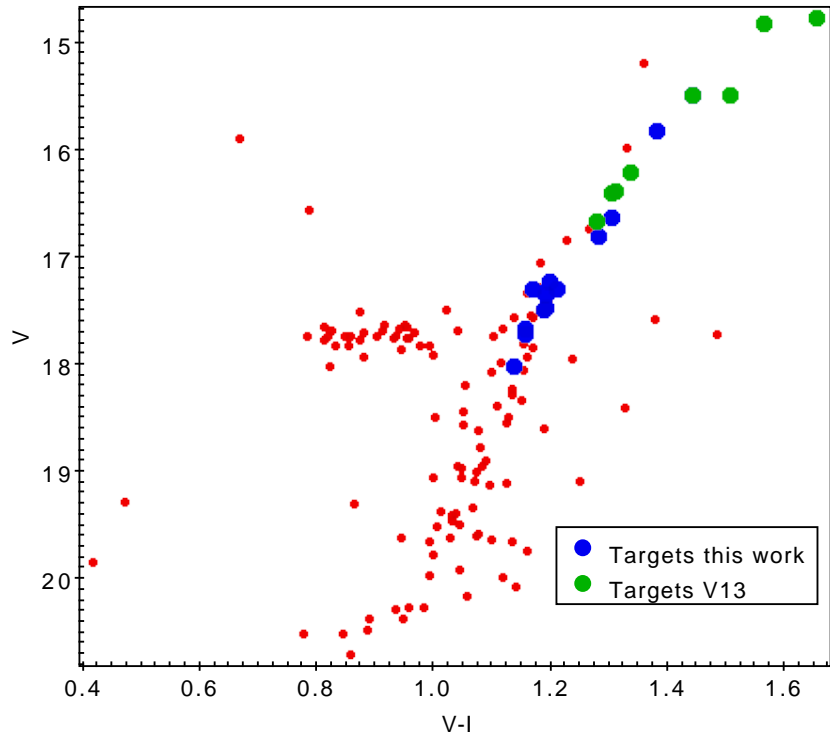
Figure 33: Definitive CMD, targets from this work appear as blue dots while targets from V13 are the green dots. Source: Own elaboration.
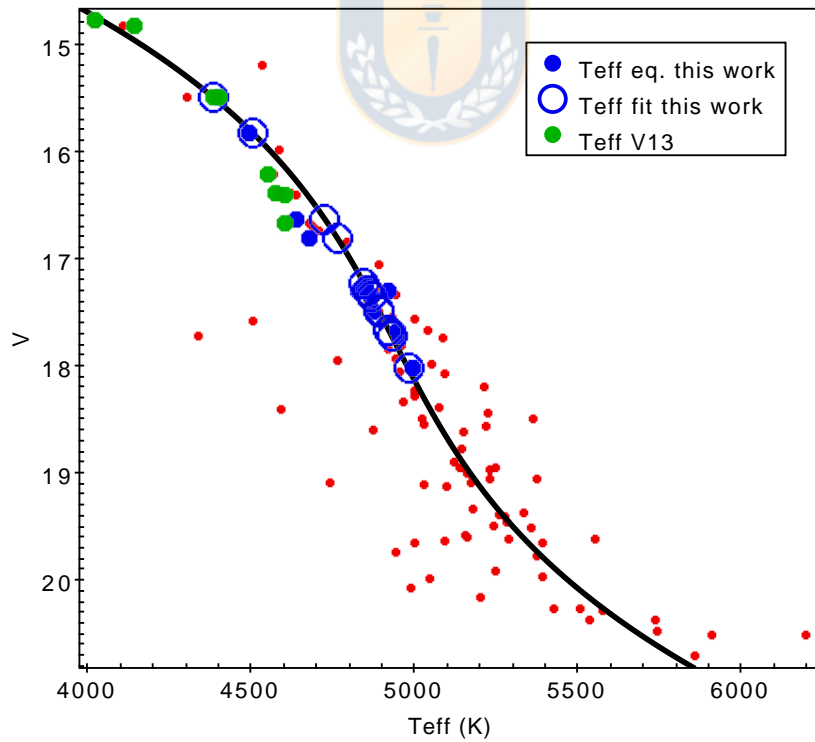
Figure 34: Effective temperatures for each RGB star are shown. Average value from Alonso et al. (1999) and Ramirez & Melendez (2005) appear as red dots. A polynomial fit is shown in black, filled blue dots indicate targets from this work obtained through the mentioned relations while blue circles are the values obtained through the polynomial fit, green dots are the effective temperatures from V13. Source: Own elaboration.

ID	RA(J2000) (h:m:s)	Dec (°:':")	V mag	I mag	pmRA (mas yr⁻¹)	pmDEC (mas yr⁻¹)	RV (km s⁻¹)	T_{eff} (K)	log(g) (dex)	v_t (km s⁻¹)
11012	12:38:33.50	-51:10:58.30	18.022	16.885	-1.47079	0.34399	-39.16	4978	2.3715	1.4564
11579	12:39:05.60	-51:10:26.60	17.303	16.093	-1.24388	0.38164	-37.88	4856	2.0253	1.5678
12911	12:38:42.58	-51:09:23.00	15.494	14.054	-1.37353	0.35648	-39.25	4382	1.0307	1.8881
14650	12:38:57.47	-51:08:11.40	17.231	16.033	-1.07649	0.60763	-40.31	4843	1.9899	1.5792
14861	12:38:23.50	-51:07:58.40	17.484	16.292	-1.4267	0.31629	-38.29	4888	2.1132	1.5396
15108	12:38:25.04	-51:07:43.40	17.502	16.315	-1.26708	0.40051	-42.77	4891	2.1220	1.5367
15225	12:38:39.52	-51:07:37.10	17.673	16.517	-1.3498	0.48873	-39.50	4920	2.2042	1.5103
15502	12:38:38.34	-51:07:20.70	16.807	15.526	-1.18759	0.38536	-37.29	4761	1.7783	1.6474
15985	12:38:45.98	-51:06:49.40	16.631	15.328	-1.12986	0.47452	-38.71	4723	1.6877	1.6766
16174	12:39:02.27	-51:06:34.50	17.725	16.570	-0.94386	0.50756	-38.09	4928	2.2292	1.5022
16394	12:38:50.70	-51:06:18.80	15.822	14.439	-1.09852	0.46612	-38.02	4501	1.2368	1.8218
5015399	12:38:47.27	-51:09:52.90	17.351	16.159	-0.82873	0.54844	-37.87	4865	2.0487	1.5603
5016747	12:38:51.17	-51:08:54.20	17.305	16.137	-1.27574	0.34161	-42.74	4856	2.0264	1.5675

Table 3: Table with the details of the Targets. The order of the columns are: Star ID, Right Ascension(J2000), Declination(J2000) , Magnitude in V, Magnitude in I, Absolute Proper Motion in RA, Absolute Proper Motion in DEC, Heliocentric Radial Velocity, effective temperature, surface gravity and microturbulence velocities. Source: Own elaboration.

Surface gravities log(g) were determined through the canonical equation:

$$log(g/g_\odot) = 4log(T_{eff}/T_\odot) - log(L/L_\odot) + log(M/M_\odot)$$

Assuming a mass of 0.8 $M_\odot$, a luminosity based in the distance modulus $(m-M)_v = 17.25$ (Harris 1996,2010 edition) and a relation obtained from Alonso et al. (1999) for bolometric corrections(BC).Figure 35 shows the log(g) obtained using the T_{eff} from the equation and the polynomial fit, log(g) values from V13 are also shown. There is a difference between our values and V13(obtained through spectroscopy) about 0.4. Finally, microturbulence velocities v_t were determined using the relation from Gratton et al. (1996):

$$v_t = 2.22 - 0.322 \cdot log(g)$$

Figure 36 show the values obtained in the same way as log(g) but for v_t, the V13(spectroscopic) values differ from the photometric in $\sim$0.3.

As mentioned, our definitive values are those obtained from the T_{eff} polynomial fit. Table 3(columns 9-11) gives the values of the atmospheric parameters.

The T_{eff}, log(g) & v_t were used together with the initial metallicity estimate of [Fe/H] = -1.5 (V13) to generate atmospheric models for each target.

Although log(g) & v_t differ between V13 and this study, we decided to continue with our own photometric parameters since Mucciarelli et al. (2020) concluded that the spectroscopic parameters may be in error for metallicity lower than –1.5 dex, leaving our cluster at the limit where the spectroscopic parameters begin to be wrong. Also, to match our parameters with the spectroscopic values from V13 we should shift them, increasing the uncertainties.
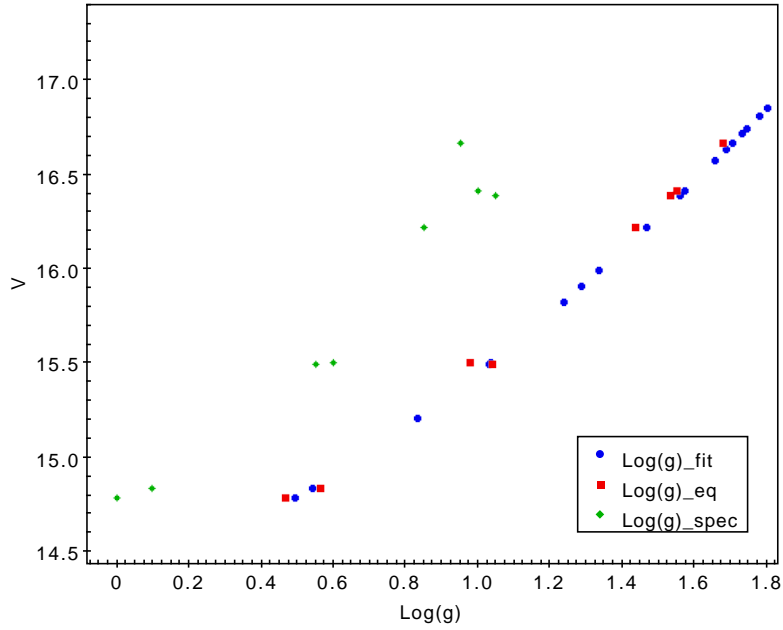
Figure 35: Surface gravities obtained using the adjusted polynomial from T_{eff} are shown as blue circles. Red squares showing the Log(g) using the original T_{eff} are shown too to demonstrate the the difference between both is negligible, and green diamonds are the log(g) from V13 that show a shift of ~ 0.4. Source: Own elaboration.
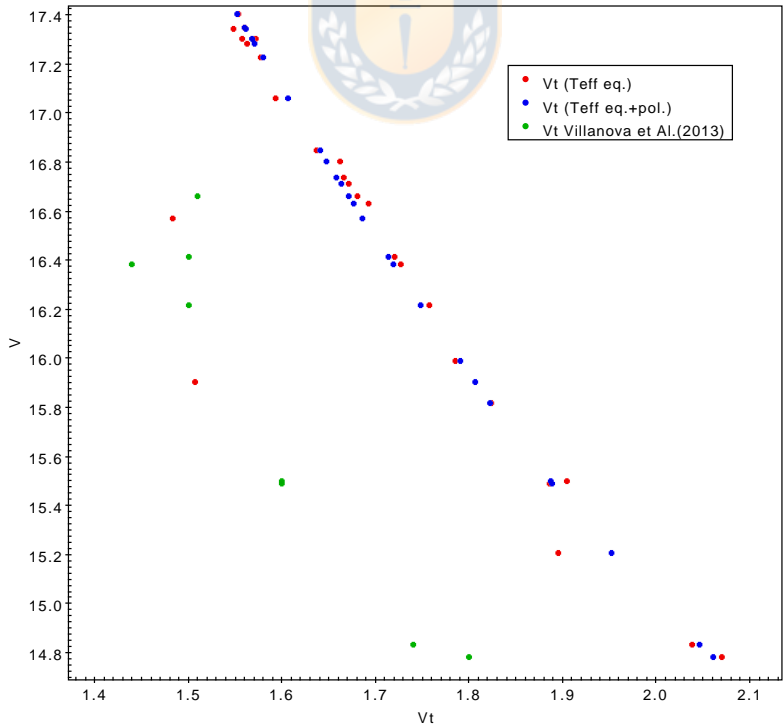
Figure 36: Microturbulence velocities using the formula from Gratton et al. (1996) are shown as blue circles. Again, values not using the polynomial T_{eff} values are shown in red to compare. Green circles are the values from V13. The difference between both photometric and spectroscopic values this time is 0.27. Source: Own elaboration.

37

4.4 Abundance Analysis

Chemical abundances were calculated using the Local Thermodynamic Equilibrium program MOOG (Sneden 1973), and atmospheric models were calculated using the ATLAS9 code (Kurucz 1970), assuming our initial estimations of the atmospheric parameters. The Spectrum-synthesis technique was used to determine Fe and Na abundances. This method consist in comparing an observed spectral line with five different synthetic spectra calculated with different abundances. The interpolated model with the lowest Root Mean Square compared to the observation give us the abundance of the element associated with that line. For a more precise determination we applied a parabolic fit to the 5 RMS values of the 5 synthetic spectra plotted as a function of the abundance in order to obtain the minimum. This minimum is the final abundance we assumed for the line.An example of the spectrum-synthesis applied to the Na line is shown in Figure 37.
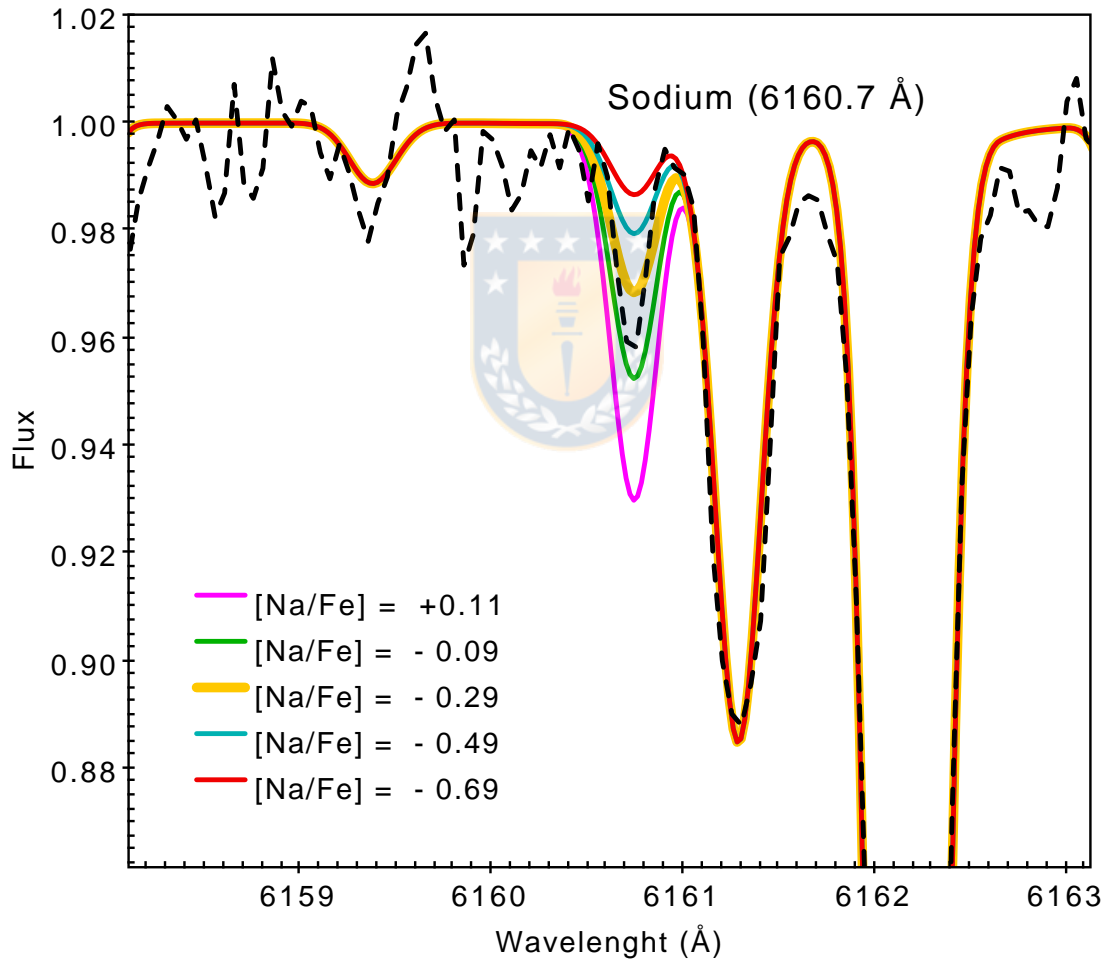
Figure 37: Spectrum-synthesis in the line at 6160.7 Å of the star 12911. Five different synthetic spectra appear as coloured lines. The best fit among the five is shown as a broader yellow line ([Na/Fe]=-0.29). Source: Own elaboration.

We used the following lines for iron: (6136 Å, 6191 Å, 6213 Å, 6252 Å, 6322 Å, 6335 Å, 6336 Å, and 6393 Å), while for Na we used the line at 6160.7 Å since that at 6154.2 Å was too weak. The FWHM to be used for the spectrum-synthesis of

ID	T$_{\text{eff}}$	[Fe/H]	[Na/Fe]
11012	4978	-1.42	<-0.20
11579	4856	-1.44	-0.39
12911	4382	-1.53	-0.29
14650	4843	-1.43	<-0.29
14861	4888	-1.41	<-0.01
15108	4891	-1.47	< 0.05
15225	4920	-1.55	< 0.03
15502	4761	-1.47	-0.31
15985	4723	-1.46	<-0.16
16174	4928	-1.42	-0.37
16394	4501	-1.53	-0.28
5015399	4865	-1.44	-0.44
5016747	4856	-1.46	-0.41

Table 4: Table with abundance values. The order of the columns are: Star ID, effective temperature, metallicity and Na abundance. In some cases we could establish only upper limits for Na abundances. Source: Own elaboration.

the Na line was determined by the comparison of the synthetic spectra with nearby strong and well defined Ca and Fe lines.

For some targets we could estimate only upper limits, mostly due to the low S/N ratios. The adopted solar abundances were $\log\epsilon$(Fe)=7.50 and $\log\epsilon$(Na)=6.32 (V13). Our mean abundances for each star are represented in table 4.

Na is known to be affected by departure from LTE. In this paper we did not apply any NLTE correction since our analysis is based on the relative Na abundance of stars that have roughly the same atmospheric parameters and so the same NLTE corrections for sodium. In any case, according to the INSPECT database [3], the Na NLTE correction for our abundances is of the order of -0.20 dex for all our targets.

Figure 38 report the present results together with those of V13. In the upper panel we report the [Fe/H] abundance as a function of the temperature. We can see that there is no trend in spite that the two sets of abundances were obtained using different spectrographs and methods. Also the linear fit is compatible with a flat trend within 1 σ. Combining the two databases we obtained a mean iron abundance of

$$[Fe/H] = -1.47 \pm 0.01$$

and

$$\sigma_{[Fe/H]} = 0.05 \pm 0.01$$

In the lower panels we report the [Na/Fe]$_{\text{LTE}}$ abundances as a function of the temperature (left panel) and the [Na/Fe]$_{\text{LTE}}$ distribution (right pannel). In this case GIRAFFE data have a systematic shift of +0.11 dex (targets with upper limits were not considered for the comparison). The cause of this systematics is probably due to the fact that in V13 we used the four Na lines at 5682.6 Å, 5688.2 Å, 6154.2 Å and 6160.7 Å as Na abundance indicator while here we could use only that

---
[3]http://www.inspect-stars.com/

at 6160.7 Å. Also systematics due to some effect related to the spectrograph not well removed during the reduction procedure cannot be ruled out such as scattered light. We applied a correction of -0.11 dex to the Na abundances obtained from GIRAFFE data. Making this correction to only our stars with derived values and then combining the samples, we found a mean Na LTE abundance of:

$$[Na/Fe] = -0.47 \pm 0.01$$

The Na distribution histogram is very narrow with a r.m.s. of:

$$\sigma_{[Na/Fe]} = 0.06 \pm 0.01$$

The typical internal error on the fit for our T_{eff} is 10-20 K, while the errors on $\log(g)$ and v_t are below 0.1 dex and 0.05 km/s respectively. If we apply the same procedure described in V13 for the error calculation we obtain:

$$\sigma_{TOT}(Na) = 0.05$$

We underline the fact that in our case the observational error is dominated by the S/N of the spectra. Comparing this value with the r.m.s. of the Na distribution histogram we can confirm the result by V13 that Rup106 does not host multiple stellar populations.
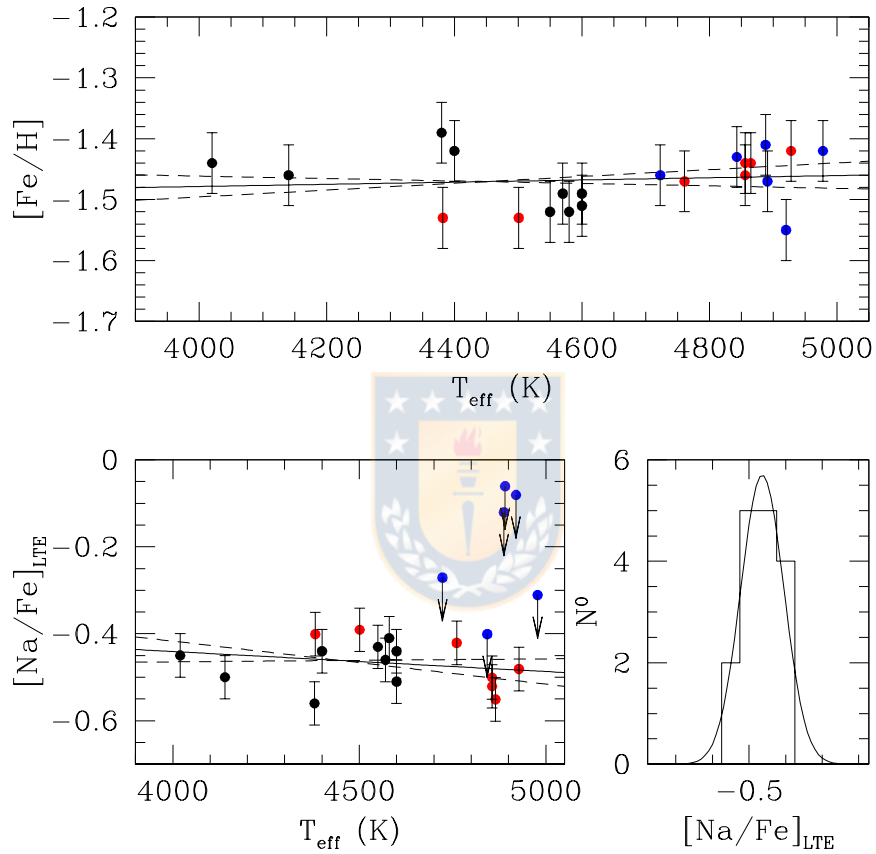
Figure 38: Upper panel: [Fe/H] abundance as a function of the temperature, Red dots are determined abundances, blue dots are upper limits and black dots are abundances from V13. Lower panel(Left): [Na/Fe]$_{LTE}$ abundances as a function of the temperature. Lower panel(Right): [Na/Fe]$_{LTE}$ distribution. Source: Own elaboration.

4.5 Photometric Analysis

As mentioned, the Washington filter C has proved to be useful to detect MPs due to the fact that it covers CN, CH and NH bands (Canterna 1976). Figure 39 shows a CMD obtained using the Washington Filter C combined with the R_{KC} filter, limited to the part of the RGB where our targets lie. If Rup106 had more than one stellar population we should observe one of the following effects:

a) A split in the RGB (Cummings et al. 2014). In this case all the targets would lie in one or the other of the RGBs.

b) A spread in the RGB caused by the chemical differences between the populations and larger than the photometric errors.

Figure 39 shows instead that the RGB of Rup106 is very narrow and that the spread in color is compatible with the errors.
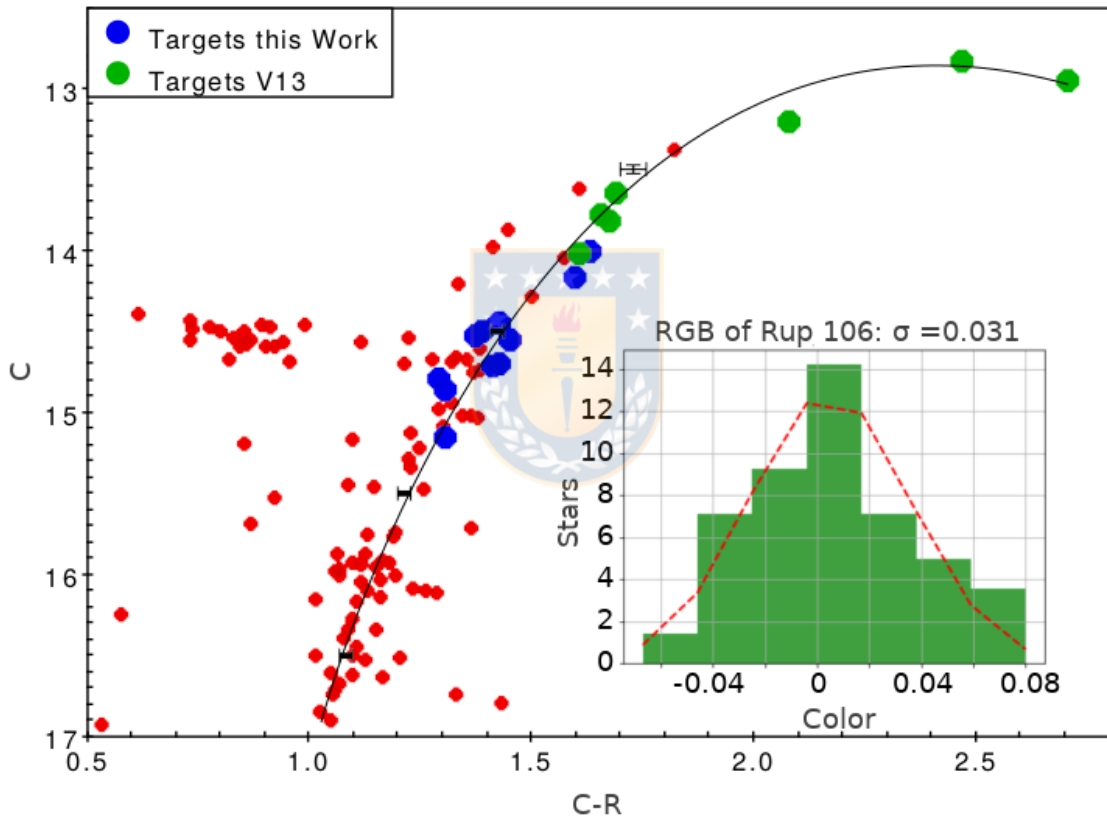
Figure 39: CMD using the Washington filter C to distinguish the presence of MPs. The spread of the Targets along the RGB indicate the presence of only one population. A fiducial has been adjusted, color differences of stars from the fiducial have been normalized in a histogram and the best-fitting gaussian has been derived. Source: Own elaboration.

A fiducial curve (defined as the highest density locus of stars along the RGB) has been fitted along the RGB in C-R vs C (the black curve in Figure 34). We then measured the color difference of the stars from the fiducial and build a distribution histogram of this value. We then derived the best-fitting gaussian for the histogram and got $\sigma = 0.031 \pm 0.003$, about 1.5 times the median error in the C-R color for the RGB that is $\sigma_{\text{C-R}} = 0.02 \pm 0.01$ obtained calculating the square root of the sum

of the squares of the errors of each filter. The σ value we found is very likely an upper limit and not the intrinsic width of the RGB since the field contamination cannot be fully removed because of the superposition of the cluster with the field in the proper motion space (see Figure 27). For this reason we conclude that the width of the Rup106 RGB is fully explained by the photometric errors and it does not require the presence of multiple stellar populations.

4.6 The Orbit

We used the GRAVPOT16[4] model (Fernández-Trincado et al. in preparation) to study the orbital elements (eccentricity, apo-/peri-galactocentric distance, the characteristic orbital energy, and the orbital Jacobi constant) of Rup106. Since V13 already suggest that this cluster has an extragalactic origin based on its Na and α-element abundances, the aim is to find the Halo structure Rup106 is associated with.

The GRAVPOT16 is composed of a massive ($\sim$1.1$\times$10^{10} M$_\odot$) 'boxy/peanut' bar/bulge structure accompanied by multiple stellar discs whose profiles mimic to that of the Besançon Galaxy model (Robin et al. 2003, Robin et al. 2014). For the orbit computations, we adopt the same model configuration and Sun's positions and velocity as in Fernandez et al. (2020), except for the bar patterns speed, which we adopt the recommended value of 41 km s^{-1} kpc^{-1} (see e.g., Sanders et al. (2019)). We integrated hundred thousand orbits by adopting a simple Monte Carlo approach which considers the errors in the observables as 1-σ variations over a 5 Gyr timespan toward the past (backward) and future (forward) by adopting the observables with their respective errors from Baumgardt et al. (2019):

$$\text{RA: } 189.6675°$$
$$\text{DEC: } -51.150277°$$
$$d = 21.2 \pm 2.12 \text{ kpc}$$
$$\text{RV}_{\text{Helio}}: -38.36 \pm 0.26 \text{ km s}^{-1}$$
$$\text{pm}_{\text{RA}}: -1.25 \pm 0.01 \text{ mas yr}^{-1}$$
$$\text{pm}_{\text{DEC}}: 0.39 \pm 0.01 \text{ mas yr}^{-1}$$

Figure 40 show the resulting orbits of Rup106 on the equatorial and meridional Galactic planes in the inertial frame. The top and bottom panel in Figure 40(a) show the predicted orbit of Rup106 without considering the errors in the observable, while the the top and bottom panel Figure 40(b) show the resulting ensemble of orbits from our Monte Carlo approach, which consider the errors in the observable. The yellow and orange colors correspond to more probable regions of the space, which are crossed more frequently by the simulated orbits, while the black solid and dashed line show the forward and backward orbital path of Rup106 over 1 Gyr for guidance.

Figures 40a and 40b reveals that Rup106 lies on a radial and highly eccentric (>0.81 $\pm$ 0.01) halo-like orbit with rather higher excursions above the Galactic plane ($\sim$23.6 $\pm$ 3.2 kpc). The perigalactocentric (r$_{\text{min}}$) and apogalactocentric (r$_{\text{max}}$) distance of Rup106 is $\sim$3.4 $\pm$ 0.5 kpc and $\sim$32.7 $\pm$ 3.7 kpc, respectively, placing the cluster well within the inner halo of the Milky Way, but located beyond of the bulge/bar region. In addition, using a slightly different angular velocity for the bar ($\pm$10 km s^{-1} kpc^{-1}) does not change significantly our conclusions, and returns orbits in which the cluster is confined to the inner halo.

It is important to note that unlike Baumgardt et al. (2019), our orbit computations are based in a realistic (as far as possible) barred Milky Way model, which may affect the orbital path of Rup106, as the cluster orbit has close approaches ($\sim$3 kpc) to the 'bulge/bar' region, where the strength of the 'bar' structure is important.

Figure 40c show the Characteristic orbital energy (E$_{\text{char}}$ = (E$_{\text{max}}$ + E$_{\text{min}}$)/2) versus the orbital Jacobi constant (E$_{\text{J}}$) in the non-inertial reference frame where

---

[4]https://gravpot.utinam.cnrs.fr/
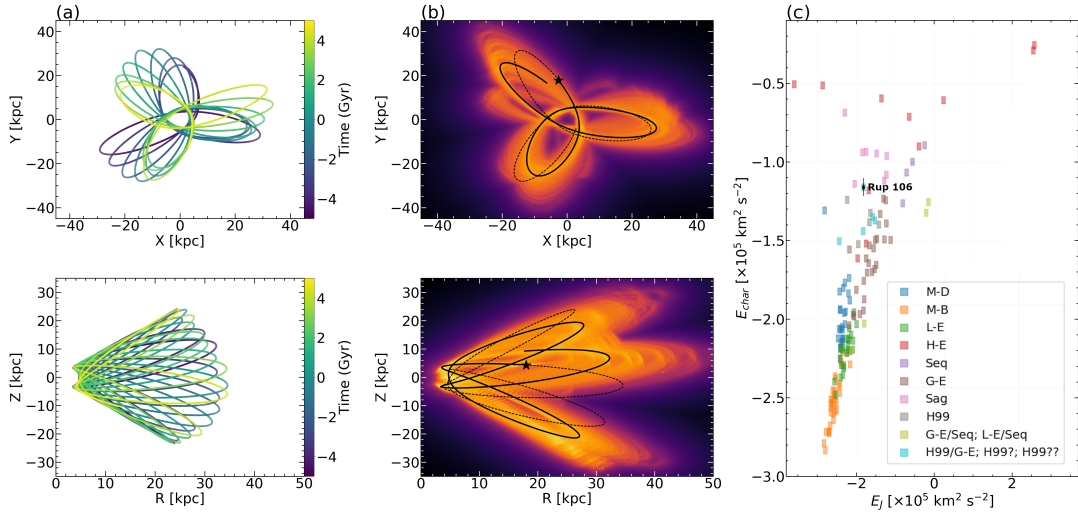
Figure 40: Panels (a) and (b) shows the equatorial and meridional Galactic planes in the inertial frame, time-integrated forward/backward over 5 Gyr. Panel (b) show the probability density, with yellow and orange colors corresponding to more probable regions of the space, which are crossed more frequently by the simulated orbits. The black solid and dashed line show the forward and backward orbital path of Rup106 over 1 Gyr, for guidance. Panel (c) show the Characteristic orbital energy ((E_{max} + E_{min})/2) versus the orbital Jacobi constant (E_J) in the non-inertial reference frame where the bar is at rest. Other Galactic GCs associated with different progenitors from Massari et al. (2019) are shown for comparison. The black dot with error bars refers to Rup106 analyzed in this work. Source: Own elaboration.

the bar is at rest, as defined in Moreno et al. (2015) and Fernandez et al. (2020). This plane reveals that the orbit of Rup106 lies in the boundary between three groups of GCs, e.g., those in the High-Energy group (H-E), the group dominated by Helmi-Stream (H99), and the group associated with the Sagittarius dwarf galaxy (Sgr) (see e.g., Massari et al. (2019)). For this reason, based only in the dynamical configuration of Rup106 there is not a clear association with any of the proposed progenitors in the Milky Way.

V13 concluded that the very low Na and α-element abundances of Rup106 only match those of the Magellanic Clouds and of the Sagittarius Galaxy. Combining our results with these conclusions we could determine that the progenitor of Rup106 is the Sagittarius dwarf galaxy, adding evidence that does not contradict the results from
Bellazzini et al. (2003) and are in line with those from Sbordone et al. (2005), however it still contradicts the conclusion of Law & Majewski (2010) who did not find significant evidence for association with any wrap of the Sgr arms, leaving the discussion opened again.

In spite of the fact that the progenitor of Rup106 is not clear, Massari et al. (2019) and Bajkova & Bobylev (2020) define it as a potential Helmi-Stream (H99) member. It is worth mentioning that all the other members of this group possess MPs with the exception of E3 (although only classified as H99 by Massari et al. (2019)). This cluster was studied in Salinas et al. (2015) and Monaco et al. (2018)

analysing 23 RGB members with low resolution spectroscopy and 4 RGB stars with high resolution spectroscopy, respectively. Both studies conclude that there is no evidence of MPs in such cluster.

In addition, Bastian & Lardo (2018) named other 3 SSP GCs: Terzan 7, Pal 12 and Pal 3. The first two GCs are Sgr members and the last belongs to the H-E group. This would indicate that all the SSP and potential SSP GCs have an extra galactic origin.

5 Part II: C, T_1, T_2. A complementary method to uncover Multiple Populations

5.1 Introduction

Multiple Populations (MPs) are now recognized as an essential characteristic of almost all Globular Clusters (GCs). Historically, Cannon & Stobie (1973) almost 50 years ago found an exceptionally large scatter in the Red Giant Branch(RGB) of Omega Cen. Thirty years later Bedin et al.(2004) found two primary sequences not only in the color of the RGB of Omega Cen, but also in the Sub Giant Branch (SGB) and Main Sequence(MS), giving the first detailed photometric glimpse of what would become known as MPs.

But it was not until Carretta et al.(2009) realized a heroic high resolution spectroscopic study of thousands of stars in a total of 19 GCs, finding chemical inhomogeneities in all of them, that MPs began to be considered as an intrinsic characteristic of GCs. Subsequently, Carretta et al.(2010) in fact suggested a new defintion of a GC: Stellar systems showing anti-correlations among the abundances of light-elements, whose main and most widespread example is the Na-O anticorrelation. This major study would be complemented 6 years later with that of Piotto et al.(2015), who conducted the HST GC UV Legacy survey using an improved photometric method employing the UV/blue WFC3/UVIS filters F275W, F336W, and F438W , best known as the "magic trio", to characterize MPs in 57 GCs, showing that they all possess MPs and proving photometry with appropriate filters as an excellent method to detect MPs. The advantages of photometry over spectroscopy of course are the ability to investigate MPs in a much larger sample in a given GC with a much smaller telescope than typically possible with high resolution spectra. Two years later, Milone et al.(2017) divided these 57 GCs into type I(GCs whose stars separate in two distinct groups, identified as first(1G) and second(2G) generations) and type II clusters (those GCs where the 1G and/or the 2G sequences appear to be split and include an additional group of redder stars in the chromosome map. Type II GCs also exhibit multiple SGBs in purely optical CMDs).

The most important conclusion is that virtually all the GC show MPs. But some clusters seem to be the exception, IC4499 (Walker et al. 2011) and especially Ruprecht 106 (Villanova et al. 2013, Frelijj et al. 2021) are the best examples. Thus, every cluster has to be carefully studied to determine whether it has MPs or not, and study its characteristics, as the UV Legacy survey has demonstrated that every GC is unique in its MP behavior.

Various scenarios for the origin of MPs have been proposed: Asymptotic Giant Branch scenarios like D'ercole et al.(2008), Fast Rotating Massive Stars scenarios like Decressin et al.(2007) and even a scenario that did not invoke multiple epochs of star-formation Bastian et al.(2013). But currently none of them satisfies all the observational evidence (Renzini et al. 2015, Bastian & Lardo 2018).

The previous studies mentioned above have proven photometry to be a very good way to search for MPs, because, while it cannot provide the detailed abundances of spectroscopy, it allows the measurement of a much larger sample of stars simultaneously and to much fainter absolute magnitudes. Sbordone et al.(2011) produced synthetic spectra of two otherwise identical GC giants, one being a 1G star with normal chemical abundances of the light elements and the other is a 2G star with

enhanced He, N and Na and depleted C and O, as observed in many spectroscopic studies. The study shows that significant differences in flux between the two spectra exist and are related to the various CN, CH, NH and OH bands, particularly in the UB/blue part of the spectrum.

Some photometric bands, concentrated in the blue-uv portion of the spectrum, are specially sensitive to these bands. The best known are the already mentioned "magic trio" of filters used in Piotto et al.(2015), consisting of three HST UVIS/WFC3 filters: F275W, F336W and F438W. The combination of these sensitive filters led to colors maximizing the separation of the different populations of stars. Actually, most blue/UV filters are capable of uncovering MPs. However, although most such filters, such as $U_{Johnson-Cousins}$ and u'_{SDSS}, detect MPs quite well, they require long exposure times due to their relatively narrow band and/or low efficiency.

The Washington filter system was designed by Canterna (1976) originally to derive a photometric temperature (from the T_1 and T_2 filters, very similar to $(RI)_{KC}$), as well as a metallicity index (from the M filter) for G and K giants. However, at the time, CN and CH variations were being discovered in GCs and it was felt prudent to include another filter that would be sensitive to such variations independent from metallicity effects, and thus the C ("Carbon") filter was added. The Washington C filter is a blue-UV filter, with λ_{eff} =3982Å and $\Delta\lambda$ =1070Å (Bessel 2005). This broadband allows it to encompass 3 CN-Bands and one NH-Band, as well as the CH band. Because of its efficiency, it should be sensitive to MPs in considerably less exposure time than other, more narrow-band, filters. These 2 characteristics make the Washington C filter a good option for detection of MPs. Indeed, the HST WFC3/UVIS instrument includes a C-like filter: F390W.

Initial efforts investigating the possibility of uncovering MPs from the ground with the Washington system used the $C - T_1$ color, obtaining good results (Cummings et al. 2014, Frelijj et al. 2017). These results, although not as accurate as HST data, present an attractive alternative, based on small ground-based telescopes. Our aim here is to investigate if there might be an even better Washington color for detecting MPs, involving the addition of the T_2 filter, which maintains some MP sensitivity (see Figure 42).

This Section is organized as follows:
In subsection 5.2 we present the data used, how it was obtained and reduced. Subsection 5.3 describes the results using the new method and compares these with results from the initial technique. We also analyze the results.

5.2 Data

5.2.1 Observations

The data consist of 46 images, 23 of NGC 7099 and 23 of NGC 1851. They were obtained from 2 telescopes, the 1-meter Swope telescope from Las Campanas Observatory, Chile; and the 4m SOAR telescope on Cerro Pachon, Chile. The filters selected for this work were the Washington C filter (Canterna 1976), and the filters R_{KC} and I_{KC} in replacement of the Washington filters T_1 and T_2 since Geisler (1996) demonstrated that the R_{KC} filter is a more efficient substitute for T_1 and the T_2 filter is almost identical to I_{KC} (Canterna 1976, Geisler 1996).

For NGC 7099 we used the same images from Frelijj et al.(2017)(hereafter F17), only dropping 1 medium and 2 long C exposures from the Swope Telescope in order to decrease the average seeing. The airmasses vary between 1.0-1.4 while the FWHM is 0.9"-1.7" for the Swope images and 0.39"-0.54" for SOAR images.

For NGC 1851 we took the images used in Cummings et al.(2014)(hereafter C14) but discarded 3 long, poor-seeing C exposures from the Swope telescope, added 1 short exposure from Swope for C,R & I, and added 2 short and 2 long exposures from SOAR in C. The airmasses vary between 1.0-1.5 while the FWHM is 0.9"-1.58" for the Swope images and 0.49"-0.52" for the SOAR images. All nights appeared photometric visually.

Table 5 gives the details of the exposures.

Table 5:

		NGC 7099			
		Swope		SOAR	
C	1(30s)	2(300s)	4(1200s)	4(10s)	2(300s)
R	1(10s)	1(100s)	3(400s)	-	-
I	1(10s)	1(300s)	3(1200s)	-	-
		NGC1851			
		Swope		SOAR	
C	1(30s)	1(300s)	7(1200s)	2(10s)	2(300s)
R	1(10s)	1(100s)	3(400s)	-	-
I	1(10s)	1(300s)	3(1200s)	-	-

The Swope images were observed with a CCD (SiTe3) of 2048x3150 pixels at 0.435 "/pix and a field of view of 14.9 x 22.8 arc minutes. The SOAR detector (SOI) consists of a total of 4096 x 4096 pixels at 0.1534"/pix (0.0767 "/pix binned 2x2) and a field of view of 5.26 x 5.26 arc minutes, divided into two CCDs with two amplifiers each resulting in 4 columns of 1024x4096 pixels.

5.2.2 Processing and Reduction

IRAF [5] and its standard tasks were used to process all the photometric data. A linearity correction (Hamuy et al. 2006) was applied to all the Swope (SiTe3) images in order to increase the range of unsaturated stars. DAOPHOT (Stetson 1987)

---

[5] IRAF is distributed by the National Optical Astronomy Observatory, which is operated by the Association of Universities for Research in Astronomy (AURA) under a cooperative agreement with the National Science Foundation.

ID	RA(J2000)	DEC(J2000)	X	Y	Rad	C	eC	dC	mC	nC
324	78.684240068	-40.042003974	161.219	1827.654	999.03	20.3654	0.0082	0.0033	0.0082	3
334	78.683674458	-40.043001613	164.868	1835.867	995.23	20.7216	0.0101	0.0016	0.0101	3
347	78.683039621	-40.047603550	169.203	1873.867	991.08	20.8262	0.0113	0.0010	0.0113	3

Table 6: The columns are: ID, RA and DEC coordinates (in degrees), X and Y coordinates (in px), radial distance of the star to the centre (in px), magnitude, psf-fitting error (internal error), dispersion (external error), higher value between internal and external error, and the number of frames where the star was detected. (All of this for C, T_1 and T_2 but due to the lack of space this table shows only C)

and its suite of tasks were used to perform the photometry in both clusters since it was specially developed to work on crowded fields. A first PSF was determined in each single image by taking the ∼200 brightest unsaturated and more isolated stars. These stars were refined subtracting all their detected neighbours to determine a second and more precise PSF that was refined a third time by eye, thus removing all PSF-stars with bad subtracted neighbours. This refined PSF determined in each image was applied to carry out a PSF photometry three successive times through the tasks FIND, PHOT and ALLSTAR. Due to the large pixel scale of the SiTe3 detector (0.435 "/pix), we decided to repeat the technique used in C14, setting in DAOPHOT and ALLFRAME a fitting radius 0.4px smaller than the FWHM measured, for all the Swope images with a FWHM smaller than 3 px in order to avoid photometric errors due to "square stars". We experimented with different ALL-FRAME (Stetson 1994) methods based on the procedures from C14 and F17, and found that the best photometry is obtained in the following way:
-First, applying the cuts used in C14, that consists in removing all the stars with errors higher than 0.15, chi-squared greater than 2.5, absolute sharpness value greater than 1 (1.5 for C filter) and magnitudes above the point (determined for each image by looking in the plot magnitude vs error) where the stars begin to be affected by the nonlinearity of the detector.
-Second, using DAOMATCH and DAOMASTER to match all the images to create a single starlist that will be given to ALLFRAME to perform PSF-Photometry in all the images simultaneously.
-Third, using DAOMATCH and DAOMASTER to match the catalogs given by ALL-FRAME, first combining the images with the same time exposure and filter, and then all the resulting catalogs of each filter to get a robust intensity-weighted mean instrumental magnitude, using the medium exposure as a reference image since it maximizes the number of stars in common with both short and long exposures, facilitating the match.
-Finally, use DAOMATCH and DAOMASTER again to generate a full catalog with all the stars found in at least 2 of the 3 filters. The R filter was used as reference filter since its wavelength response lies between the C and I filters and because it produces the deepest images.

Aperture corrections were determined taking the brightest and unsaturated stars from the entire field comparing their PSF photometry to their aperture photometry. No spatial dependence was found in any filter for both clusters.

The instrumental magnitudes of NGC 7099 were transformed to the standard Washington system using the standard coefficients obtained in F17. The RMS for each filter is 0.038(C), 0.022(R) and 0.027(I). However, for NGC 1851, the standard

coefficients from C14 caused an offset of ~ 0.15 to the red in the RGB with respect to the CMD from C14, probably due to the addition of the new images, so we decided to calibrate calculating the difference between our instrumental magnitudes and the standard magnitudes of the CMD from C14 for each star using the following formulae:

$$C = (c - r) * m_1 + n_1 + c$$
$$T1 = (c - r) * m_2 + n_2 + r$$
$$T2 = (r - i) * m_3 + n_3 + i$$

where C, T1 and T2 are our calibrated magnitudes, m is the slope, n is the y-intercept of the line and c, r and i our instrumental magnitudes. The resulting calibrated magnitudes are very similar to those from C14.

According to Bonatto et al.(2013) NGC 1851 has a mean differential reddening of $\langle \delta E(B - V) \rangle = 0.025 \pm 0.01$ while NGC 7099 has a mean differential reddening of $\langle \delta E(B - V) \rangle = 0.03 \pm 0.01$. Taking into account the relation from Geisler et al.(1991) E(C-T1) = 1.966(B-V) we obtain a reddening of E(C-T1)=0.049 for NGC 1851 and 0.059 for NGC 7099[6]. We consider these numbers small enough to be negligible, so reddening corrections are not needed. In particular, in this work we are only interested in differential effects between possible different MPs and not absolute effects.

Finally, a World Coordinate System (WCS) was calculated in both NGC 1851 and NGC 7099 catalogues using 12 stars well distributed along the field to transform the x/y coordinates to RA/Dec(J2000) using the xy2sky task from WCSTools.

5.2.3 Final sample selection

As mentioned in previous works, DAOMASTER gives two types of errors: the combined photometric measurement error output by ALLFRAME(internal error) and the σ based directly on the observational scatter across multiple images(external error). We already proved in F17 through an ADDSTAR experiment that the external errors are better estimates of the real photometric error than internal errors, but for each star we take the largest of these two errors to avoid the fact that some stars detected in one single frame have error "0". These final errors appear in table 6 as mC (We use C as an example for T_1 and T_2 too). We removed all the stars with errors greater than 0.1 in each filter, and colors were created from the remaining stars. The errors in colors are the square root of the quadratic sum of the final errors from each input magnitude. Radial cuts were applied to both clusters following the previous studies from C14 and F17. For NGC 7099 we removed all the stars from the center up to 80px(34.8") radius while for NGC 1851 we cut up to 50px(21.75") due to crowding and we left for both clusters a ring with an outer radius of 1000px(7.25').

Proper Motions (PM) provided by the *Gaia* DR2 mission (Gaia collaboration et al.(2016,2018)) allowed to select (in a PM-RA vs PM-DEC plot) all the stars with PM similar to our cluster reproducing by hand the selection shown in the Baumgardt Globular Cluster database (3rd version) [7], removing non-member stars and cleaning the CMD. From now we work with two kinds of catalog in each cluster,

---

[6]Bonatto et al.(2013) say that differential reddening values lower than 0.04 may be related to zero-point variations.

[7]https://people.smp.uq.edu.au/HolgerBaumgardt/globular/

one catalog containing only member stars to ease the detection of different sequences or broadening in the clusters(Figures 41_{Top}), and a second catalog containing the same member stars plus all the stars that do not have a PM, aiming to have a deeper Main Sequence (Figures 41_{Bottom}).

Figure 41: Definitive CMDs in C-T1 vs C. Top left: NGC 1851 using only member stars according to PMs provided by GAIA. Bottom left: NGC 1851 using member stars according to PMs provided by GAIA plus stars without PMs detected. Top right: NGC 7099 using only member stars according to PMs provided by GAIA. Bottom right: NGC 7099 using member stars according to PMs provided by GAIA plus stars without PMs detected. Source: Own elaboration.

Both catalogs show improvements with respect to their original papers: NGC 1851 is $\sim$1.5 mag deeper in C, and we can see better the double Sub-Giant Branch (SGB) mentioned in C14 and Han et al.(2009), and that Milone et al.(2017) classified as a characteristic of type II GCs. For NGC 7099, since we discarded some bad seeing images, we have a CMD $\sim$1 mag deeper in C and T_2 and a narrower SGB.

5.3 The efficacy of the new color in detecting MPs

As mentioned before, C14 and F17 proved the efficacy and efficiency of the Washington C filter to uncover MPs. This filter goes from the atmospheric cutoff at around 3300 Å to beyond the G-band, thus covering 3 CN-bands, a NH-band and a CH-band. This can be seen in Figure 42, that shows the comparison between the synthetic spectra of otherwise identical 1G and 2G stars made by Sbordone et al.(2011) with the Washington filter response curves included.
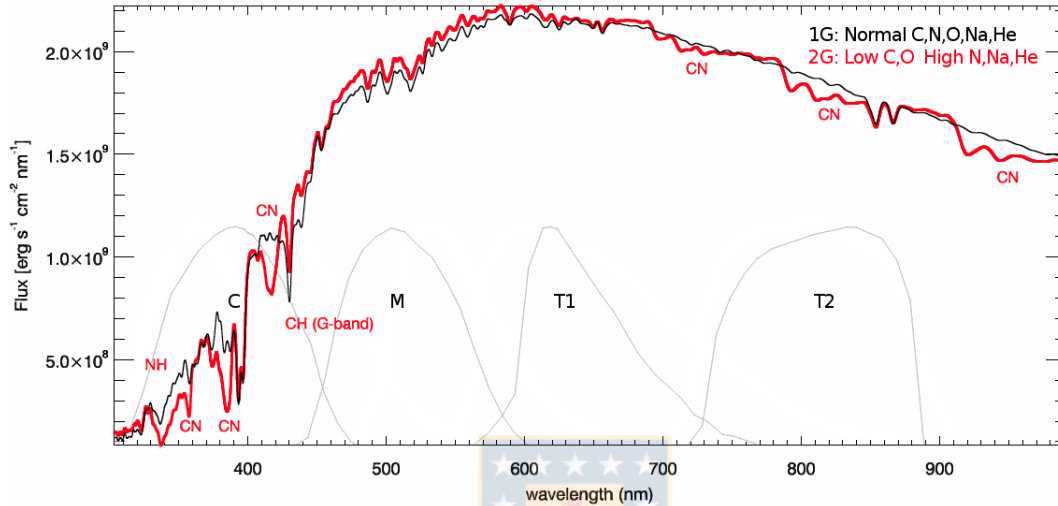

Figure 42: Comparison of the synthetic spectra from 1G(black) and 2G(red) stars. Illustrative Washington filter response curves are included. Source: Own elaboration.

Until now, our best weapon in the Washington System to find MPs was to use the $C - T_1$ color and plot vs C in a CMD, leaving other C filter combinations to show partially defined MPs ($C - T_2$), or how the absence of the C filter fails to separate MPs ($T_1 - T_2$). But careful analysis of Figure 42 shows that the T_2 filter is roughly centered on multiple CN bands which have a fairly significant flux difference between 1G and 2G stars, allowing (in theory) to further separate the populations of the cluster, although our previous studies demonstrated that the spread in $T_1 - T_2$ is almost completely due to the errors. Our hypothesis is that T_2 retains some capability to to distinguish MPs due to the CN-bands that it includes (as seen in figure 42), but the separation of the different sequences is difficult to detect. So based on the technique from Piotto et al.(2015), we created a new combination of colors: $(C - T_1) - (T_1 - T_2)$ (or $C + T_2 - 2T_1$). The idea is that we can potentially further separate the sequences in a CMD combining the potential of $C - T1$ with a small additional difference generated in $T_1 - T_2$. We also note that the C filter includes both CN bands as well as the CH band. The former are stronger in 2G vs. 1G stars due to the fact that the CN-band strength is controlled by the N abundance, which is enhanced in 2G over 1G stars. However, the CH band is weaker in 2G vs. 1G stars since C is depleted. Hence, these 2 effects work against each other to some extent, although it is also clear that the strongest effect is due to the various CN bands, so that the flux in the C filter will be less in a 2G star compared to that of an otherwise identical 1G star. Similarly, it should also be less in the T2 filter for a 2G vs 1G star. Figure 43 shows the new $(C - T_1) - (T_1 - T_2)$(hereafter C, T_1, T_2) vs C CMDs. A detailed analysis is shown in the next subsections.
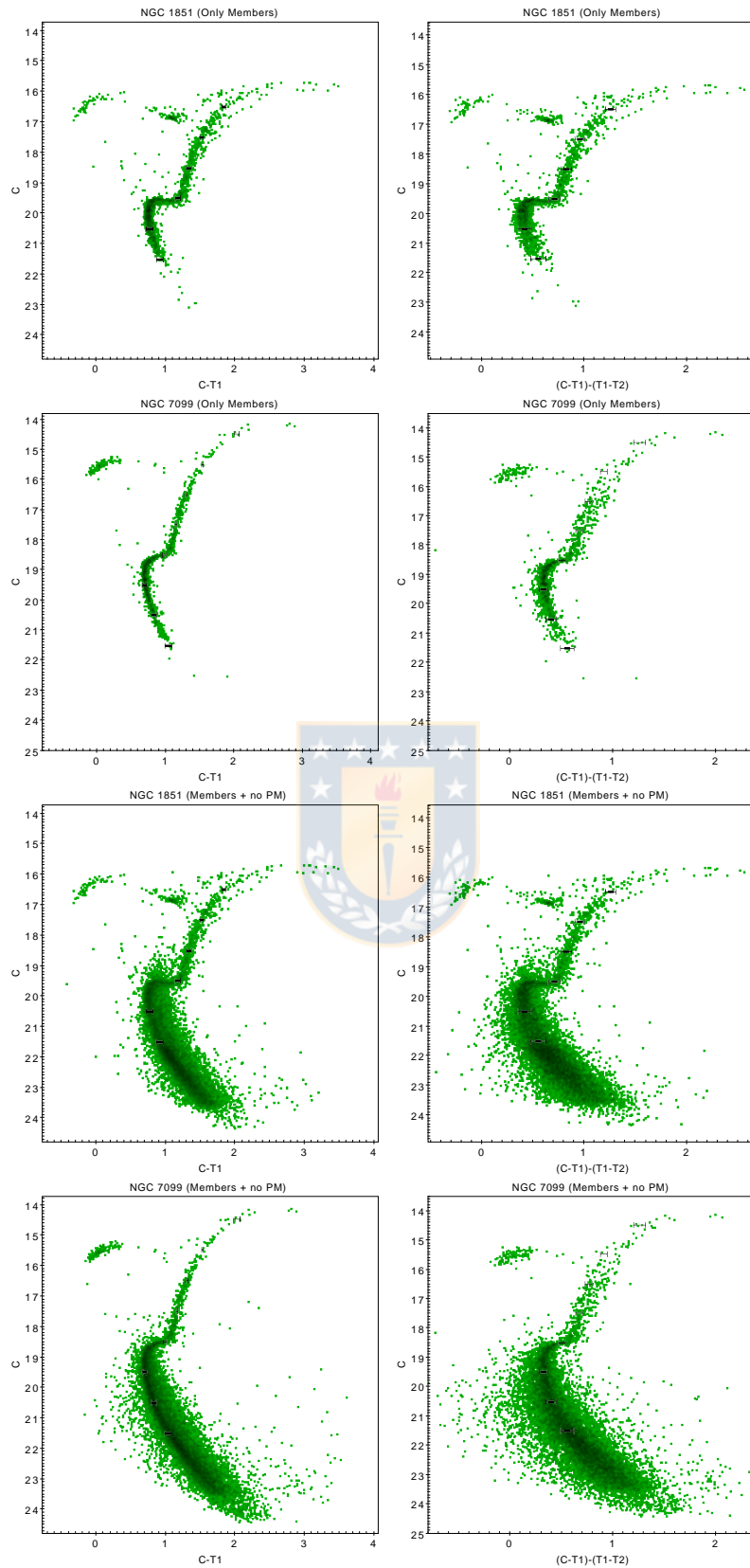
Figure 43: Left: The $(C - T1)$ CMDs from Figure 41. Right: The new color $(C - T1) - (T1 - T2)$ vs C. Mean color and magnitude errorbars in 1 magnitude bins along the principal sequence are displayed as black crosses. Source: Own elaboration.

5.3.1 NGC 7099

For NGC 7099, in both CMDs (pm members and members + stars with no pm), we can see a very broad RGB compared to $C - T_1$, similar to the CMD shown in Piotto et al.(2015) for the same cluster. Based on the C, T_1, T_2 CMDs of NGC 7099 from figure 43 we included the mean color error in 1 magnitude bins along the principal sequence, but attached to the left border of the RGB. We consider these stars inside the errorbars as those associated with the 1G, while those at the right of the limits of the errorbars are considered as 2G stars, so taking this as a guide we established our 1G/2G division in the catalog containing members + stars with no PM by drawing two lines, each connecting with the limits of the error bars, at both sides, as seen in Figure 44. The samples of each Generation of stars is taken between the 15-18 magnitude range in C and 13-17 in T2 since the MPs begin to merge in the brighter bins, and the AGB complicates the separation as well.

Figure 44: Criteria to divide the 1G from the 2G. The black lines represent the limits established for being the 1G. Source: Own elaboration.

In this part we made a correction in F17. There, we took a group of stars at the left of the RGB deemed as the 1G. Comparing the radial distributions of both 1G and 2G stars of NGC 7099 we got the most imp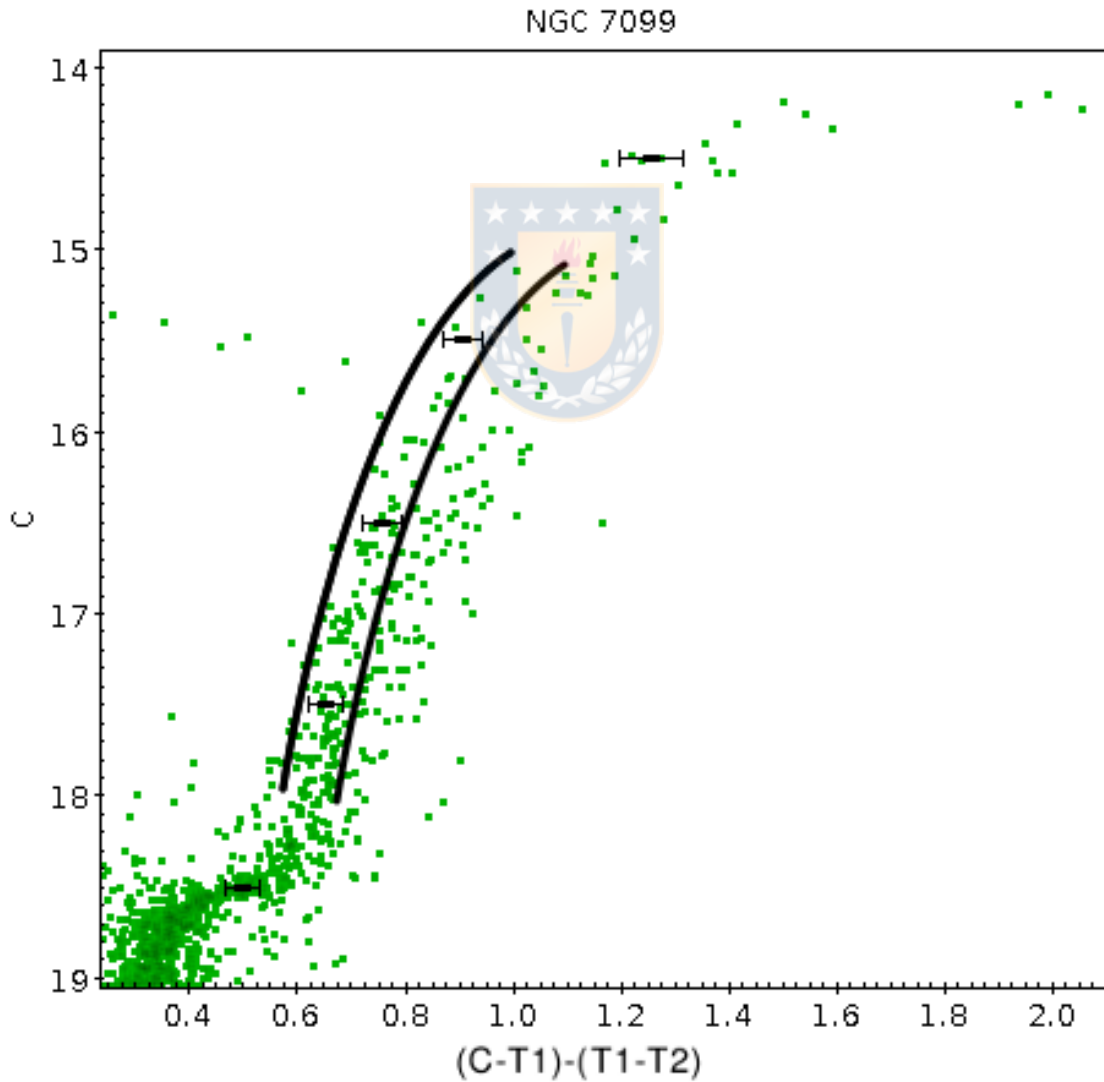ressive but unexpected conclusion of the publication: The first generation of NGC 7099 was more centrally concentrated than the second, opposite to most of the actual observations as well as MP formation models. However, our new research proves that conclusion to be wrong, since the 1G subset of F17 does not appear in our new CMD, meaning that probably it was composed of field stars that could not be removed then given the absence of Gaia PMs at the time. This would also explain why we got a p-value of 0 in our Kolmogorov-Smirnov test[8], indicating that the 1G and 2G subsets were different distributions.

We now take a new subset in $C - T_1$, trying to replicate the one from C, T_1, T_2 assumed to be our 2G and leaving the rest of the RGB as the 1G. These subsets were compared in the other colors and their radial distributions were tested to analyze which pair of subsets was more effective in distinguishing the MPs. What we should expect in this part is to have the 1G at the blue side and the 2G at the red side in both $C - T_1$ and C, T_1, T_2 colors with, hopefully, better defined subsets in the latter, but with totally the opposite ocurring in T1-T2, since in this color the filter that covers the CN-band appear as the subtrahend (and this explains why subtracting this color from $C - T_1$ should help to increase the spread on the RGB).

The results are shown in Figure 45. As expected, the subsets made based on the color C, T_1, T_2 (upper panels) are a bit less defined in the CMD with $C - T_1$, since the separation in the latter color should be less than that in the former. In $T_1 - T_2$ both populations seem to be well separated but mirrored.

The subsets made from $C - T_1$ (middle pannels) show a less effective separation in C, T_1, T_2 and a very similar one in $T_1 - T_2$. Both groups of CMDs look very similar. With $C - T_1$ the percentage of 2G stars is 23.2% of the RGB while for C, T_1, T_2 the percentage of 2G is 44.9%. This big difference in percentages could be due to the smaller spread in $C - T_1$, causing that any small error in selecting a subset includes/excludes lots of stars.

Comparing the radial distributions of both pairs of 1G/2G stars (lower pannels) we can see that both of them show a 2G more centrally concentrated, in agreement with most of the MP formation scenarios. In fact, both pair of subsets give a P-value = 0 in a K-S test. While the subset from $C - T_1$ grows faster with radius than C, T_1, T_2, the latter color includes all stars after reaching $\sim$780px from the center($\sim$200px less than $C - T_1$). The lowest right panel compares both 2G groups of stars. A K-S test between these give a P-value of 0.026, indicating that we should reject the null hypothesis of no difference between both distributions, so there are significant differences while selecting a subset from $C - T_1$ or C, T_1, T_2. And in fact, since C-T1 shows the strongest central concentration in the inner parts, its behaviour is preferred in this regard.

---

[8]If P<0.05, one must reject the null hypothesis of no difference between two datasets, more information about this test is found in http://www.physics.csbsju.edu/stats/KS-test.html
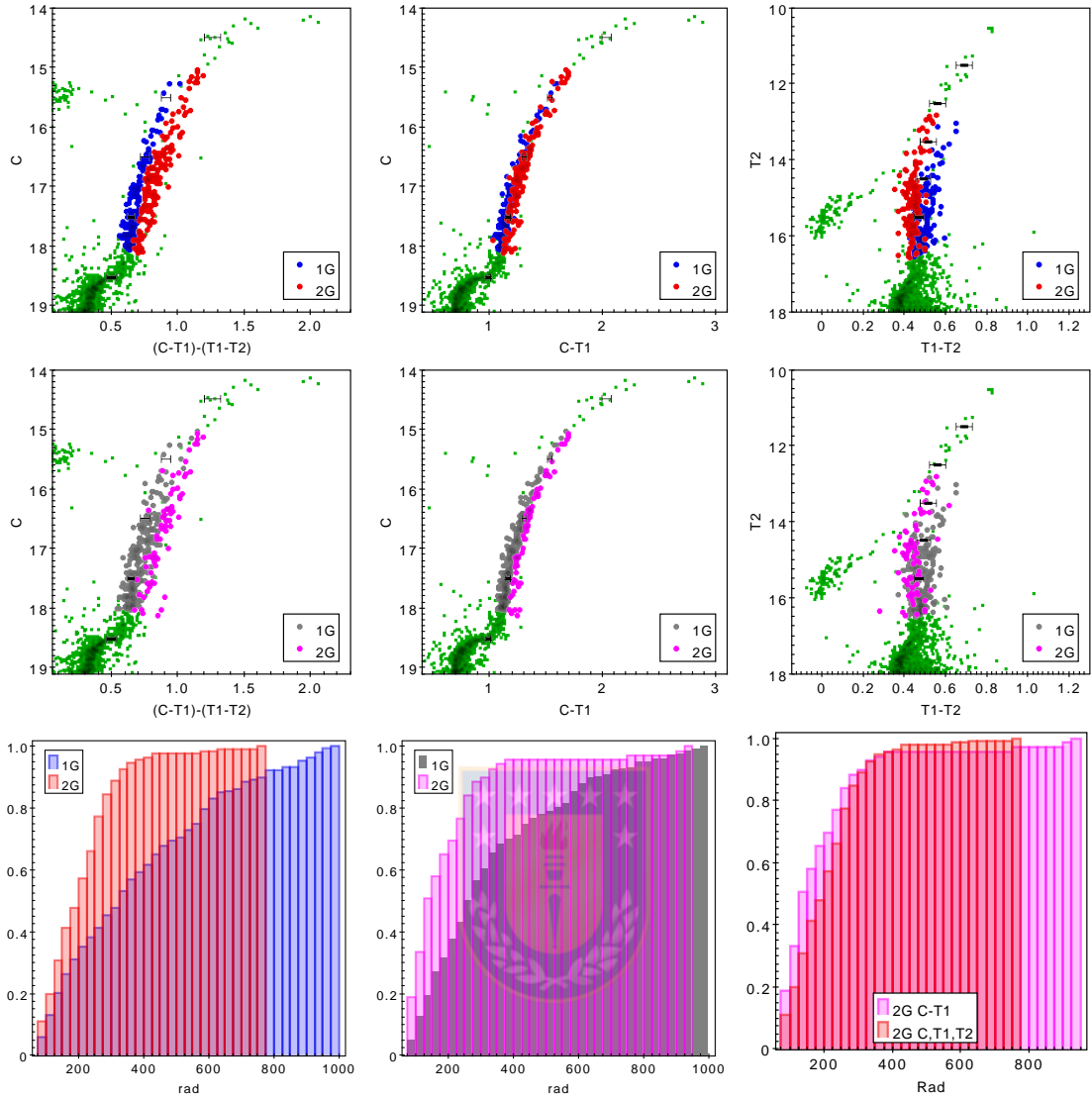
Figure 45: NGC 7099: Upper panels: A 1G/2G subset chosen from the color C,T1,T2 shown in C-T1 and T1-T2. Mid panels: A 1G/2G subset chosen from the color C-T1 shown in C,T1,T2 and T1-T2. Bottom panels: Left: Radial distributions of 1G and 2G of the subset from C,T1,T2. Middle: Radial distributions of 1G and 2G of the subset from C-T1. Right: Comparison of the 2G from the C,T1,T2 and the 2G from C-T1. Source: Own elaboration.

Table 7 shows the standard deviation (read as the width) of the RGB and the mean error in bins of 1 magnitude (with the exception of the last bins), for each of the 3 colors, while the last column shows the ratio width/error, which is a robust measurement of the effectiveness of the colors for separating MPs. As expected, $T_1 - T_2$ shows a mean ratio of 1.68, in agreement with previous studies that indicates that, although this color shows a spread slightly bigger than the errors, it is not very sensitive to the presence of MPs. The small observed difference could in fact come from an undetected source of error. For $C - T_1$, the mean ratio is 2.33, significantly larger, and enough to assure the detection of MPs. Unfortunately, C, T_1, T_2 only has a mean ratio of 2.01, significantly less than that of $C - T1$. However, we note that this is not unexpected since it is not a combination of new filters but only a combination of the width and error of the first 2 colors.

Magnitude Range	Mean width	Mean error	Ratio
	C-T_1 vs C		
15-16	0.043	0.021	2.05
16-17	0.038	0.016	2.38
17-17.9	0.041	0.016	2.56
	T_1-T_2 vs T_2		
13-14	0.061	0.039	1.56
14-15	0.052	0.033	1.58
15-16.4	0.042	0.022	1.91
	C,T_1,T_2 vs C		
15-16	0.073	0.043	1.70
16-17	0.070	0.035	2.00
17-17.9	0.063	0.027	2.33

Table 7: Comparison of error vs width in NGC 7099.

This means our C, T_1, T_2 color combination, although a reliable method to detect MPs, is not as effective as $C - T_1$. It is also less efficient, as the latter requires only observations in 2 filters.

5.3.2 NGC 1851

-The Blue and Red RGBs

As shown in Figure 46, NGC 1851 presents a double RGB: The left RGB, hereafter the Blue-RGB; and the right RGB, hereafter the Red-RGB. Both sequences are already well divided in $C - T_1$, so there are no clear differences in the subsets made from $C - T_1$ or C, T_1, T_2. Indeed, the amount of Red-RGB stars is 11.4% and 9.3% in $C - T_1$ and C, T_1, T_2, respectively. A K-S test done to the Red-RGB of both subsets give a P-value of 0.995, meaning that there is no significant difference between them. Anyway, a K-S test in both Blue-RGB and Red-RGB populations of C, T_1, T_2 give a P-value of 0.423 while for $C - T_1$ is 0.313; again neither comparison shows a significant difference.
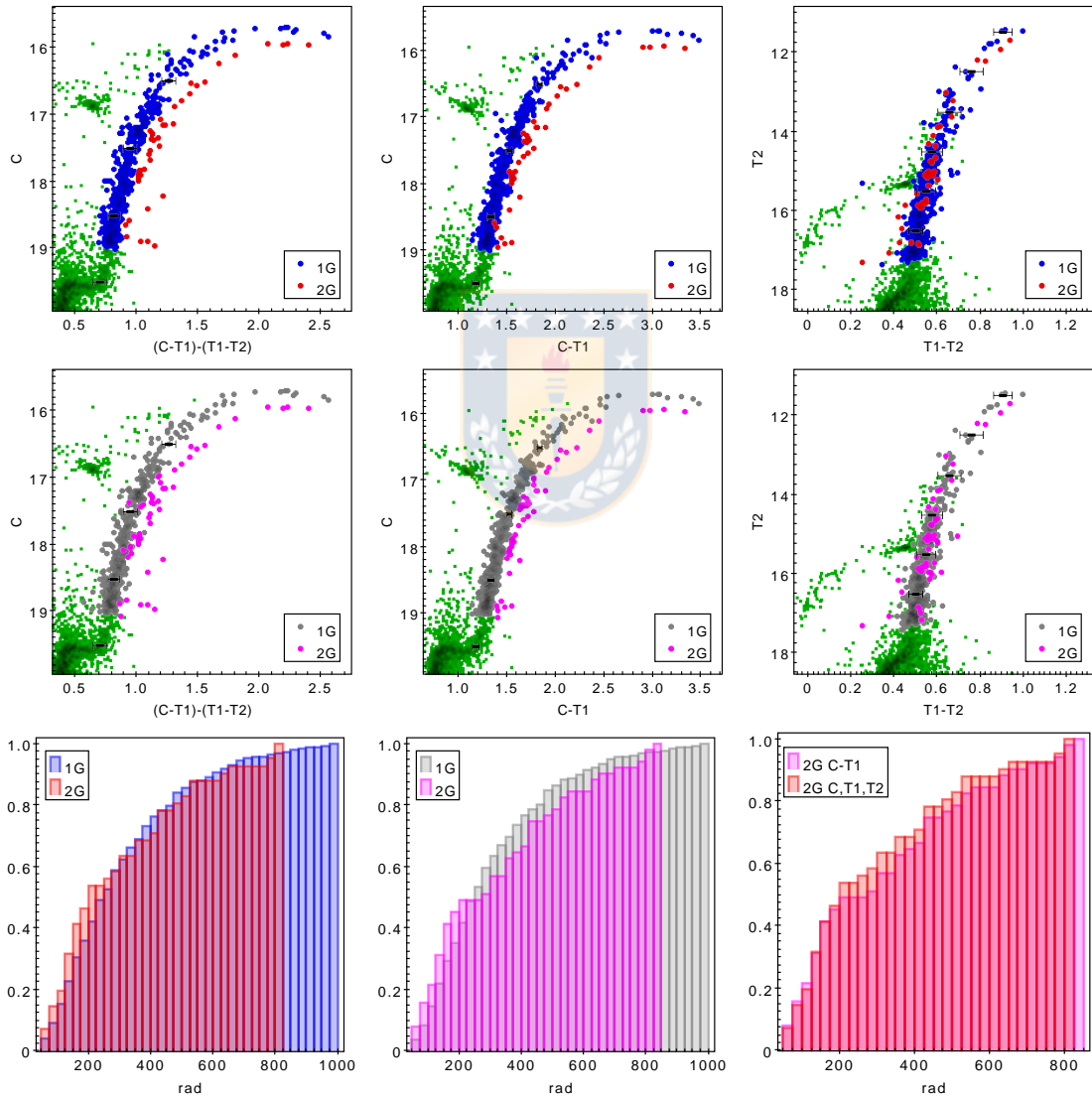
Figure 46: NGC 1851: Upper panels: A 1G/2G subset chosen from the color C,T1,T2 shown in C-T1 and T1-T2. Mid panels: A 1G/2G subset chosen from the color C-T1 shown in C,T1,T2 and T1-T2. Bottom panels: Left: Radial distributions of 1G and 2G of the subset from C,T1,T2. Middle: Radial distributions of 1G and 2G of the subset from C-T1. Right: Comparison of the 2G from the C,T1,T2 and the 2G from C-T1. Source: Own elaboration.

Both subsets also show very similar radial distributions, but as explained in C14, this behaviour could be due to the small amount of Red-RGB stars in both subsets. Also, opposed to what we expected, the Red-RGB does not appear at the right of the Blue-RGB in $T_1 - T_2$ but dispersed along the entire Blue-RGB.

The ratio width/error in NGC 1851 (table 8) shows that, although $C - T1$ give ratios even better than in NGC7099, the ratios in $T_1 - T_2$ are very low, indicating a spread completely due to the errors. Naturally, the ratios of C, T_1, T_2 should be between the values of $C - T_1$ and $T_1 - T_2$, as they are. And again, opposite to our original hope, C, T_1, T_2 does not show an improvement in the ratio with respect to $C - T_1$ and in fact is substantially worse, indicating that $T1 - T2$ is not collaborating to help split the sequences.

Magnitude Range	Mean width	Mean error	Ratio
	C-T_1 vs C		
15.7-17	0.078	0.031	2.52
17-18	0.069	0.025	2.76
18-19.2	0.054	0.025	2.16
	T_1-T_2 vs T_2		
11.4-13	0.068	0.051	1.33
13-14	0.038	0.051	0.75
14-15	0.032	0.046	0.70
15-16	0.030	0.045	0.67
16-17	0.025	0.032	0.78
17-17.5	0.022	0.032	0.69
	C, T_1, T_2 vs C		
15.7-17	0.074	0.056	1.32
17-18	0.068	0.049	1.39
18-19.2	0.060	0.041	1.46

Table 8: Comparison of error vs width in NGC 1851.

Figure 47 shows a comparison of the lower RGB and SGBs of NGC 1851 between C, T_1, T_2 vs C (left) and $C - T_1$ vs C (right). Subsets were taken from both colors trying to cover all the SGB. The fainter SGB is somewhat more visible in the former.

Radial distributions between the Bright-SGB and Faint-SGB were compared in both subsets. The K-S test in $C - T_1$ give a p-value of 0.729 while in C, T_1, T_2 give 0.590. Both subsets show no significant differences in radial distributions between Bright-SGB and Faint-SGB stars. This is in agreement with Milone et al.(2009) who also did not find differences in the radial distributions of the SGBs of NGC 1851.

The combined samples of the SGB and RGB from each Bright-SGB/Blue-RGB and Faint-SGB/Red-RGB were analyzed to discard the possibility that the lack of differences in the radial distributions is due to the low amount of stars. $C - T_1$ give a p-value of 0.095 while C, T_1, T_2 give 0.128. Both of these values are considered values too high to assure that there are differences in radial distributions. Recall that indeed C14 found differences in the radial distributions of the MS but none in the RGB and HB, even after combining them. Also, the percentage of Red-RGB/Faint-SGB stars is 14.5% in $C - T_1$ and 14,1% in C, T_1, T_2, confirming that there is no significant improvement with C, T_1, T_2 with respect to $C - T_1$ for this case.
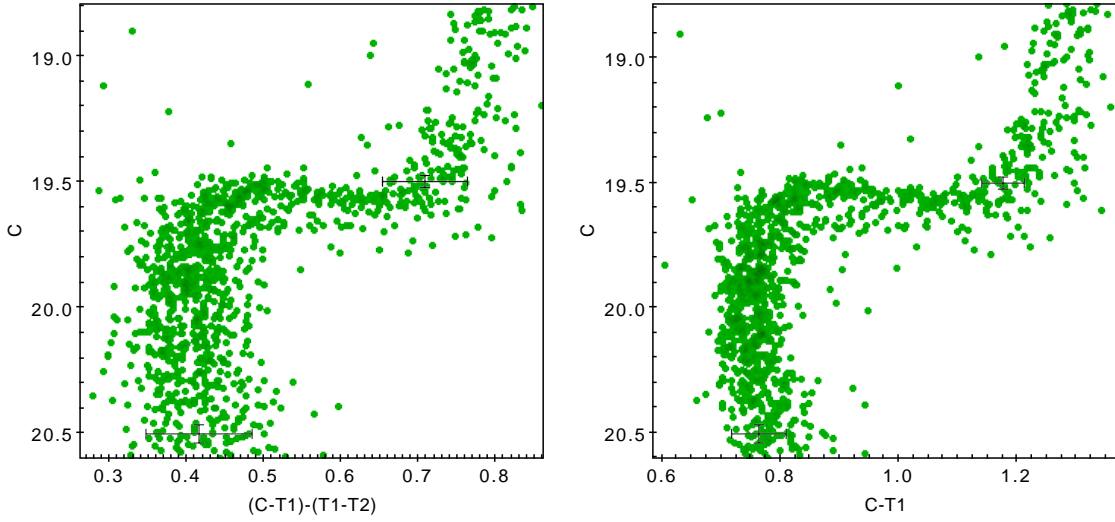
Figure 47: Comparison of the lower RGB and SGBs of NGC1851 seen in C, T_1, T_2 vs C (left) and $C - T_1$ vs C (right). Source: Own elaboration.

-First and second Generations in the Blue-RGB

According to Campbell et al.(2012), both Blue-RGB and Red-RGB could possess a first and second generations of stars. This idea is also supported by Milone et al. (2017), who found two 2G sequences in the chromosome map of NGC 1851, with a hint of a second 1G as well.

For our case, the number of stars in the Red-RGB is too small to analyze it in search of a 1G/2G division, so we will only analyze the Blue-RGB.

Following the same procedure used in NGC 7099, we used the errorbars from each color to separate the 1G from the 2G. We found a small fraction of stars lying at the left side of the Blue-RGB in $C - T_1$ and C, T_1, T_2, deemed as 1G stars. Figure 48 shows the comparison of the 1G subset chosen from C, T_1, T_2 (upper panels) and $C - T_1$ (central panels). This time the chosen subset from C, T_1, T_2 follow the expected behaviour for a different population: well defined at one side of the RGB in C, T_1, T_2, partially less defined at the same side of the RGB in $C - T_1$, and even less defined and at the opposite side of the RGB in $T_1 - T_2$, although the last point is not as clear in $C - T_1$. With C, T_1, T_2 the Blue-RGB has 10.3% of 1G stars while with $C - T_1$ the amount of 1G stars is 40.3%.

The radial distributions in $C - T_1$ gives a P-value of 0.014 while C, T_1, T_2 show a P-value of 0.870, although the last result is not as reliable since the 1G are only 21 stars.

A width to error ratio analysis indicates that $C - T_1$ has a mean ratio of 1.79 while C,T_1,T_2 vs C has a mean ratio of 0.97. $C - T_1$ ratio is too small to confirm or reject the presence of MPs while the width of C,T_1,T_2 is completely due to errors ($T_1 - T_2$ was not considered in this table since the Red-RGB is inside the Blue-RGB, hence the values of the last are the same of those in table 8).
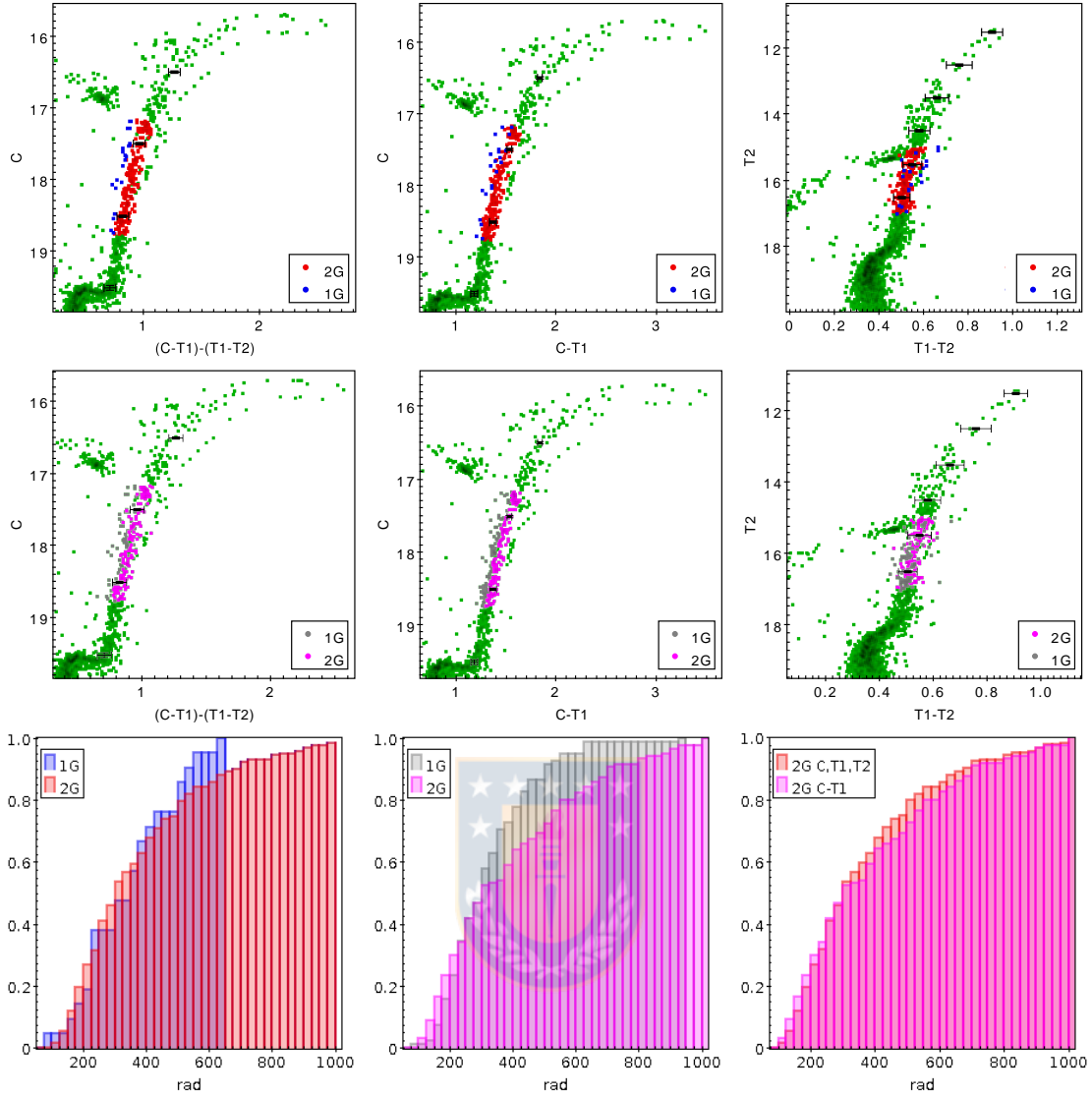
Figure 48: NGC 1851 Blue-RGB: Upper panels: A 1G/2G subset chosen from the color C,T1,T2 shown in C-T1 and T1-T2. Mid panels: A 1G/2G subset chosen from the color C-T1 shown in C,T1,T2 and T1-T2. Bottom panels: Left: Radial distributions of 1G and 2G of the subset from C,T1,T2. Middle: Radial distributions of 1G and 2G of the subset from C-T1. Right: Comparison of the 2G from the C,T1,T2 and the 2G from C-T1. Source: Own elaboration.

Magnitude Range	Mean width	Mean error	Ratio
C-T_1 vs C			
17.2-18	0.042	0.023	1.83
18-18.8	0.042	0.024	1.75
C,T_1,T_2 vs C			
17.2-18	0.044	0.047	0.93
18-18.8	0.039	0.039	1.00

Table 9: Comparison error vs width in the Blue-RGB of NGC 1851.

A further analysis was realized using data from the release of the Treasury Program GO 13297 described in Piotto et al. (2015), in an attempt to verify if our subset chosen as 1G in the Blue-RGB of NGC 1851 was correct or not. Taking as 1G the subset chosen in Milone et al. (2017) using the "Magic Trio" in NGC1851 we recreated our Washington Trio using the Filters F336W, F606W and F814W in replacement of C, T_1 and T_2 respectively. We obtained a very similar CMD, as shown in Figure 49a, where the blue stars are the 1G, the green RGB are the 2G stars and the red stars are the Red-RGB stars. The reason for the small amount of 1G stars is because most of them lie less than 22 arcseconds from the center, and we cut those stars (up to 21.75 arcseconds of radius) due to the crowding, as seen in Figure 49b. This would explain the small width to error ratios. Despite this, we were able to detect a small amount of 1G stars thanks to the C, T_1, T_2 color, confirming it as a complementary method to detect MPs.
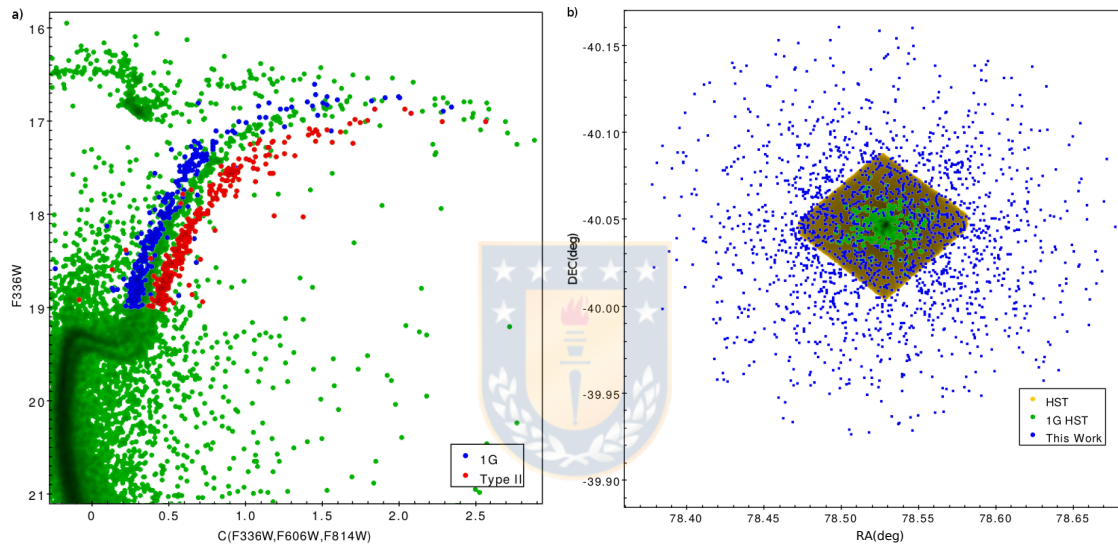

Figure 49: NGC 1851: a)CMD using F336W, F606W and F814W from HST in replacement of C, T_1 and T_2. The blue and red dots are the 1G and Red-RGB stars respectively, identified by Milone et al. (2017). b)Spatial distributions of the stars of our work and HST. Most of the 1G stars (green dots) were removed in our work due to the crowding. Source: Own elaboration.

6 Conclusions

Part I:

In this section we have derived atmospheric parameters and chemical abundances for Fe and Na for 13 RGB stars of the GC Rup106 using FLAMES-GIRAFFE data. The abundance results have been compared with Villanova et al. (2013).A photometric analysis with images taken from the 1-meter Swope Telescope was done as a complement to the spectroscopic results. For this purpose we studied the broadening of the RGB of Rup106 in the CMD using a filter sensitive to the presence of MPs. Finally, we studied the orbit of the cluster and tried to determine any possible association with a known Halo stream.

From these studies we can conclude the following:

1) Rup106 has [Fe/H] = -1.47 ± 0.01 and $[Na/Fe]_{LTE}$ = -0.47 ± 0.01. The [Fe/H] is in good agreement with V13, and the constant Na abundances confirm that the cluster does not have multiple stellar populations.

2) The $RGB_{Broadening}/RGB_{error}$ ratio in the Color-Magnitude Diagram of Rup106 is 1.5. This indicates that although there is a difference between both values, it is not large enough to contradict the spectroscopic result, and is hampered by small number statistics.

3) The orbital analysis indicates that Rup106 is confined to the halo, while the orbital energy puts Rup106 among the High-Energy group (H-E), Helmi-Stream (H99), and Sagittarius dwarf galaxy (Sgr), with the latter most likely.

It is interesting to note that combining our results concerning the orbits with the analysis from V13 we could propose the Sagittarius dwarf galaxy as the progenitor of Rup106. It also falls nicely along the age metallicity relation for this galaxy. However, the work made in Law & Majewski (2010) indicates the opposite, leaving the question open.

Part II:

In this work we have improved the Washington photometry of the clusters NGC 7099 and NGC 1851 done in Frelijj et al.(2017,F17) and Cummings et al.(2014,C14), respectively. We have determined the optimum way to reduce the data, thus obtaining the highest number of stars with the minimum possible errors. We also added PM information from Gaia to help select members. Finally, we created a new color combination $(C - T_1) - (T_1 - T_2)$ and we tested it in two clusters.

We conclude that:

1) An expected behaviour for a 1G/2G subset is to be at one side of the RGB in C, T_1, T_2; at the same side but less defined in $C - T_1$; and even less defined, at the opposite side, in $T_1 - T_2$.

2)The subsets chosen as 1G and 2G in F17 for NGC 7099 are incorrect, since the stars belonging to the 1G are actually field stars, removed now thanks to the PM provided by the Gaia mission. This explains why we got a p-value of 0.0 and the 1G stars having radial distributions more concentrated to the center than the 2G.

3)The new color combination widens the RGB of NGC 7099 better than $(C-T_1)$, allowing to properly select the Population subsets. However, $(C - T_1)$ still has the best width/error ratio. Depending on the criteria used, C, T_1, T_2 would have a stronger central concentration than $(C-T_1)$ or weaker. While the 2G subset chosen from $C - T_1$ has the highest fraction of stars within ∼300px from the center, the

subset extends until ∼980px, while the 2G subset from C, T_1, T_2 has no stars beyond ∼780px from the center.

4)We find a very small number of 1G stars at the left side of the Blue-RGB of NGC 1851 using both C, T_1, T_2 and $C - T_1$. Despite the subset of C, T_1, T_2 being slightly more accurate, the small number of stars complicates any study. A comparison with analogous HST filters (F336W,F606W and F814W) shows a very similar CMD with a higher amount of 1G stars at the same side of our small subset, confirming our findings. But a spatial analysis of those stars shows that most of them were removed in our catalog due to the crowding of stars at the center.

5) The Red-RGB in NGC 1851 does not follow the expected behaviour for a common 2G group of stars. Instead, it appears at the same side, without any improvement, in both C, T_1, T_2 and $C - T_1$ colors, while in $T_1 - T_2$ they are completely merged with the stars from the Blue-RGB. Also, little or no difference is seen in the radial distributions between the stars of the Blue-RGB and Red-RGB using the old and new color combinations, even when combining the samples with the bright-SGB and faint-SGB, respectively.

6)- The 2G percentage in the RGB of NGC 7099 is 23.2% for $C - T_1$ and 44.9% for C, T_1, T_2.

- The percentage of Faint-SGB/Red-RGB stars respect to the total number of stars in the SGBs and RGBs in NGC 1851 is 14.5% for $C - T_1$ and 14.1% for C, T_1, T_2.

- The percentage of 1G stars in the Blue-RGB of NGC 1851 is 40.3% for $C - T_1$ and 10.3% for C, T_1, T_2.

Comparing these percentages with those of Milone et al.(2017)(∼62% of 2G stars in NGC 7099, ∼3% of Red-RGB stars in NGC 1851 and ∼26.4% of 1G stars in NGC 1851) we find little relation. This difference might occur because we removed the center of our cluster (a radius of 21,75" in NGC 1851 and 34.8" in NGC 7099) in order to avoid issues due to the crowding. In addition, the HST photometry used here covers the field up to a radius of only ∼2.47' while our photometry covers up to a radius of ∼7.25'.

7 Bibliography

- Alonso, A., Arribas, S., & Martínez-Roger, C. 1999, A&AS, 140, 261

- Bajkova A. T., Bobylev V. V., 2020, arXiv, arXiv:2008.13624

- Bastian, N., Lamers, H. J. G. L. M., de Mink, S. E., et al. 2013, MNRAS, 436, 2398

- Bastian, N. 2015, arXiv:1510.01330

- Bastian N., Lardo C., 2018, ARA&A, 56, 83.

- Baumgardt, H., Hilker, M., Sollima, A., et al. 2019, MNRAS, 482, 5138.

- Bedin, L. R., Piotto, G., Anderson, J., et al. 2004, Memorie della Societa Astronomica Italiana Supplementi, 5, 105

- Bellazzini M., Ferraro F. R., Ibata R., 2003, AJ, 125, 188.

- Bonatto, C., Campos, F., & Kepler, S. O. 2013, MNRAS, 435, 263

- Brown, J. A., Wallerstein, G., & Zucker, D. 1997, AJ, 114, 180

- Campbell S. W., Yong D., Wylie-de Boer E. C., Stancliffe R. J., Lattanzio J. C., Angelou G. C., D'Orazi V., et al., 2012, ApJL, 761, L2. doi:10.1088/2041-8205/761/1/L2

- Cannon R. D., Stobie R. S., 1973, MNRAS, 162, 207. doi:10.1093/mnras/162.3.207

- Canterna, R. 1976, AJ, 81, 228

- Carretta, E., Bragaglia, A., Gratton, R. G., et al. 2009, A&A, 505, 117

- Carretta, E., Bragaglia, A., Gratton, R. G., et al. 2010, A$A, 516, A55

- Carretta E., Gratton R. G., Lucatello S., Bragaglia A., Catanzaro G., Leone F., Momany Y., et al., 2010, ApJL, 722, L1. doi:10.1088/2041-8205/722/1/L1

- Carretta E., Lucatello S., Gratton R. G., Bragaglia A., D'Orazi V., 2011, A&A, 533, A69. doi:10.1051/0004-6361/201117269

- Cassisi S., Salaris M., Pietrinferni A., Piotto G., Milone A. P., Bedin L. R., Anderson J., 2008, ApJL, 672, L115. doi:10.1086/527035

- Chandar, Rupali & Fall, S. & Whitmore, Bradley & Mulia, Alexander. (2018). The Fraction of Stars That Form in Clusters in Different Galaxies.

- Chaisson Eric, McMillan Steve. (2004). Astronomy today.

- Cohen, J. G. 1978, ApJ, 223, 487

- Cottrell, P. L., & Da Costa, G. S. 1981, ApJL, 245, L79

- Cummings, J. D., Geisler, D., Villanova, S., & Carraro, G. 2014, AJ, 148, 27.

- D'Ercole, A., Vesperini, E., D'Antona, F., McMillan, S. L. W., & Recchi, S. 2008, MNRAS, 391, 825

- D'Ercole, A., D'Antona, F., & Vesperini, E. 2016, MNRAS, 461, 4088. doi:10.1093/mnras/stw15

- D'Ercole, A., D'Antona, F., Ventura, P., Vesperini, E., & McMillan, S. L. W. 2010, MNRAS, 407, 854

- Decressin T., Meynet G., Charbonnel C., Prantzos N., Ekström S., 2007, A&A, 464, 1029. doi:10.1051/0004-6361:20066013

- Decressin T., Charbonnel C., Meynet G., 2007, A&A, 475, 859. doi:10.1051/0004-6361:20078425

- Dotter, A., Sarajedini, A., & Anderson, J. 2011, ApJ, 738, 74

- Dotter, A., Milone, A. P., Conroy, C., et al. 2018, ApJl, 865, L10

- Elmegreen, B. G. 2017, ApJ, 836, 80. doi:10.3847/1538-4357/836/1/80

- Fernández-Trincado J. G., Chaves-Velasquez L., Pérez-Villegas A., Vieira K., Moreno E., Ortigoza-Urdaneta M., Vega-Neme L., 2020, MNRAS, 495, 4113.

- Fernie, J. D. 1983, PASP, 95, 782

- Forbes, D. A., & Bridges, T. 2010, MNRAS, 404, 1203

- Frelijj, H., Geisler, D., Cummings, J., et al. 2017, MNRAS, 472, 4532

- Gaia Collaboration, Prusti, T., de Bruijne, J. H. J., et al. 2016, A&A, 595, A1

- Gaia Collaboration, Brown, A. G. A., Vallenari, A., et al. 2018, A&A, 616, A1

- Gaia Collaboration, Brown A. G. A., Vallenari A., Prusti T., de Bruijne J. H. J., Babusiaux C., Biermann M., 2020, arXiv, arXiv:2012.01533

- Geisler D., Claria J. J., Minniti D., 1991, AJ, 102, 1836. doi:10.1086/116008

- Geisler, D. 1996, AJ, 111, 480

- Gieles, M., Charbonnel, C., Krause, M. G. H., et al. 2018, MNRAS, 478, 2461. doi:10.1093/mnras/sty1059

- Hamuy M., Folatelli G., Morrell N. I., Phillips M. M., Suntzeff N. B., Persson S. E., Roth M., et al., 2006, PASP, 118, 2. doi:10.1086/500228

- Han S.-I., Lee Y.-W., Joo S.-J., Sohn S. T., Yoon S.-J., Kim H.-S., Lee J.-W., 2009, ApJL, 707, L190. doi:10.1088/0004-637X/707/2/L190

- Harris, W. E. 1996, AJ, 112, 1487

- Hénault-Brunet, V., Gieles, M., Agertz, O., & Read, J. I. 2015, MNRAS, 450, 1164

- Ideta, M., & Makino, J. 2004, ApJL, 616, L107

- Kaufmann, William J. (1991). Universe.,3rd Edition, W.H. Freeman

- Kurucz, R. L. 1970, SAO Special Report, 309

- Lardo C., Milone A. P., Marino A. F., Mucciarelli A., Pancino E., Zoccali M., Rejkuba M., et al., 2012, A&A, 541, A141. doi:10.1051/0004-6361/201118763

- Law D. R., Majewski S. R., 2010, ApJ, 718, 1128.

- Lee, J.-W. 2010, MNRAS, 405, L36

- Marcolini, A., Gibson, B. K., Karakas, A. I., et al. 2009, MNRAS, 395, 719. doi:10.1111/j.1365-2966.2009.14591.

- Martell, S. L. & Smith, G. H. 2009, PASP, 121, 577. doi:10.1086/599979item Massari D., Koppelman H. H., Helmi A., 2019, A&A, 630, L4.

- Milone A. P., Bedin L. R., Piotto G., Anderson J., King I. R., Sarajedini A., Dotter A., et al., 2008, ApJ, 673, 241. doi:10.1086/524188

- Milone A. P., Stetson P. B., Piotto G., Bedin L. R., Anderson J., Cassisi S., Salaris M., 2009, A&A, 503, 755. doi:10.1051/0004-6361/200912256

- Milone, A. P., Piotto, G., Bedin, L. R., et al. 2012, ApJ, 744, 58

- Milone, A. P., Marino, A. F., Piotto, G., et al. 2013, ApJ, 767, 120

- Milone A. P., Piotto G., Renzini A., Marino A. F., Bedin L. R., Vesperini E., D'Antona F., et al., 2017, MNRAS, 464, 3636. doi:10.1093/mnras/stw2531

- Monaco L., Villanova S., Carraro G., Mucciarelli A., Moni Bidin C., 2018, A&A, 616, A181.

- Moreno E., Pichardo B., Schuster W. J., 2015, MNRAS, 451, 705.

- Mucciarelli A., Bonifacio P., 2020, A&A, 640, A87.

- Norris, J., Freeman, K. C., & Da Costa, G. S. 1984, ApJ, 277, 615

- Osborn, W. 1971, The Observatory, 91, 223

- Piotto, G., Milone, A. P., Bedin, L. R., et al. 2015, AJ, 149, 91

- Prantzos N., Charbonnel C., 2006, A&A, 458, 135. doi:10.1051/0004-6361:20065374

- Ramírez, I. & Meléndez, J. 2005, ApJ, 626, 465.

- Renzini, A., D'Antona, F., Cassisi, S., et al. 2015, MNRAS, 454, 4197

- Robin A. C., Reylé C., Derrière S., Picaud S., 2003, A&A, 409, 523.

- Robin A. C., Reylé C., Fliri J., Czekaj M., Robert C. P., Martins A. M. M., 2014, A&A, 569, A13.

- Romanishin, W.(2000) An introduction to astronomical Photometry using CCDs

- Salinas, R., & Strader, J. 2015, ApJ, 809, 169

- Sanders J. L., Smith L., Evans N. W., 2019, MNRAS, 488, 4552.

- Sbordone L., Bonifacio P., Marconi G., Buonanno R., Zaggia S., 2005, A&A, 437, 905.

- Sbordone, L., Salaris, M., Weiss, A., & Cassisi, S. 2011, A&A, 534, A9

- Sirianni, M., Jee, M. J., Benítez, N., et al. 2005, PASP, 117, 1049.

- Smith, G. H., & Norris, J. 1984, AJ, 89, 263

- Sneden, C. 1973, ApJ, 184, 839. doi:10.1086/152374

- Sneden, C., Kraft, R. P., Prosser, C. F., & Langer, G. E. 1992, AJ, 104, 2121

- Stetson, P. B. 1987, PASP, 99, 191

- Stetson, P. B. 1994, PASP, 106, 250

- Tautvaišienė, G., Wallerstein, G., Geisler, D., et al. 2004, AJ, 127, 373

- Taylor, M. B. 2005, Astronomical Data Analysis Software and Systems XIV, 347, 29

- Valcarce, A. A. R., & Catelan, M. 2011, AAP, 533, A120

- Vande Putte, D., & Cropper, M. 2009, MNRAS, 392, 113

- Villanova, S., Geisler, D., Carraro, G., Moni Bidin, C., & Muñoz, C. 2013, ApJ, 778, 186

- Walker, A. R., Kunder, A. M., Andreuzzi, G., et al. 2011, MNRAS, 415, 643

- Yong D., Grundahl F., D'Antona F., Karakas A. I., Lattanzio J. C., Norris J. E., 2009, ApJL, 695, L62. doi:10.1088/0004-637X/695/1/L62

- Yong D., Grundahl F., Norris J. E., 2015, MNRAS, 446, 3319. doi:10.1093/mnras/stu2334

  http://wise2.ipac.caltech.edu/docs/release/prelim/expsup/sec4_3c.html